Photoluminescence study of Cu(In,Ga)Se_2 and $Cu_2ZnSnSe_4$ used for thin film solar cells

A Thesis submitted for the Degree of
Master of Philosophy

by
Ekaterina Skidchenko

The Department of Physics

University of Strathclyde

2017

This thesis is the result of the author’s original research. It has been composed by the author and has not been previously submitted for examination which has led to the award of a degree.

Signed:

Date:

Abstract

In this study we were trying to answer the question why the best laboratory-size $CuIn_{1-x}Ga_xSe_2$-based (CIGSe) solar cells have been achieved at about 30% Ga, whereas the optimal band gap requires much higher Ga content (around 50%). Also for the first time ever we examined the effects of 4 keV Ar^+ irradiation on optical properties of $Cu_2ZnSnSe_4$ (CZTSe) thin films. Photoluminescence (PL) measurements were performed on samples of CIGSe single crystals with x=0, 0.05, 0.10, 0.25, 0.50, 0.75, 1 and on samples of CZTSe thin films before and after Ar^+ irradiation. The impact of variations in excitation intensity and temperature on the nature of the PL bands was investigated. For most CIGSe samples band-tail (BT) recombination coupled with band-band (BB) transition were identified as being responsible for the obtained PL peaks. The calculated band tails are deeper in $CuGaSe_2$ than in $CuInSe_2$, explaining why an increase in Ga content $x > 0.3$ does not improve the efficiency of solar cell. Also band-impurity (BI) transition and donor-acceptor pair (DAP) recombination were discovered. For the first time ever excitons in the CIGSe samples with 5% and 10% Ga content were clearly observed and identified. In the CZTSe samples BI recombination was established as the main source of PL. Ar^+ irradiation of CZTSe produced significant changes in the material: reduced PL intensity and creation of tail defect complexes supported by an increase in the average band tail depth γ from 25 to 30 meV as well as increase in the activation energy from 75 to 88 meV. The composition of the CIGSe and CZTSe samples was investigated using energy dispersive x-ray (EDX) analysis and wavelength dispersive x-ray (WDX) technique, respectively. According to the microscopy results, calculated cation ratios proved the nature of established recombinations.

Contents

Chapter 1

Introduction

1.1 Solar energy

Nowadays it is hard to imagine human life without electricity. Virtually all the devices we use in everyday life, from coffee machines to supercomputers, operate using electricity. However, traditional sources of electric power (such as fossil fuel, nuclear reaction) cause numerous environmental problems, for example climate changes due to emission of CO_2 and environmental disasters caused by accidents at atomic power stations.

All of this has made people turn to alternative, or renewable, energy sources such as hydro, wave, wind, solar power and etc. that are environmentally friendly. Although all of the renewable power sources have their own advantages and disadvantages, solar energy is the most abundant. Firstly, during the hours of daylight the energy from the sun can be used anywhere and at any time. Secondly, solar devices based on simple operation principles can directly harvest the sunlight and convert it to usable energy [1]. Moreover, solar installations do not have moving parts, resulting in low maintenance costs. Finally, they do not produce either noise or pollution (redundant solar cells can contain toxic materials like Cd, Te, Se) during their operation nor damage natural areas in the way wind and hydro installations do.

The capabilities of solar power can hardly be overestimated. For example, at the end of 2015 it was estimated that 22 countries had sufficient solar PV capacity to meet more than 1% of their electricity demand, with far higher figures in some countries (e.g., 7.8% in Italy, 6.5% and 6.4% in Greece and Germany, respectively) [2]. Now it is even possible to build a house in Canadian climate that will only rely on solar energy without any electricity supply from other sources [3]. Such a house costs only 25% greater than a similar one without solar panels.

1.2 Basics of photovoltaics

Photovoltaic solar cells are based on the p-n junction, as shown in Figure 1.1.

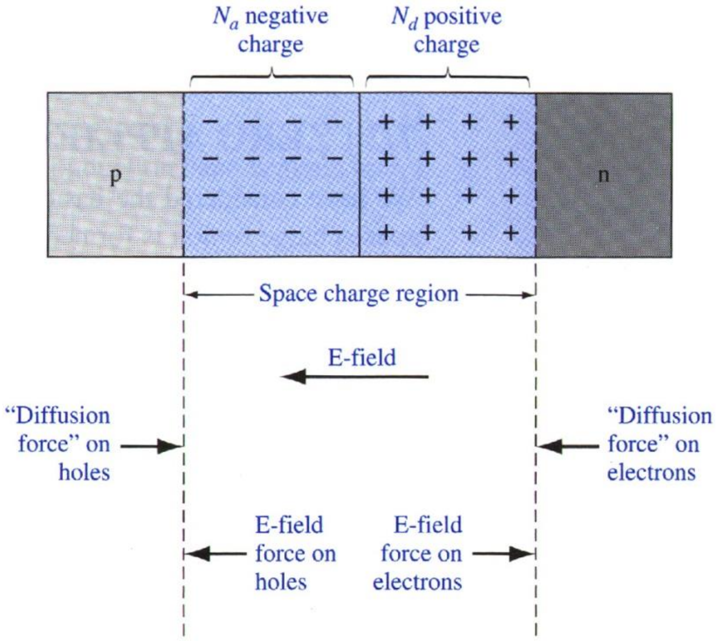

Figure 1.1: Semiconductor p-n junction showing the depletion region [4].

When a junction is formed between the p- and n-regions of a semiconductor, electrons diffuse from the n side of the junction to the p side to neutralise the charge imbalance. Similarly, holes diffuse from the p side of the junction to the n side. As electrons diffuse from the n side, positively charged acceptor atoms are left behind. Similarly, as holes diffuse from the p side, they uncover negatively charged donor atoms. The net positive and negative charges in the n and p regions induce an electric field in the region near the junction. This diffusion process continues until the electric field formed by the separation of the electrons and holes becomes great enough to prevent any further diffusion. A region devoid of free charge carriers (the depletion or space charge region) is formed near the junction, as shown in Figure 1.1.

When light with photon energy that is greater than the bandgap energy is incident on the junction region, it can be absorbed creating electron-hole pairs. These free electrons and holes will be swept out of the depletion region by the built-in electric field. If electrodes are attached to the p and n regions and an external load is connected, the electrons from the n region and also holes from other side can flow around the external circuit, generating a current in the load. This is the principle on which solar cells operate.

The efficiency of a solar cell is defined as the ratio of the light power input to the electrical power output. For example, if 500 W/m^2 of solar radiation is falling on a 1 m^2 solar cell then the light power input is 500 W. If this 1 m^2 solar cell can feed 50 W of the generated electricity into an external resistive load, its efficiency is $\frac{50}{500} = 10\%$.

It has been shown, using a thermodynamic treatment of the p-n junction [5], that the maximum achievable efficiency is about 29% and 26% for an outer-space and terrestrial single-junction solar cell, respectively. There the efficiency of a single-junction solar cell is plotted as a function of the semiconductor band gap for various levels of illumination. AM0 ("Air mass zero") illumination is the intensity of solar radiation at the top of the Earth's atmosphere. AM1.5 ("Air mass 1.5") illumination corresponds to the intensity received at the Earth's surface, after the sunlight has been filtered by the atmosphere and some parts absorbed by certain gases.

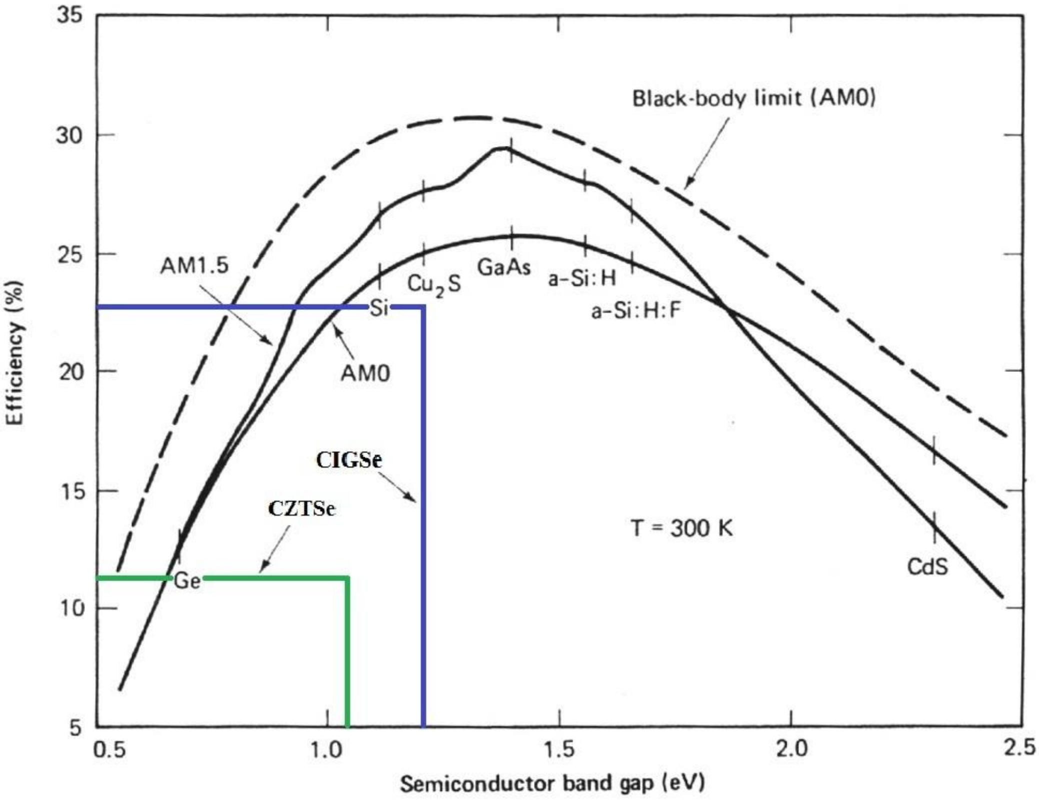

Figure 1.2: Dependence of the theoretical limit of the conversion efficiency of single junction solar cells on the bandgap of their absorber for AM1.5, AM0 and the thermodynamic limit as well as current record efficiencies for CZTSe (11.6% [6], marked in green), CIGSe (22.6% [7], marked in blue) based laboratory scale solar cells [8].

1.3 Materials' significance

The first solar cells were made using monocrystalline silicon (m-Si) for both the n-type and p-type layers. Many different materials have been tried since, the most important being polycrystalline silicon (p-Si), gallium arsenide (GaAs), cadmium telluride (CdTe) and copper indium diselenide ($CuInSe_2$). The choice of these materials can be explained in view of their band gap values that are within 1.0-1.75 eV range, meaning high conversion efficiencies to be achieved as shown in Fig. 1.2.

In general, materials for the solar cell absorber layer firstly should have a high absorption coefficient in order to reduce the required thickness of the absorber layer and therefore the cost of the very solar cell and should be non-toxic and sustainable. They should also have good radiation resistance, to extend the solar cell's lifetime.

Compared with pure $CuInSe_2$, $Cu(In,Ga)Se_2$ associated alloys have the advantage of a variable band gap, making it a desirable material for solar cell absorber. Also CIGSe is considerably less toxic than its leading thin film competitor CdTe. The radiation resistance of CIGS-based solar cells is at least 50 times greater than that of Si- or GaAs-based ones. Another advantage of CIGS is that it is a direct bandgap material, so no energy is lost to phonons when an absorbed photon creates an electron-hole pair. This makes direct bandgap semiconductors more efficient than those with an indirect bandgap such as Si. The absorption coefficient α of CIGSe exceeds 10^5 cm^{-1} at energies greater than 1.5 eV (at wavelengths greater than 827 nm) and in fact it is one of the highest among known semiconductors.

The $Cu_2ZnSnSe_4$ is another attractive material for absorption layer. As well as CIGSe it is a direct band gap material with absorption coefficient close to that one of CIGSe. Moreover, by using the $Cu_2ZnSnSe_4$ in solar cells the ambiguous problem of In scarcity would be solved, since CZTSe contains inexpensive and earth-crust-abundant elements [9].

The unique properties of this compound make it a promising material for space applications. However, the radiation hardness of CZTSe is poorly studied. There is only one paper describing properties of CZTSSe after ionizing radiation treatment, but for single crystals, not thin films [10]. That is why the study of 4 keV Ar^+ irradiation is extremely important as it will provide valuable information on radiation resistance of thin film $Cu_2ZnSnSe_{4.}$ Ar ions are convenient ions to study radiation effects (in particular, radiation defects), because Ar is an inert material, does not form chemical bonds and, therefore, does not complicate the analysis.

The highest reported conversion efficiencies ~ 22.6% [7] and ~11.6% [6] for CIGSe (marked in blue) and CZTSe (marked in green), respectively (Figure 1.2). These numbers are impressive, but there is still plenty of room for further improvement. For comparison, efficiency evolution of different types of solar cells is shown on Figure 1.3.

This project investigates the effects of substituting In by Ga in the semiconductor alloy $CuIn_{1-x}Ga_xSe_2$ on the defects observed in the semiconductor. Additionally, $Cu_2ZnSnSe_4$ thin films are studied before and after Ar^+ cleaning to examine any changes in spectra. Defects are the major factor limiting solar cell efficiency and a deeper understanding of the defects that exist will help to find the ways to increase the efficiency of CIGS and CZTSe thin-film solar cells.

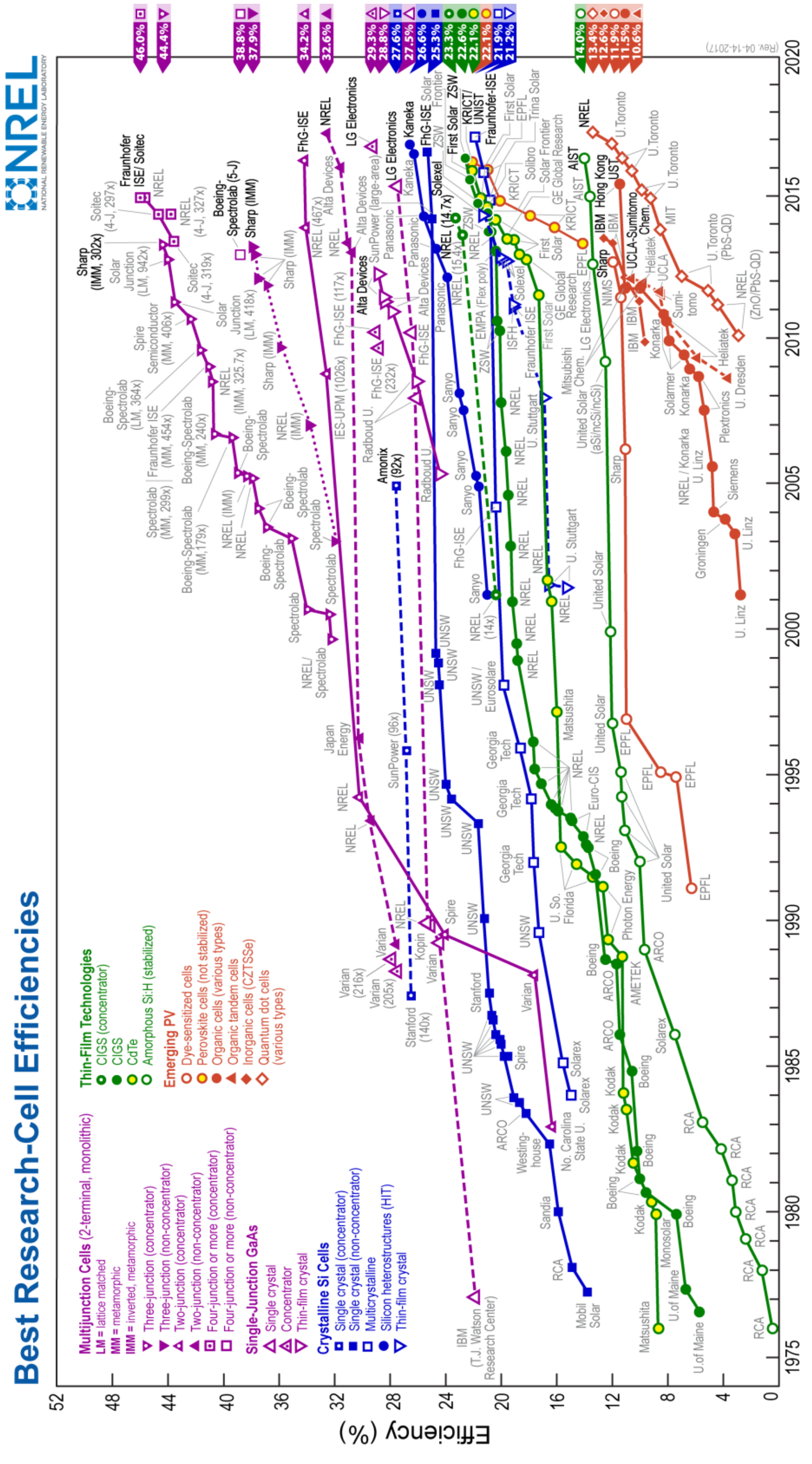

Figure 1.3: Research cell record efficiency chart [11].

Chapter 2

Materials

2.1 Growth

The $CuIn_{1-x}Ga_xSe_2$ single crystals were grown by the vertical Bridgman technique [12] by Dr Michael Yakushev. Samples with different Ga content (x=0, 0.05, 0.10, 0.25, 0.50, 0.75 and 1) were synthesised. The process of growth comprised the following stages.

Initially, stoichiometric proportions of copper, indium, gallium and selenium were placed in a quartz ampoule, which was then sealed under vacuum. After that this ampoule was placed in a rocking furnace to melt the elements at temperatures of 1100 °C and mix them thoroughly together. Then the ampoule with CIGSe was cooled down to the room temperature. This results in a polycrystalline CIGSe.

To convert the polycrystalline material into a single crystal, the ampoule was placed in a vertical furnace. This furnace has two sections: the upper hotter section was kept at a temperature above the melting point (990 °C for $CuInSe_2$ and 1030 °C for $CuGaSe_2$), whereas the bottom section was kept below the melting point, but above a solid state sphalerite to chalcopyrite phase transition at 810 °C. The ampoule was slowly (1 mm per hour) moved through the gradient between the two temperature regions. Then the temperature in the bottom furnace was slowly (one degree an hour) reduced to 650 °C. From 650 °C to 20 °C the temperature was reduced at a faster rate of 10 degrees per hour. During the process the polycrystalline material recrystallises as a single crystal.

Prior to the PL measurements ingots of the $CuIn_{1-x}Ga_xSe_2$ single crystals were cut into 2 mm slices perpendicular to the growth direction. Samples for PL analysis were cleaved to expose clean surfaces. Cleaved samples for experiments were then embedded into In to maximise heat transport from the sample and placed on a sample holder in the cryostat.

The CZTSe thin films were synthesised by selenisation of magnetron deposited precursors [13] at Northumbria University (Newcastle). The process comprised the following stages at certain conditions.

Firstly, precursor layers were simultaneously deposited on Mo-coated soda-lime glass substrates by magnetron sputtering of high-purity Cu, Zn and Sn. This stage was performed at room temperature. Then the precursors were selenised in graphite boxes by a two-step rapid thermal process for 5 and 15 minutes, respectively. The first step was at 300°C and the second at 500°C. Nitrogen at 850 mbar was used as a background pressure.

The CZTSe samples were studied for PL twice: before and after the films were irradiated by 4 keV Ar ions with a dose of $2x10^{16}$ cm^{-2}, corresponding to 3 minute surface cleaning with Ar^+ beam for X-ray photoelectron spectroscopy (XPS) measurements.

Before fixing by Cu plates on the sample holder the CZTSe samples were divided into 5 mm x 5 mm pieces by mechanical scribing and wrapped in In foil again to maximise heat transport from the sample.

2.2 Physical properties

The lattice of $CuInSe_2$ has the tetragonal chalcopyrite structure. The crystal structure can be visualised as two interpenetrating face-centered cubic sublattices displaced from each other by ¼ of a body diagonal. One sublattice contains only selenium atoms, while the other sublattice contains equal numbers of copper and indium atoms. The lattice is distorted by the different sizes of copper and indium atoms. In $Cu(In,Ga)Se_2$ a fraction of In atoms in the structure described above are replaced with Ga atoms. Otherwise, the structure remains the same. A unit cell of the chalcopyrite tetragonal structure is shown in Figure 2.1a below.

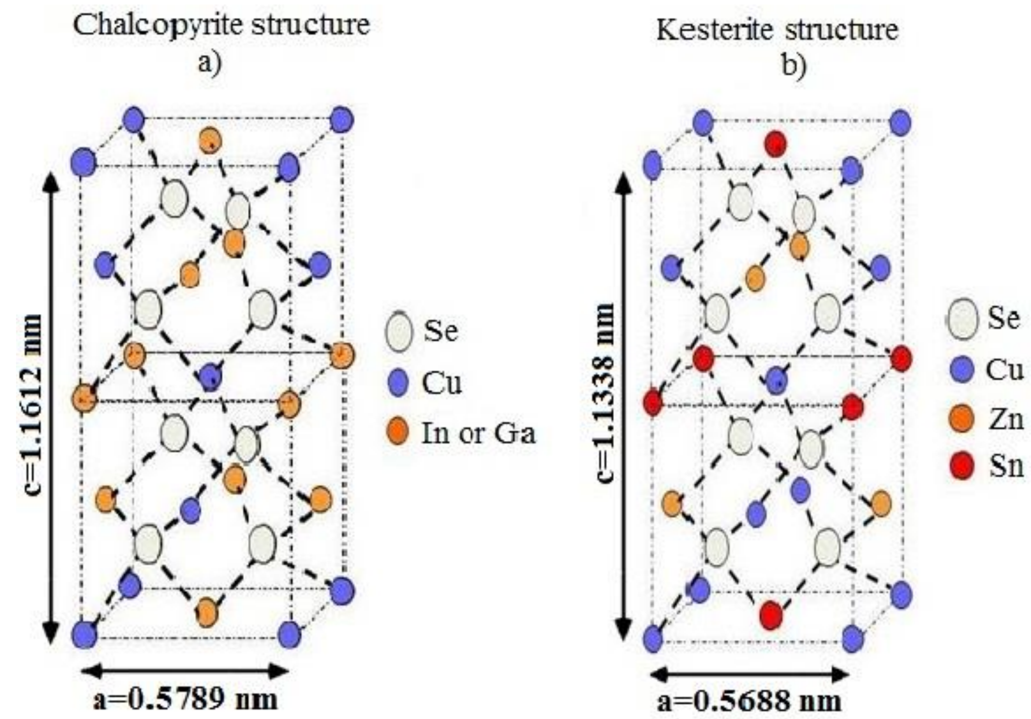

Figure 2.1: A unit cell of (a) the chalcopyrite and (b) the kesterite tetragonal structures.

CZTSe, on the other hand, crystallises with the kesterite structure, to obtain which every two In or Ga atoms (group III) in chalcopyrite structure should be replaced by a Zn atom (group II) and Sn atom (group IV) as seen in Figure 2.1b, maintaining the octet rule [9].

For $CuInSe_2$ and $Cu_2ZnSnSe_4$ the lattice parameters are a=0.5789 nm and c=1.1612 nm [14], a=0.5688 nm and c=1.1338 nm [15] for chalcopyrite and kesterite structures, respectively.

2.3 Electronic band structure

The easiest way to describe the electronic band structure of $CuInSe_2$ is to compare it with electronic band structure of zinc blende (ZnSe). There are two bands in the zinc blende structure, conduction and valence. The valence band is a triply degenerate p-like state. In $CuInSe_2$ because of different lengths of the chemical bonds for Cu–Se and In–Se a tetragonal distortion is created, as was mentioned in section 2.2. This distortion causes a splitting of the valence band at the Γ point in ZnSe into the three sub-bands A, B, and C in chalcopyrite as shown in Figure 2.2 and 2.3 below.

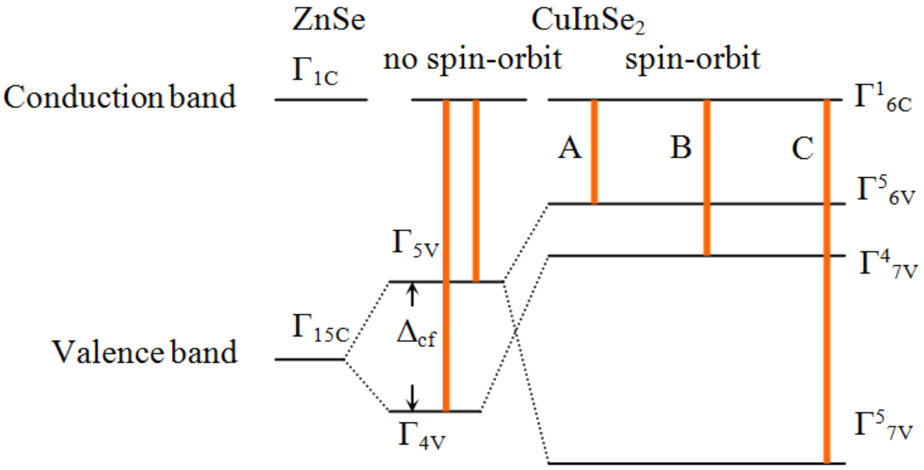

Figure 2.2: The band structure of zinc blende and $CuInSe_2$. Symmetry groups are indicated. Δ_{cf} – the crystal field splitting.

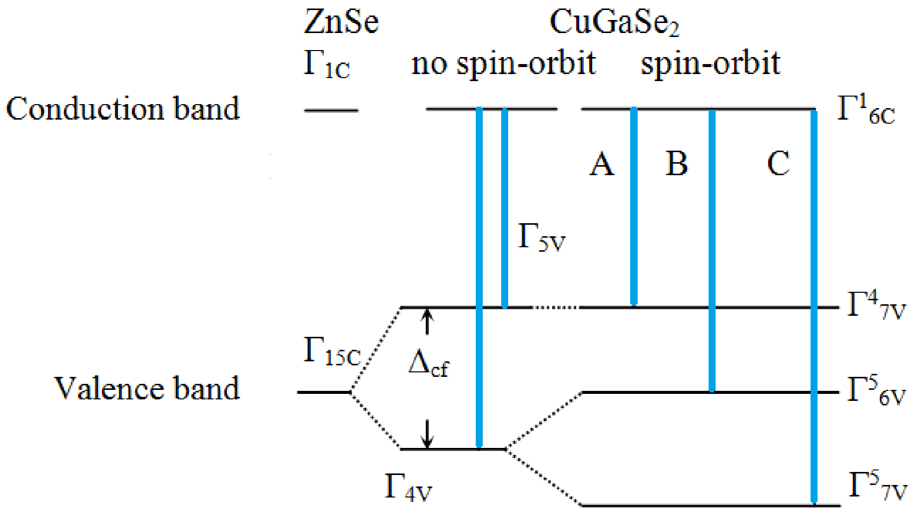

Figure 2.3: The band structure of zinc blende and $CuGaSe_2$. Symmetry groups are indicated. Δ_{cf} – the crystal field splitting.

In terms of the quasi-cubic model the splitting can be explained as a simultaneous influence of the non-cubic crystal-field and spin-orbit interactions that determine the spectral splitting of the A-B and B-C bands, respectively.

The electronic band structure of CZTSe with AB and C sub-bands is shown in Figure 2.4.

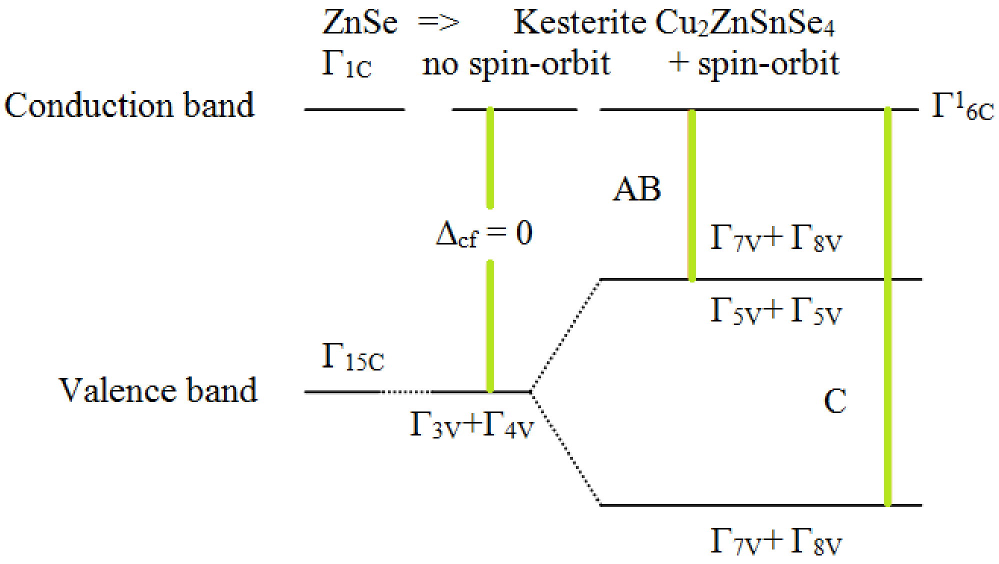

Figure 2.4: The band structure of zinc blende and $Cu_2ZnSnSe_4$. Symmetry groups are indicated. Δ_{cf} – the crystal field splitting [16, 17].

The tetragonal distortion $\tau = 1\text{-}c/2a$, where c and a are the lattice constants, is small and negative (-0.29 %) for CuInSe2 and small and positive (+0.33 %) for CZTSe. This results in a small and positive value of the crystal field splitting (Δ_{cf}), which inverts the valence sub-band sequence in $CuInSe_2$ and gives the uppermost A sub-band the Γ_{6v} symmetry.

2.4 Samples used

To effectively detect the PL emission from samples the values of E_g of each sample should be known and, according to that, appropriate detector should be selected. The band gap values of pure $CuInSe_2$ and $CuGaSe_2$ were calculated from the following equation:

$$E_g = E_{max} + E_b, \qquad (2.1)$$

where E_{max} is the spectral peak position of the free A exciton and E_b is the binding energy of that exciton, the values of which were taken from [18] and [19] for $CuInSe_2$ and $CuGaSe_2$, respectively. The E_g, of the rest of CIGSe samples was obtained by the interpolation, assuming the linear dependency. Figure 2.5 below shows how E_g in CIGSe samples is changing with increasing Ga content. The band gap energy of CZTSe samples was taken from [20].

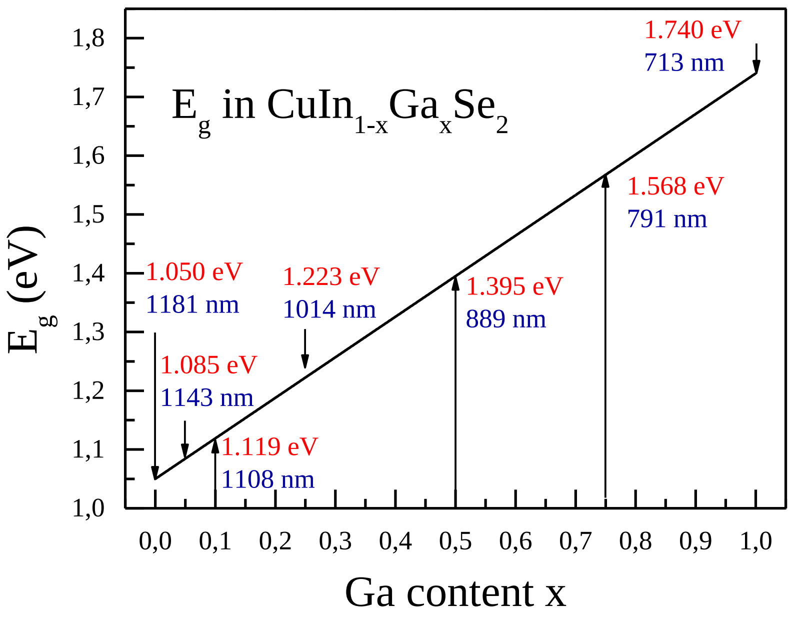

Figure 2.5: The dependence of band gap energy on the sample composition in $Cu(In,Ga)Se_2$.

All samples used in this study are listed below (Table 2.1 and Table 2.2), showing their E_g as well as detector used and its operating wavelength ranges. More information on the detectors will be given in the section 4.1.

Table 2.1 $Cu(In,Ga)Se_2$ samples used in this study.

	Sample	E_g	Detector
1.	$CuInSe_2$	1.050 eV (1181 nm)	PMT InGaAs (950-1650 nm)
2.	$CuIn_{0.95}Ga_{0.05}Se_2$	1.085 eV (1143 nm)	
3.	$CuIn_{0.9}Ga_{0.1}Se_2$	1.119 eV (1108 nm)	
4.	$CuIn_{0.75}Ga_{0.25}Se_2$	1.223 eV (1014 nm)	
5.	$CuIn_{0.5}Ga_{0.5}Se_2$	1.395 eV (889 nm)	Ge diode (300-1700 nm)
6.	$CuIn_{0.25}Ga_{0.75}Se_2$	1.568 eV (791 nm)	PMT R636 (200-900 nm)
7.	$CuGaSe_2$	1.740 eV (713 nm)	

Table 2.2 $Cu_2ZnSnSe_4$ samples used in this study.

	Sample	E_g	Detector
8.	$Cu_2ZnSnSe_4$	1.030 eV (1204 nm)	PMT InGaAs (950-1650 nm)
9.	$Cu_2ZnSnSe_4$ (Ar^+ cleaning)		

Chapter 3

Theory of photoluminescence

3.1 Concept of PL

If photons with a sufficiently high (in excess of E_g) energy falls on a semiconductor, it will be absorbed and it will excite electrons within the material. The process of the electrons relaxation by returning to their ground state results in an emission of light that is called photoluminescence (PL). When the energy loss does not produce light the recombination is non-radiative and involves, for example, the emission of phonons instead of light (Figure 3.1a).

In an ideal semiconductor with no defects, the two most important energy bands are the conduction and valence bands, separated by an energy gap with no energy levels. However, intrinsic defects or impurities can create energy levels in the band gap. Electrons can now make transitions to and from these energy levels within the gap. By analysing the spectrum of PL the information about the semiconductor electronic band structure and its defects can be obtained. Possible types of recombinations are illustrated in Figure 3.1.

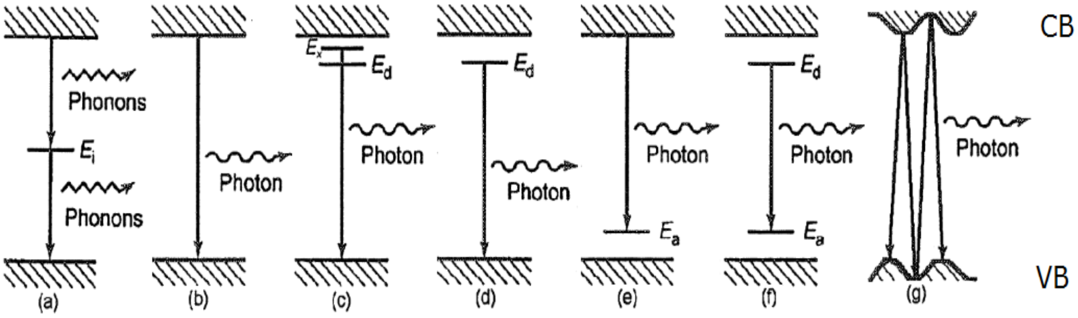

Figure 3.1: (a) Non-radiative recombination via an intermediate state. (b-g) Radiative recombination paths: (b) band-band; (c) excitonic features; band-impurity: (d) donor-valence band; (e) conduction band-acceptor; (f) donor-acceptor; (g) band-tail [21].

Since the bandgap energy of ternary semiconductor compounds is highly sensitive to the sample composition, spatial variations in the composition on a microscale also cause potential fluctuations [22]. These can cause widening of the PL bands, since the energy of the bands in PL spectra varies across the region excited by the laser beam.

Non-radiative transitions are more likely from levels deep in the bandgap as was stated earlier, while photoluminescence is mainly observed from shallow defect levels close to the conduction or valence band. Therefore it is important to ensure that these defect levels are occupied. This requires cooling of the sample, because at high temperatures the electrons and holes in the defect levels thermalise into the conduction or valence bands leaving the defect levels empty. In order to gain information on defects PL spectra are taken at temperatures below ~100 K. Also at higher temperatures the probability of non-radiative recombination and scattering of charge carriers by phonons is high, resulting in lower PL intensity.

It is also important to take into account that the material's bandgap depends on temperature, namely, an increase in temperature decreases the width of the forbidden band in conventional binary compounds. However, in the chalcopyrites $CuInS_2$, $CuInSe_2$ and $CuGaSe_2$ (ternary compounds) the bandgap behaves abnormally. At low temperatures it increases, achieving a maximum at about 70-100 K and then E_g starts to decrease. This occurs because of the optimisation of distances between atoms in the lattice, since the third atom appears.

In comparison with other experimental techniques for characterising semiconductor materials (for example, reflection and absorption study) photoluminescence spectroscopy has several significant advantages [23]. Firstly, it is a highly sensitive non-destructive method with easy data acquisition. Secondly, sample preparation is quite simple, since this technique is much less stringent about thickness and surface flatness of the samples. Additionally, no electrodes are required and all the apparatus is relatively simple.

3.2 PL transitions

Several possible recombination mechanisms can be the origin of the peaks seen in the PL spectra. The type of transition involved depends on the type and concentration of defects, as well as level of doping. Further all recombination mechanisms will be discussed one by one in the order of increase in the impurity concentration.

Band-band (BB)

When the defect concentration in the semiconductor material is low or the temperature is high the BB recombination is the main source of PL. In this case the free excited electron makes a transition from the conduction band to the valence band to recombine there with the free hole as shown in Figure 3.1b. Since the emitted photon has an energy close to E_g, the energy of band gap and BB peak correlate with the temperature. Therefore, one of the ways to identify a BB transition is to perform a temperature dependence measurement. The energy of the PL peak related to BB recombination should follow the bandgap as the temperature varies.

Excitonic (EX)

Another indication of low concentrations of defects in semiconductor is the presence of excitonic peaks in PL spectra. When a semiconductor absorbs a photon, an electron-hole pair is created. Due to the Coulomb attraction force between electron and hole and since the electron effective mass is much less than that of the hole, electron can orbit the hole like a proton in a hydrogen atom. The “quasi-particle” consisting of an electron in the conduction band orbiting a hole in the valence band is called an exciton [21]. This bound electron-hole pair can recombine to give excitonic emission (Fig. 3.1c).

As a rule it is easy to identify excitonic emission since excitons produce very narrow (tens of nanometers) bands with peak position not changing with increasing excitation intensity [24, 25].

There are 2 forms of excitons that can be found in semiconductors: free (FE) and bound (BE) excitons. Free excitons are not tied to a particular defect and can move in semiconductor. Bound excitons cannot move since they are localised at a defect site. Bound and free excitons are assigned according to temperature dependence. The former ones quench at lower temperatures (50-70 K) and the latter ones quench at around two times higher temperatures (120-150 K).

Band-impurity (BI)

At slightly higher concentrations of impurities the band-to-impurity recombination becomes the dominant radiative transition. An excited electron can either make a transition from a donor level to the valence band (Figure 3.1d) or from the conduction band to an acceptor lever (Figure 3.1e). In this case the energy of emitted photons that can be observed in PL spectra is:

$$h\nu = E_g - E_i \tag{3.1}$$

where E_i is the energy of donor or acceptor ionisation with respect to the conduction or valence band. The energy of BI peaks slowly changes with temperature with respect to the band gap. Another way to identify this type of transition is to perform an excitation intensity experiment. At low levels of doping such bands do not shift with changing excitation power. However in non-conventional highly doped semiconductors that will be discussed later on, such bands can blueshift with increasing excitation intensity at quite high rates. This type of transition is also called free-to-bound (FB).

Donor-acceptor pair (DAP)

At higher defect concentration donor-acceptor recombination, as shown in Figure 3.1f, becomes the main source of PL. In this instance this type of transition is possible since the wavefunctions of donor electrons and acceptor holes overlap. The energy of the emitted photon is described by:

$$h\nu = E_g - \left(E_A + E_D\right) + \frac{e^2}{\varepsilon r} \tag{3.2}$$

where r is the distance between donor and acceptor atoms [26]. With increase in the excitation intensity and temperature free carriers move to more favourable levels inside the band gap. This makes the donor-acceptor distance smaller and therefore according to the equation above increases the energy of emitted photon and, respectively, the energy of DAP peak on PL spectra.

Band-tail (BT)

At very high levels of defects the random distribution of charged impurities causes spatial potential fluctuations in the conduction and valence bands edges. The fluctuations of defect potentials cause a widening of the defect levels within the forbidden gap. The energy of the conduction and valence band becomes spatially dependent, therefore there is a range of energies which can be created by band-band recombination. This is known as band tail related emission. States with energies below the unperturbed conduction band or above the unperturbed valence band are called tail states (Figure 3.1).

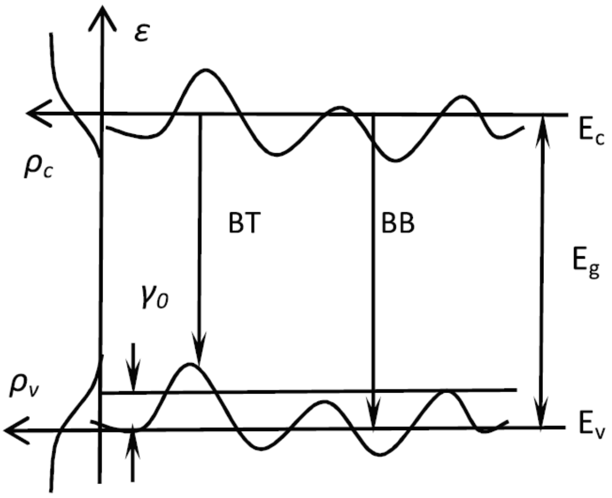

Figure 3.2: Schematic representation of the BB and BT types of transitions, where γ_0 is the average band tail depth (the average depth of potential fluctuations).

Spatial potential fluctuations are very common in highly doped and compensated semiconductors. The PL emission in such semiconductors essentially includes the BT and BB recombination. While the BB band becomes prominent at higher temperatures and high excitation intensities, the BT band can dominate at lower temperatures.

Although both the conduction and valence band can be affected by potential fluctuations in compensated semiconductors (containing high population of both donors and acceptors) the high doping limit can be easier achieved for donors. It happens because in the chalcopyrites and kesterites the effective mass of the electron m_e is significantly smaller than that of the hole m_h (in $CuInSe_2$ for example m_e= $0.09m_0$ whereas m_h= $0.7m_0$ where m_0 is the mass of free electron) therefore the size of a donor state is significantly greater than that of an acceptor one. Therefore in both chalcopyrites and kesterites the material is easily degenerates in terms of electrons whereas the high level of doping for holes is not achieved.

Speaking of BT transitions, because of the potential fluctuations at low temperatures the holes are mostly captured by the deep band states within the fundamental band gap. These deep band states form localised states for holes that seem to be the acceptor states rather than valence band states. Therefore the BT band can be considered as a recombination of a free electron from Fermi level F_n with a hole captured by the localised state. The shape of the BT band can be calculated from (3.3):

$$I_{BT}(h\nu) \propto \iint W_{BT}(E_e, E_h)\rho_c(E_e)f_e(E_e)\rho_v(E_h)q_h(E_h)\delta(E_e - E_h - h\nu)dE_e dE_h \qquad (3.3)$$

where I_{BT} is both the intensity and shape of the curve; W_{BT} is a radiative recombination probability; E_e, E_h - energy of electrons and holes, respectively; ρ_c, ρ_v - density of states functions for the electrons in the conduction band and for the localised holes, respectively; f_e - distribution function for the electrons (the Fermi function); q_h - distribution function for the localised holes.

According to [27] the BT band at low temperatures has an asymmetrical shape with an abrupt slope on the high-energy side and more gentle decrease on the low-energy side. The latter one is determined by the ρ_v function which does not depend on excitation intensity or temperature, whilst the former one has much more complex nature.

In most cases the shape of ρ_v and the low-energy side I_{LE} at low temperatures can be described by (3.4) and (3.5), respectively:

$$\rho_v(\varepsilon) = \rho_0 \exp\left(-\frac{\varepsilon}{\gamma}\right) \qquad (3.4)$$

$$I_{LE}(h\nu) \propto \exp\left[-\frac{E_g - h\nu}{\gamma}\right] \qquad (3.5)$$

where γ is the average band tail depth. The low energy side of the BT band can be fitted with (3.5) and γ can be determined. The high-energy side (I_{HE}) of the BT band has several common properties for all types of the density of states function for localised holes. At low temperatures (when $kT<\gamma$) the slope of I_{HE} gradually increases with temperature and at higher temperatures (when $kT>\gamma$) the BT band becomes more symmetrical.

With increasing excitation intensity the spectral peak position of BT band shifts towards higher energies, since the concentrations of free electrons and holes increases. On the other hand, at low temperatures the BT peak spectral position decreases linearly with temperature and more rapidly than the band gap energy does. At higher temperatures, when spectral peak position reaches some characteristic temperature it shifts to higher energies.

Another type of radiative recombination that can be observed in the PL spectra of chalcopyrites and kesterites is the BI recombination. It is observed when the materials contain a high concentration of acceptor whose energy level is deeper than the average depth of potential fluctuations. Such a transition at the presence of potential fluctuations of the valence band is affected by its tail. The energy level is transformed into a broad band, which has an asymmetric shape with long low energy tail and more abrupt high energy side very similar to the BT band. The peak position also shifts with changing excitation intensity at a high rate (see paragraphs describing j-shift in section 3.3). At temperature increase the BI band redshifts. Its low energy side is associated with the density of states and can be used to determine the average depth of potential fluctuations. More information on tail emission can be found elsewhere [22].

3.3 PL peaks identification

The aim of the PL analysis is to identify the type of radiative recombination in each particular sample. There are two main experiments in the PL study that can help to achieve this: excitation intensity dependence and temperature dependence, each with its own features. The presence of one or another recombination type is revealed by the character of the alterations in peak shape, PL intensity and position of maximum energy, as experimental conditions (excitation intensity, temperature) are changed.

To improve the accuracy of the determination of the position of PL peaks and also to extract maximum information from experimental spectra different theoretical fitting shapes can be applied. The choice of fitting function depends on the shape of the analysed band in the PL spectrum and the recombination type.

In the case of excitons peaks they were firstly separated from the background by subtracting a straight line modelling the background and then the peaks were fitted with a simple Gaussian model because this function fits well the exciton peak shape [28].

The PL peaks of the majority of the CIGSe samples and all CZTSe samples were fitted using an empirical asymmetric double sigmoid function [22]:

$$I(h\nu) = A\left(\frac{1}{1+\exp\left[-\frac{h\nu - E_1}{W_1}\right]}\right) \times \left(1 - \frac{1}{1+\exp\left[-\frac{h\nu - E_2}{W_2}\right]}\right) \qquad (3.6)$$

where A, E_1, E_2, W_1 and W_2 are experimental parameters. $E_1$and W_1 represent the shape of the low-energy side of the PL spectrum that determined by density of states, while E_2 and W_2 stand for the high-energy side determined by temperature features.

This model was chosen, because it results in the best fitting for bands in PL of highly doped chalcopyrites and kesterites, since simple Gaussian or Lorentzian models do not work well (Fig. 3.3). Additionally, from this theoretical model the average band tail depth γ-value ($\gamma = W_1$) is derived. The importance of determining γ will be described later on.

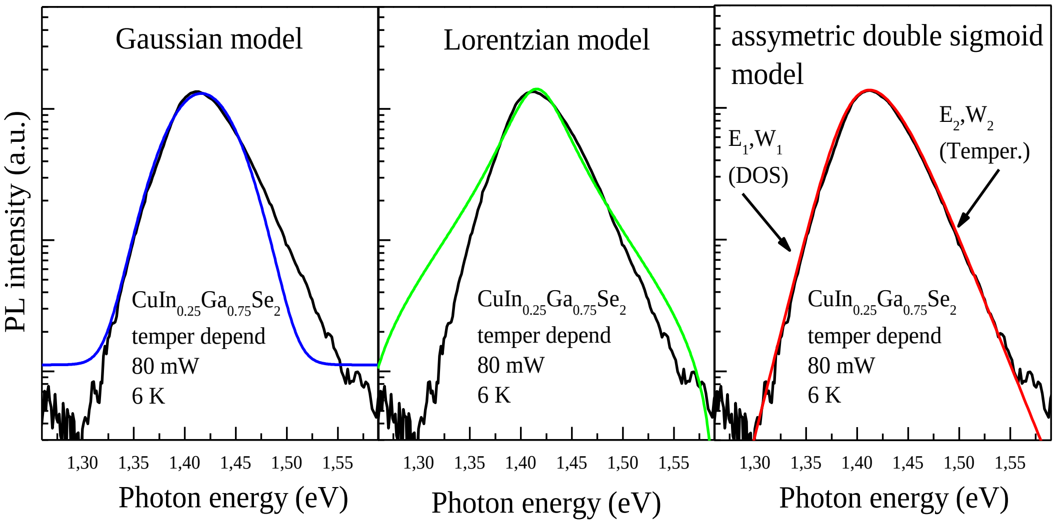

Figure 3.3 – Example of peak fitting for the PL spectrum from $CuIn_{0.25}Ga_{0.75}Se_2$. Black - experimental data, blue – Gaussian model, green – Lorentzian model, red - asymmetric double sigmoid model.

In the case of a set of peaks that are hardly resolvable the PL analysis sometimes is conducted only for the dominant peaks. However, this provides quite rough and inconclusive results.

Excitation intensity dependence

Excitation intensity dependence is collected at the lowest possible temperature T≈6 K by varying laser excitation intensity from fractions of a mW (using neutral density (ND) filters) up to 160-200 mW, depending on the maximum PL intensity of the analysed sample. There are 2 methods for the identification of the PL peak nature that can be applied for excitation intensity dependence data.

1) **j-shift**

This shift is determined from the dependence of the peak energy E_{max} on log(laser excitation intensity) I_{exc}. In such a dependency the data points are fitted by straight line whose gradient provides the value of the j-shift (the rate of the shift change per decade of the excitation power). Also from this plot we determine at which laser power $E_{max}(I_{exc})$ starts saturating due to temperature rise, that is important for temperature dependence measurements.

Moreover, the j-shift is the level of compensation and indicates how different the concentrations of donors and acceptors are [21]. The greater the j-shift, the closer these concentrations. If after some treatment the j-shift remains the same, this means that these processes do not greatly change the ratio of the donors and acceptors concentrations, generating both donors and acceptors.

The j parameter is found to have different values for different types of recombinations: as a rule, for a DA recombination $j < 3$ and for band tails $j > 3$. Excitonic recombination and conventional BI recombination band do not show a shift in peak energy with excitation intensity change (i.e. $j=0$) [26].

2) **k-coefficient**

This coefficient is determined from log(peak PL intensity) vs. log(laser excitation intensity) plot of experimental points fitted by straight line. In this dependency values of integrated PL intensity were used for the peak PL intensity. The slope of the fitted straight line equals the k coefficient. For the EX and BB transitions the k-value is much greater than 1, for the all defect related recombinations it is less than 1 [29].

Temperature dependence

Temperature dependence is measured by varying the temperature from 6 K up to 300 K, depending on the PL intensity of the particular sample. We use maximum excitation laser power I_{exc}, at which the E_{max} (I_{exc}) has not started to saturate. This value is derived from peak energy vs. log(laser excitation intensity) plot for each particular sample.

There are 2 methods of the PL peak identification that can be used for temperature dependence data analysis.

3) **Peak energy vs. temperature plot**

There are some characteristic patterns for the temperature dependence of each type of recombination. For example, if at increasing temperature the peak spectral position shifts first to lower energies, reaches a minimum, and starts to move toward higher energies then we can identify the recombination mechanism as BI or BT recombination. It is a clear indication that we have highly doped material with band tails generated by spatial potential fluctuations due to high concentrations of charged defects [21]. In the case when the peak position shifts to higher energies with increase in temperature DAP is involved [26].

4) **Log(peak PL intensity) vs. 1000/temperature plot**

This dependence is very important since provides the value of the activation energy (E_a) that is the energy of electrons at the donor impurity must obtain in order to thermalise into the conduction band or the energy of holes at the acceptor impurity to be thermalised to the valence band. Two different activation energies indicate that two recombination processes occur.

The experimental points are fitted using 3 different theoretical models: simpler Arrhenius-1(Ar-1), Arrhenius-2 (Ar-2) and more complex Krustok-1 (Kr-1) [30]. Models Ar-1 and Kr-1 provide one value of activation energy, while from Ar-2 two values is derived. These fitting formulae are presented beneath. For Ar-1:

$$\mathrm{y(x)} = \frac{\mathrm{P1}}{1 + \mathrm{P2} * \exp(-\mathrm{E_a} * 0.0116 * \mathrm{x})} \tag{3.7}$$

For Ar-2:

$$\mathrm{y(x)} = \frac{\mathrm{P1}}{(1 + \mathrm{P2} * \exp(-\mathrm{E_{a1}} * 0.0116 * \mathrm{x})) + \mathrm{P3} * \exp(-\mathrm{E_{a2}} * 0.0116 * \mathrm{x})} \tag{3.8}$$

Finally, for Kr-1:

$$y(x) = \frac{P1}{\left(1 + P2 * \left(\frac{1000}{x}\right)^{\frac{3}{2}} + P3 * \left(\frac{1000}{x}\right)^{\frac{3}{2}} * \exp(-E_a * 0.0116 * x)\right)} \qquad (3.9)$$

where P_n variables are normalization parameters.

After fitting the results are compared. The quality of the fit is evaluated by eye and by comparing the values of R^2 and error that should be close to 1 and close to 0, respectively. On the other hand, the values of the activation energy should make physical sense. As a rule, it is not less than energy of the most shallow defects of 5-10 meV and greater than 200-700 meV, when the defects become deep traps). Also two activation values should be of close values.

Summing up all information stated above it is possible to create the sequence of PL data analysis that will help to identify the type of recombination in each case.

Sequence of PL data analysis

Firstly, the shape of the PL spectrum should be investigated, since the excitonic features present very narrow peaks. These are usually clearly seen and it is difficult to confuse them with other types of recombinations.

Secondly, the k-value is considered. If k<1 then recombination is defect related, otherwise excitonic or BB types of recombination are present.

Thirdly, the nature of the shift type at temperature increase is determined. If in the temperature dependence the band red shift is observed then the recombination is associated with BT or BI transitions. If the shift is blue then the DAP transition is involved. When initially red shift is observed, but after reaching some energy minimum the blue shift is observed, the last part of the curve is due to BB recombination.

Fourthly, to clarify which type of recombination exactly is present BT or BI the value of W_1 (γ) and E_a should be compared. In the case when the activation energy is significantly bigger than the γ-value, the recombination is connected to BI transition. If the value of the activation energy is equal to or less than γ, then a BT transition is involved.

Chapter 4

Experimental setup

4.1 Photoluminescence setup

As described in section 3.3 two kinds of PL experiment were performed: excitation intensity dependence and temperature dependence. The former is conducted at constant temperature (the minimum temperature) T~6 K; the later one is conducted at constant excitation intensity (the value depends on the PL intensity of each particular sample). The same experimental setup was used for both types of PL measurements (Figure 4.1). Differences between the equipment used for the experiments on Cu(In,Ga)Se_2 and $Cu_2ZnSnSe_4$ will be indicated where relevant.

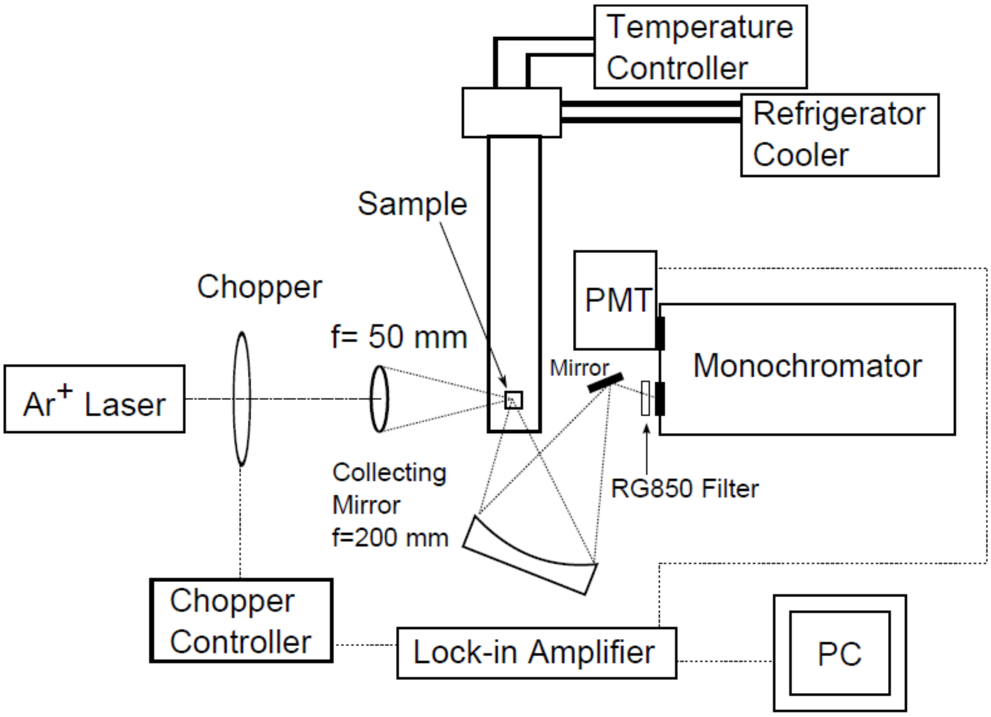

Figure 4.1: The PL setup for measurements of Cu(In,Ga)Se_2 samples.

Laser

A Spectra Physics 177G air-cooled argon ion (Ar^+) laser was used to provide excitation. This laser produces green light at the main (most powerful) line at 514.5 nm. The power output from 20 to 300 mW can be adjustable via the controller.

Bandpass filters

Apart from the main 514.5 nm line the parasitic lines at other wavelengths should be removed from the PL spectra to provide effective excitation without noise. In order to eliminate non-514.5 nm lines from the laser an interference bandpass (BP) filter was applied. The filter has a transmission of ~33% at the 514.5 nm laser wavelength. A blue-green (BG) filter is used to perform a related role, and suppress all lines with wavelength below 470 nm. The BP and BG filters are both placed between the laser aperture and the chamber with the samples.

Chopper & Lock-in amplifier

To increase the sensitivity of the detection system and to reduce the level of noise caused by stray light the continuous laser beam is modulated into a pulsed one by a DC-motor-driven chopper disk, operating at about 35 Hz. This frequency was chosen for the chopping disk because this frequency is not subject of interference from other sources such as mains power (50 Hz & 120 Hz), fluorescent lighting, computer boards etc. The chopper is connected to the lock-in amplifier (Stanford Research Systems SR830) that, in its turn, extracts the signal at the particular frequency of the chopper with a very high signal-noise ratio.

Neutral density (ND) filters

Neutral density filters, inserted into the filter holder between the laser aperture and the sample, were used to attenuate the excitation intensity and achieve the fine tuning of the excitation power for the excitation intensity dependent measurements. The attenuation is described by:

$$\frac{I_{out}}{I_{in}} = 10^{-OD} \tag{4.1}$$

where OD is the optical density of the filter. Filters with OD=0.3; 0.6; 1.0; 2.0 were used individually and in combinations, enabling the laser intensity to be varied by at least 2 orders of magnitude.

Focusing lens

A double convex glass lens (with the short focal length of 10 cm) placed on a translation stage in front of the sample chamber was used to focus and direct the laser beam onto the sample under investigation. Moving this lens towards the sample or away from the chamber adjusts the focus. In the experiments conducted for this study the diameter of the laser spot on the sample was around 0.5 mm. The position of the laser spot on the sample can be adjusted finely by turning the vertical and horizontal handles of a translation stage carrying the lens.

The PL study of CZTS thin films was conducted without the lens to avoid damaging the films by the focused laser beam. This is necessary because of the poor thermal conduction of the glass used as a substrate.

The location of laser spot on the sample surface was observed by a microscope-camera.

Cold finger & Cryopump system

An Advanced Research System CX204AE-x1 Al closed-cycle helium cryopump drives a helium refrigerator connected to the upper end of a cold finger. The samples are mounted on the lower end of the cold finger using indium foil and copper plates to maximise heat transport from the sample.

The temperature of the cold finger is adjusted via a SI-9700-1 Scientific Instruments Temperature Controller to enable temperature-dependent measurements to be performed. The two temperature sensors are Precision Silicon diodes. One is mounted next to the sample holder, the other one is attached to the base of the cold finger. The controller reads the temperature from sensor and operates a heating coil wrapped around the cold finger to increase or decrease the temperature until it reaches the set point. The minimum temperature that can be achieved is ~6 K. It takes about 70 minutes to drop the temperature from room values to minimum. Using the controller, the temperature can be varied with an accuracy of 0.1 K up to room temperature.

To prevent ice formation on the cold finger and also to minimise heat transport from the surroundings, the cold finger is mounted in a vacuum chamber with windows for laser light. The chamber is pumped with a diffusion pump backed with a rotary pump. The base pressure attained is ~$2x10^{-5}$ Torr.

The vacuum chamber with cold finger inside can be raised or lowered and rotated a few degrees to enable different parts of the sample to be excited. By a combination of moving the cold finger and moving the focusing lens, any spot on the sample can be excited.

Spherical mirror

A concave spherical mirror with a diameter of about 12 cm and 25 cm focal length was used to focus the photoluminescence from the sample on to the entrance slit of the monochromator. This mirror can be moved closer to or further away from the chamber with samples and also can also tilted in both the vertical and horizontal planes to enable the light to be better focused on the slit. Since the photoluminescence occurs in the IR part of the spectrum, it is obviously not possible to directly use the PL emission as a guide to adjusting the mirror to focus light on the entrance slit. Instead, the alignment is performed using the diffuse reflection of the green laser light from the sample.

IR-pass filters

Since the laser emits light at 514.5 nm and the wavelengths range used to record the PL spectra covers about 800-1650 nm, the monochromator will detect second-order wavelength at 1029 nm. To prevent this, a high-wavelength bandpass filter Comar RG 850 was used to stop the laser light reflected by the sample. This filter is placed in front of the entrance slit of monochromator and blocks all light with wavelength shorter than 800 nm while transmitting PL with wavelength longer than 900 nm. It has a 50% transmission rate at 850 nm. The filter also minimises detection of stray and fluorescent light by the monochromator.

The Comar RG 850 filter was used when the InGaAs photomultiplier and Ge diode were in operation. When using the PMT R636 a Comar RG 665 filter was used.

Monochromator

A Hilger & Watts 1 m path length monochromator with the Czerny-Turner configuration, a 600 grooves/mm grating and dispersion of 1.67 nm was used to split the light into different wavelengths. The monochromator is fitted with adjustable entrance and exit slits and is rotated by a computer controlled stepper motor.

The spectral resolution of the monochromator is determined by the widths of both the entrance and exit slits and by the diameter of the laser spot on the sample. Since the PL spectra may slightly vary across the excited region on the sample, the spectrum recorded by the monochromator will be an average of the emissions from the sampled area. The effect of any inhomogeneity like this is to broaden the peaks in the spectrum.

By narrowing the slits, the spectral resolution is increased but the intensity of the received signal at the exit slit decreases, hence decreasing the signal-to-noise ratio. It was found that a slit width of 1.5 mm for both entrance and exit slits worked well during the experiments, providing a resolution of 2.5 nm that is equivalent to ~2meV.

Detectors

In this work 3 types of detectors were used to record the light from the monochromator in order to efficiently detect light across all the band gaps of the studied materials (see section 2.4).

For CIGS samples with the 0%, 5%, 10% and 25 % Ga content and also for the CZTSe thin films a Hamamatsu InGaAs photomultiplier tube (wavelength limits 950-1650 nm) with a bias voltage of -500 V was applied.

For the CIGS sample with 50% Ga content an Edinburgh Instruments Ge p-i-n photodiode was chosen. The spectral range of this detector is 300-1700 nm. The photodiode is biased to 100 V with an external high voltage power supply to improve the quantum efficiency of the detector by increasing the depletion layer width. Since the bandgap of germanium is small (0.74 eV), the detector is cooled with liquid nitrogen to reduce the production rate of thermal carriers which would contribute to noise in the detector signal.

Finally, a photomultiplier tube (PMT) R636, bias voltage of 1000 V, wavelength range 200-900 nm, was used for the measurements of CIGS samples with 75% and 100% content of Ga.

In each of the cases described above the signal from the detector is passed to the lock-in amplifier that, in its term, communicates with the computer via a serial RS232 link and the computer records the intensity of the detector signal (in volts).

Software

The PL data were acquired by an “in house” written computer programme that controls the monochromator and reads the signal from the lock-in amplifier.

Through this programme a range of wavelengths to scan, a step of scanning, value of grating and scanning time can be set up.

To analyse the collected PL spectrum and obtain additional data from them the software package Origin was used. The main advantage of this programme is its ability to fit various theoretical curves, including the basic ones (Gaussian and Lorenzian), and more complex curves, to the experimental spectral data obtained. Origin can also fit multiple peaks simultaneously and, moreover, a range of user fitting models can be created and applied.

4.2 X-ray elemental analysis

Electrons bombarding a specimen cause a number of effects, one of which is the emission of characteristic X-rays. The energy or wavelength of the emitted X-rays is then characteristic of the elemental composition of the sample. There are two distinctly different methods to detect characteristic X-rays and obtain information about elemental composition each with its own features. An Energy Dispersive X-ray (EDX) spectrometry counts and sorts characteristic X-rays by their energy, whereas Wavelength Dispersive X-ray (WDX) spectrometry using diffracting crystals to measure and count X-rays according to their wavelength.

Since the studied $CuIn_{1-x}Ga_xSe_2$ samples are monocrystals with cleaved surfaces EDX analysis was chosen to establish the composition of the chalcopyrite samples as this technique is less demanding on the sample flatness and does not require the surface preparation (flattening and polishing) in comparison with WDX analysis. On the other hand, because of the flatness of the kesterite samples and since the WDX analysis provides higher spectral (energy) resolution it was decided to use WDX technique to study the elemental composition in this case.

The EDX analysis of the $CuIn_{1-x}Ga_xSe_2$ samples was performed on the SEM Quanta 250 FEG (FEI) [31]. The WDX analysis of the $Cu_2ZnSnSe_4$ samples was performed on the EPMA system microscope Cameca SX-100 shown on the Figure 4.2 [32].

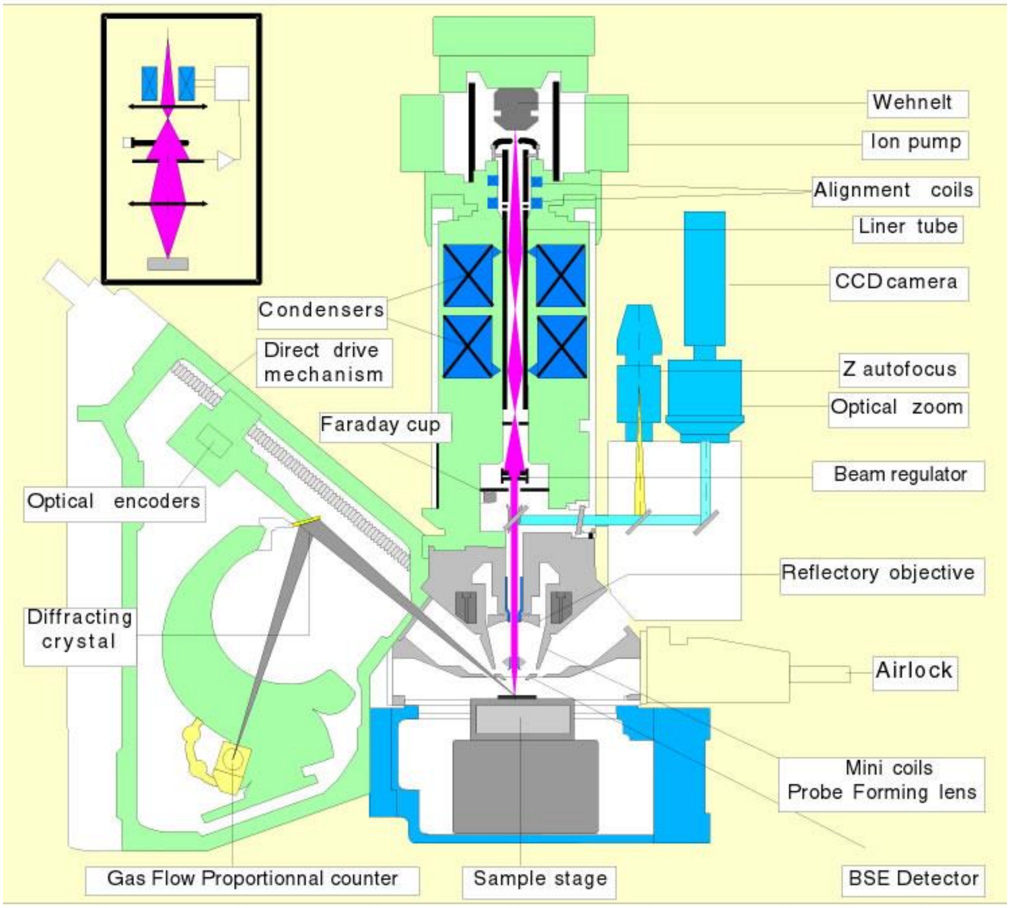

Figure 4.2 – A cutaway view of the Cameca SX-100.

Both techniques (EDX and WDX) work on the following principle. The incident beam excites orbital electrons in an atom inner shell (it can be the K, L or M shells), ejecting it from the shell while creating a hole where the electron was (Fig. 4.3). After that another electron from an outer, higher-energy shell fills that hole, and the difference in energy between the higher- and the lower-energy shell may be released in the form of an X-ray.

The EDX spectrometer measures the number and energy of the X-ray photons emitted from a specimen. As the energies of the X-rays are characteristic of the difference in energy between the two shells and of the atomic structure of the emitting material, EDX allows estimation of the elemental composition of the sample. The resulting energy spectrum exhibits distinctive peaks for the elements present, with the peak area indicating the elements’ concentrations.

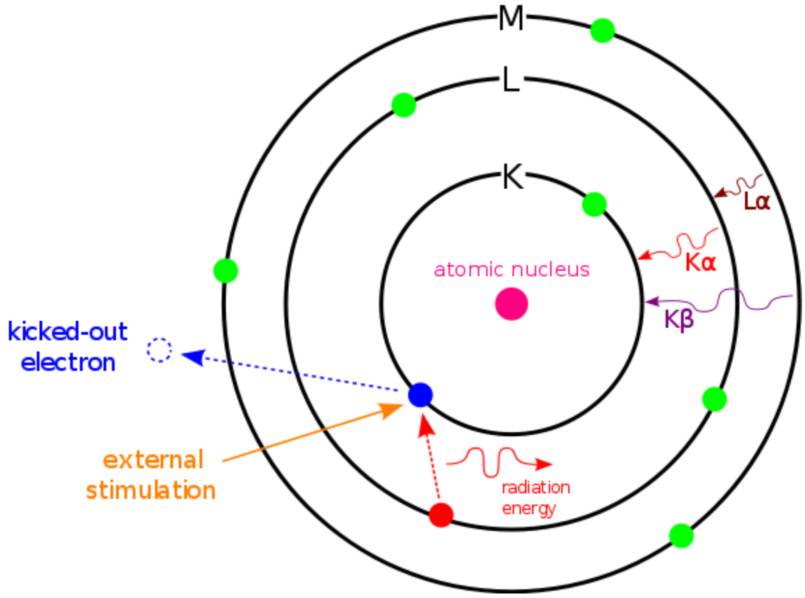

Figure 4.3 – Principle of EDX and WDX.

The WDX, in its turn, uses Bragg scattering of X-rays by a diffracting crystal, which obeys Bragg's law to select the wavelength for analysis and diffract characteristic X-rays. The crystal or grating (of known lattice spacing d) is located between the sample and the detector. The angle of diffraction is a function of the X-ray wavelength and the crystal is mechanically scanned through a range of angles while a detector measures varying intensity. Different crystals are effective for different elements due to their various spacing.

The geometry of the WDX spectrometer represents the following (Fig. 4.4). The sample, crystal and detector must lie on a so-called Rowland circle and remain on it to focus the characteristic X-rays effectively for all wavelengths being measured. The sample is fixed, therefore only the crystal and detector could be moved to remain on the Rowland circle with change in wavelength.

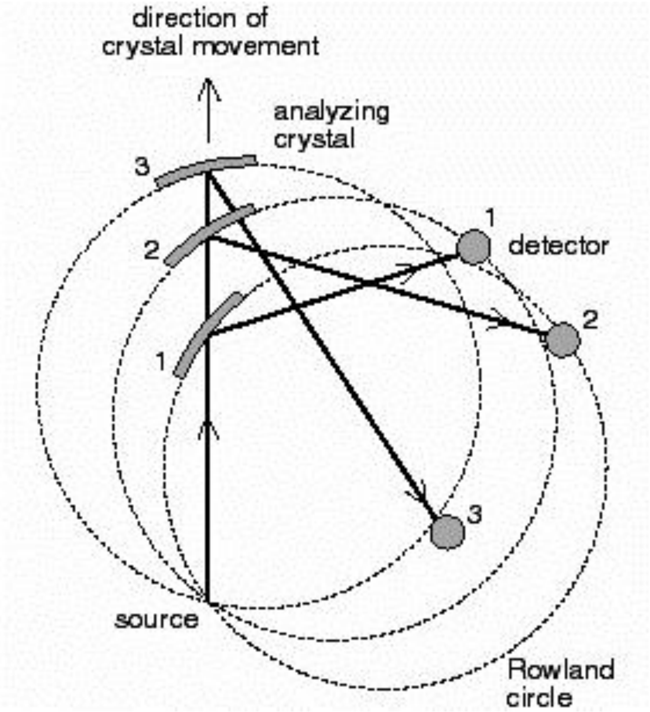

Figure 4.4 – Principle of the WDX.

For both kinds of analysis the samples is mounted on a sample holder in an evacuated chamber and the system is first calibrated using reference elements and the intensity of the X-rays emitted measured. Measurements are then run on the sample and the relative intensities of the emitted X-rays compared. After some processing this gives an indication of the composition of the sample. The WDX technique provides the accuracy and better resolution rather than the EDX, but is slow and can measure only one element each time. However, the EDX spectrometry is faster and easier and can measure all elements at once.

The elemental composition of the CZTSe thin films was determined by WDX as the averaging over 10-point linear scans, whereas for the CIGSe single crystals due to lack of time the elemental compositions were determined by EDX as a single point scan for each sample.

Chapter 5

Results and interpretation

5.1 PL results

This chapter will describe PL data from the series of CIGSe and CZTSe samples described in chapter 2. Intensity and temperature dependent PL spectra for each particular sample, additional fitted functions discussed in section 3.3 as well as descriptions for them are shown in the subsections from 5.1.1 up to 5.1.10. The summary tables will be shown after subsections 5.1.8 and 5.1.10.

5.1.1 CIGSe samples spectra

The spectral position of the dominant peaks in all the $CuIn_{1-x}Ga_xSe_2$ samples was changing gradually with increase in x from 0 to 1 as shown in Fig.5.1. All spectra were obtained at 6 K with 20mW laser excitation power. Blue ticks indicate the position of energy maxima, while the values of the band gap energy taken from section 2.4 are marked in red colour.

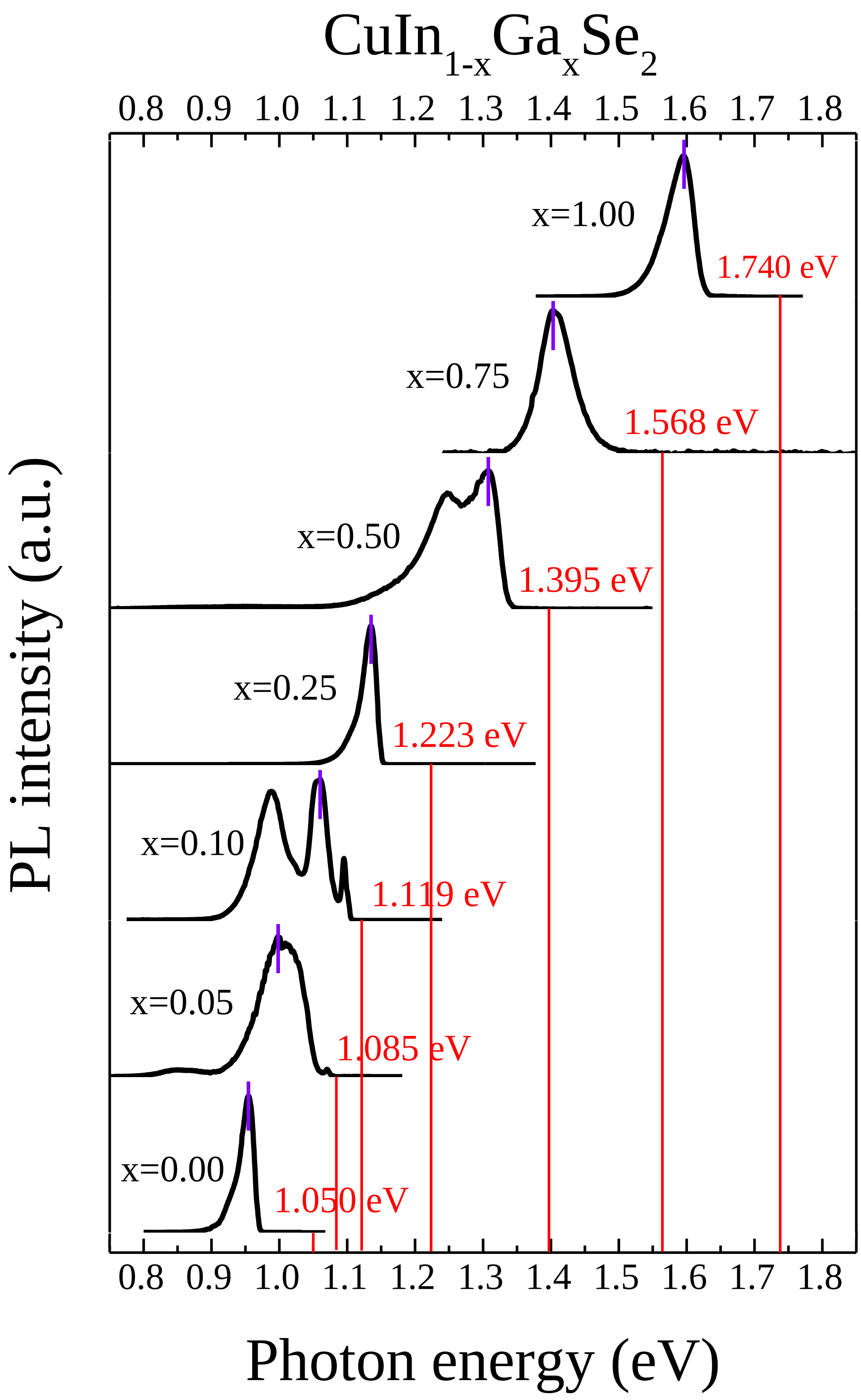

Figure 5.1: Normalized PL spectra of $CuIn_{1-x}Ga_xSe_2$ with different Ga content along with estimated bandgaps shown by red lines.

5.1.2 $CuInSe_2$ (x=0.00)

Excitation intensity and temperature dependent PL spectra from $CuInSe_2$ are shown in Figure 5.2 and Figure 5.3.

In the excitation intensity dependence diagram shown in Figure 5.2a only one peak can be clearly observed, that shows a blue shift with increase in excitation intensity. In order to easily trace how the spectral peak position changed during the measurements black straight line is shown in Figure 5.2a and in all successive figures reflecting excitation intensity and temperature dependencies. Although a j-shift of 2.6 meV/decade (Figure 5.3c) can originate from a DAP transition it also does not contradict the assignment to the BI recombination. Here the k-value is less than 1 (Figure 5.2b), indicating that the recombination is defect based as described in section 3.3.

According to the temperature dependence, at 6 K the spectrum is dominated by one peak at 0.95 eV, but at higher temperatures (above 60 K) a second peak at 0.98 eV appears (the spectrum marked by the ellipse in Figure 5.3a). Starting from 140 K only the second peak is visible (the spectrum marked by another ellipse in Figure 5.3a). With increase in temperature from 6 K the low energy peak firstly exhibits a shift towards lower energies, reaching a minimum of 0.94 eV at a temperature of T_{min}=62.5 K, then begins to shift towards higher energies (Figure 5.3b). According to the sequence of PL data analysis discussed in section 3.3, this suggests that this peak is due to either BI or BT recombination.

To prove the presence of the BI recombination the γ-value shown in Figure 5.3d, derived from asymmetric sigmoidal function fitting (discussed in PL peaks identification section 3.3) was compared with values of activation energy. The activation energies derived from fitting by the Arhenius-2 model are 44 meV and 15.5 meV (Figure 5.3c). In this case E_a of 44 meV is much greater than γ of 14 meV, and, following the sequence of PL data analysis shown in section 3.3, we can firmly conclude that it is a BI transition. We assume that the band might have two non-resolved peaks corresponding to BI with greater E_a and BT on the high energy side with smaller E_a.

As the high energy peak becomes visible at quite high temperatures and exhibits a further shift to higher energies at increasing temperatures, it can be tentatively assigned to a BB transition as explained in section 3.2.

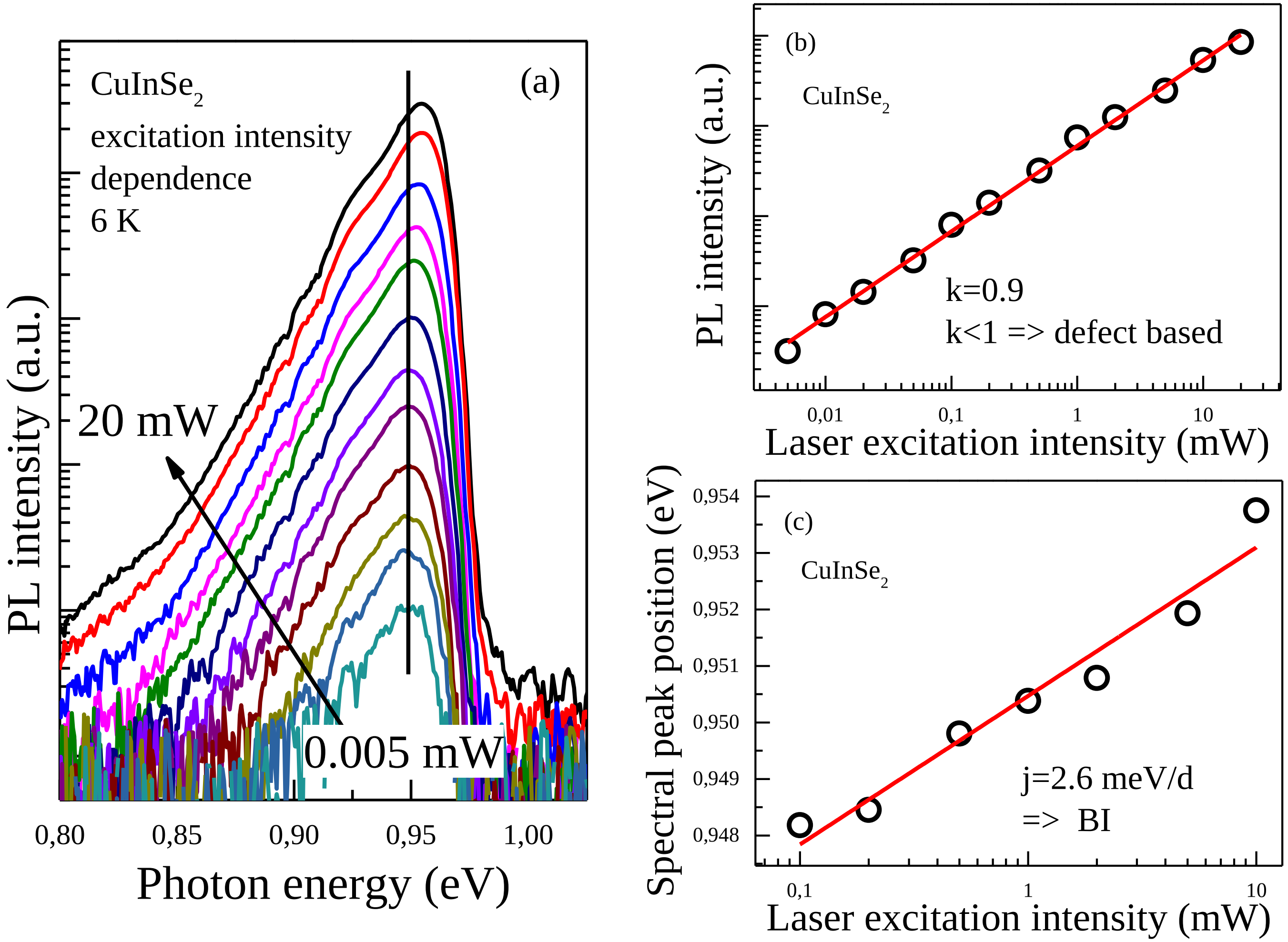

Figure 5.2: (a) Excitation intensity dependence, (b) k-value plot and (c) j-shift plot from CuInSe$_2$.

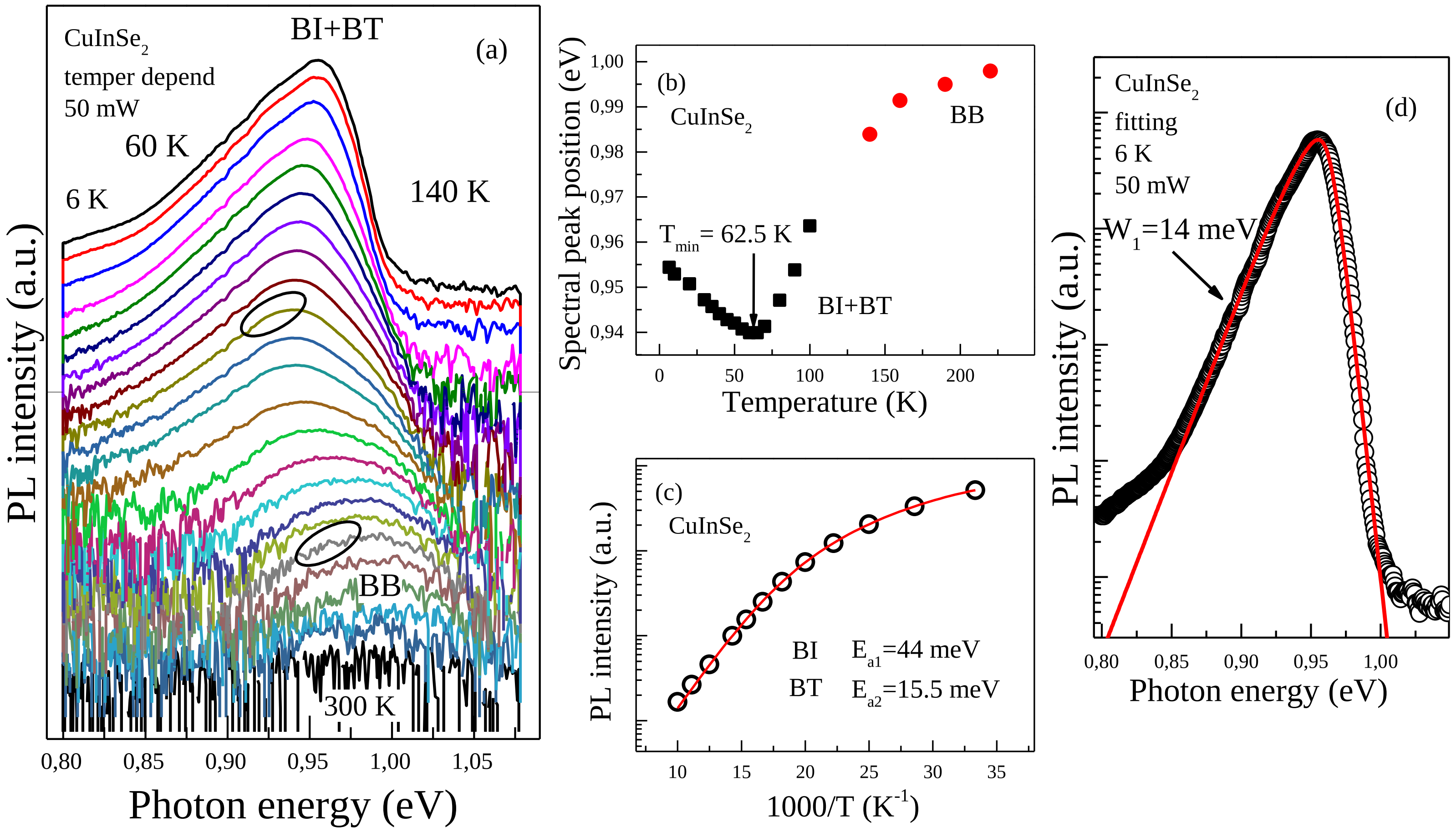

Figure 5.3: (a) Temperature dependence, (b) peak energy vs. temperature plot, (c) log(peak PL intensity) vs.1000/temperature plot and (d) fitting of PL spectrum at 6 K and 50 mW by double sigmoid function from CuInSe$_2$.

5.1.3 $CuIn_{0.95}Ga_{0.05}Se_2$ (x=0.05)

At 6 K and 20 mW excitation intensity there were several poorly resolved peaks in the PL spectra of $CuIn_{0.95}Ga_{0.05}Se_2$ (Fig. 5.4a). The most intense peak is observed at 1.00 eV. With an increase in the excitation intensity the spectral position of that peak moved to higher energies with a j-shift of 11 meV/d (Fig. 5.4c). The k-value was 0.94 (Fig. 5.4b), indicating that recombination is defect associated.

With increasing temperature (Fig. 5.5a) the spectral peak position of the most intense peak firstly shifted to lower energies, reaching a minimum of 1.02 eV at 55 K, and then moved towards higher energies (Fig. 5.5b). This is a characteristic pattern for either BI or BT recombination. Comparing the E_a value of 31 meV shown in Figure 5.5c and the maximum γ-value among all the CIGSe samples (20 meV) that will be discussed later on, we can assign this band to the BI recombination. However, since the PL spectra of $CuIn_{0.95}Ga_{0.05}Se_2$ contain a set of unresolved peaks, this result is inconclusive.

It is remarkable that the PL spectra of $CuIn_{0.95}Ga_{0.05}Se_2$ contained very narrow, weak peaks, which can very likely be excitonic features. To clarify this, these features were studied separately in a more detailed way (Fig. 5.6 and 5.7). In a closer view (Fig. 5.6a) two bands centered at 1.07 eV and 1.08 eV are seen. Firstly, the k-value of these peaks obtained through the excitation-dependence measurement is 1.2 and 4.6, respectively (Fig. 5.6b). Secondly, the spectral peak position of these bands does not change with increase in excitation intensity (Figure 5.6c). These prove that these peaks have the excitonic nature.

The untypically high value of k-coefficient of 4.6 (as a rule k-value for excitons does not exceed 2) can be explained by poor resolution. The free exciton peak is not resolved, thus to separate this peak from the bound exciton peak they were fitted with two Gaussian peaks. However, we do not know how many peaks actually were there. It can be three or more peaks that were not taken into account. From the point of view of the spectral peak position and intensity the consideration through the fitting of unresolved peaks is very approximate and can lead to errors. However, the k-value of 2.2 and 3.5 (but for devices, not for single crystals) was reported in [33] for ZnO/CdS/CIGS/Mo short-circuited solar cells and solar cells without load.

Through the temperature-dependent measurement (Fig. 5.7) the PL intensity of the excitonic peaks at 80 mW excitation and 6 K was very low (~4 mV) and there were too few experimental points to perform the Arrhenius analysis and obtain a value for the binding energy. Although the parameters could not be quantitatively calculated, it is qualitatively seen that there are 2 excitons: one bound exciton (BE) and one free exciton (FE), since the former quenched faster (by ~20-30 K) whereas the latter quenched more slowly (by ~55 K) (see section 3.2).

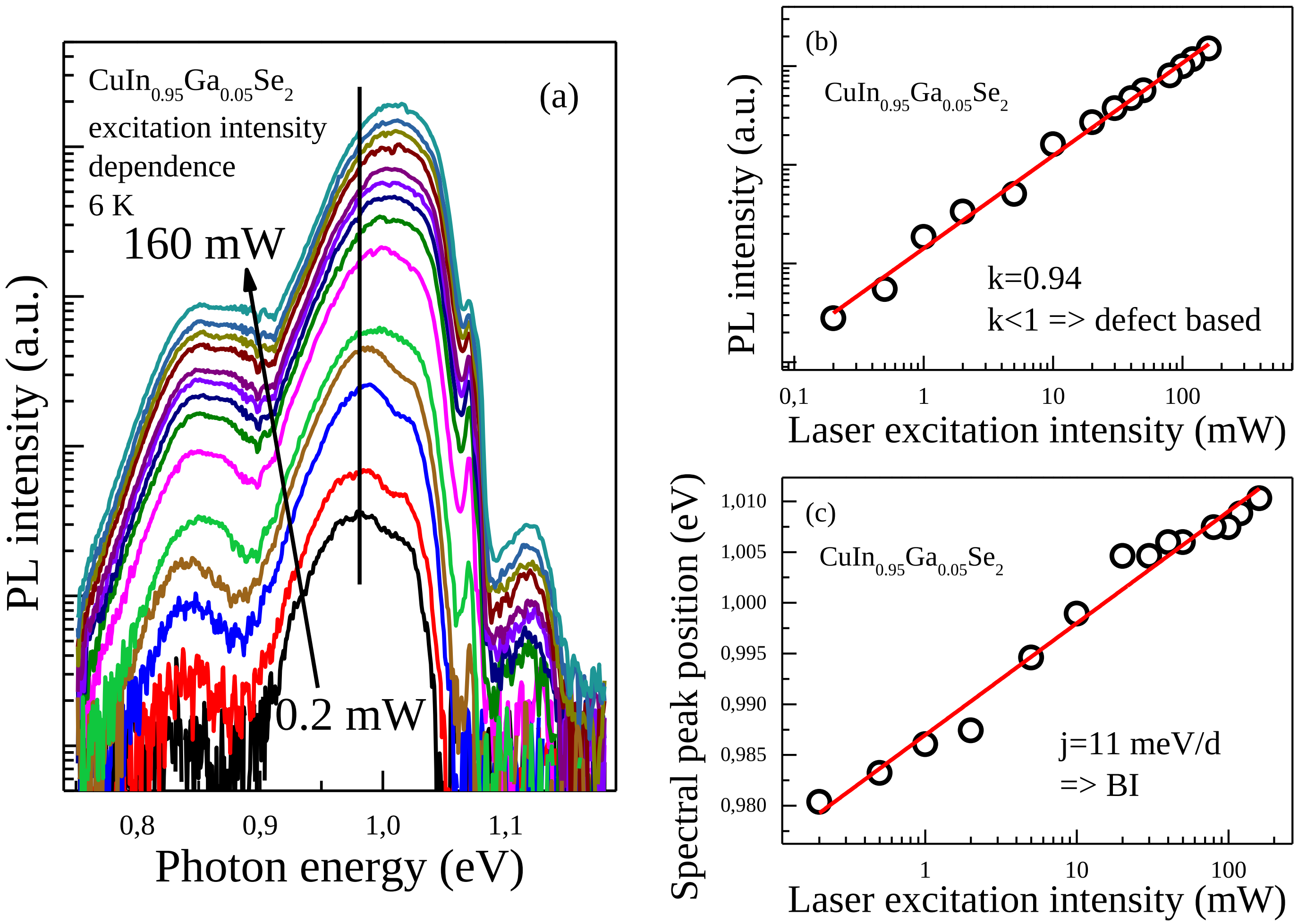

Figure 5.4: (a) Excitation intensity dependence, (b) k-value plot and (c) j-shift plot from CuIn$_{0.95}$Ga$_{0.05}$Se$_2$.

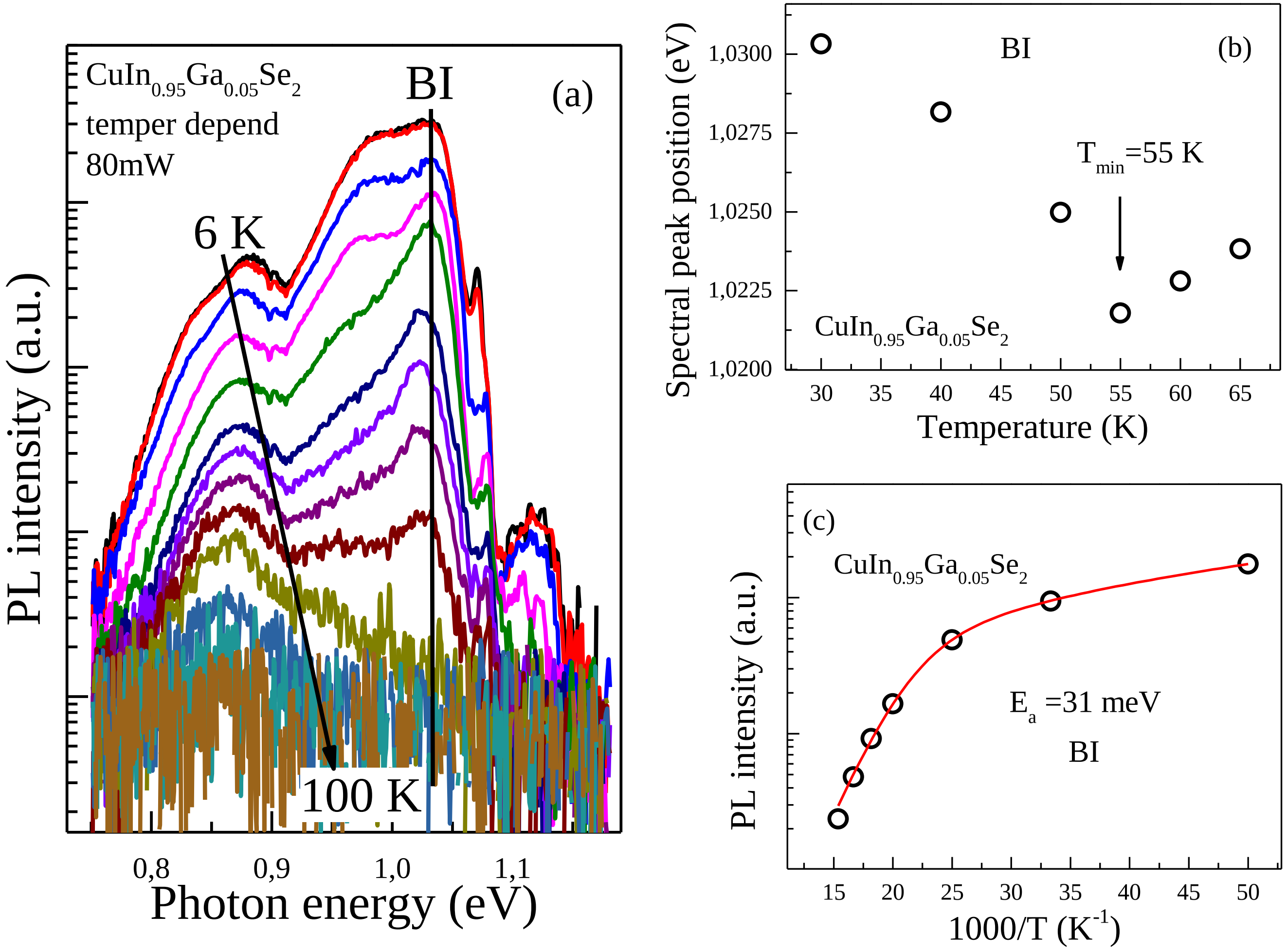

Figure 5.5: (a) Temperature dependence, (b) peak energy vs. temperature plot and (c) log(peak PL intensity) vs. 1000/temperature plot from $CuIn_{0.95}Ga_{0.05}Se_2$.

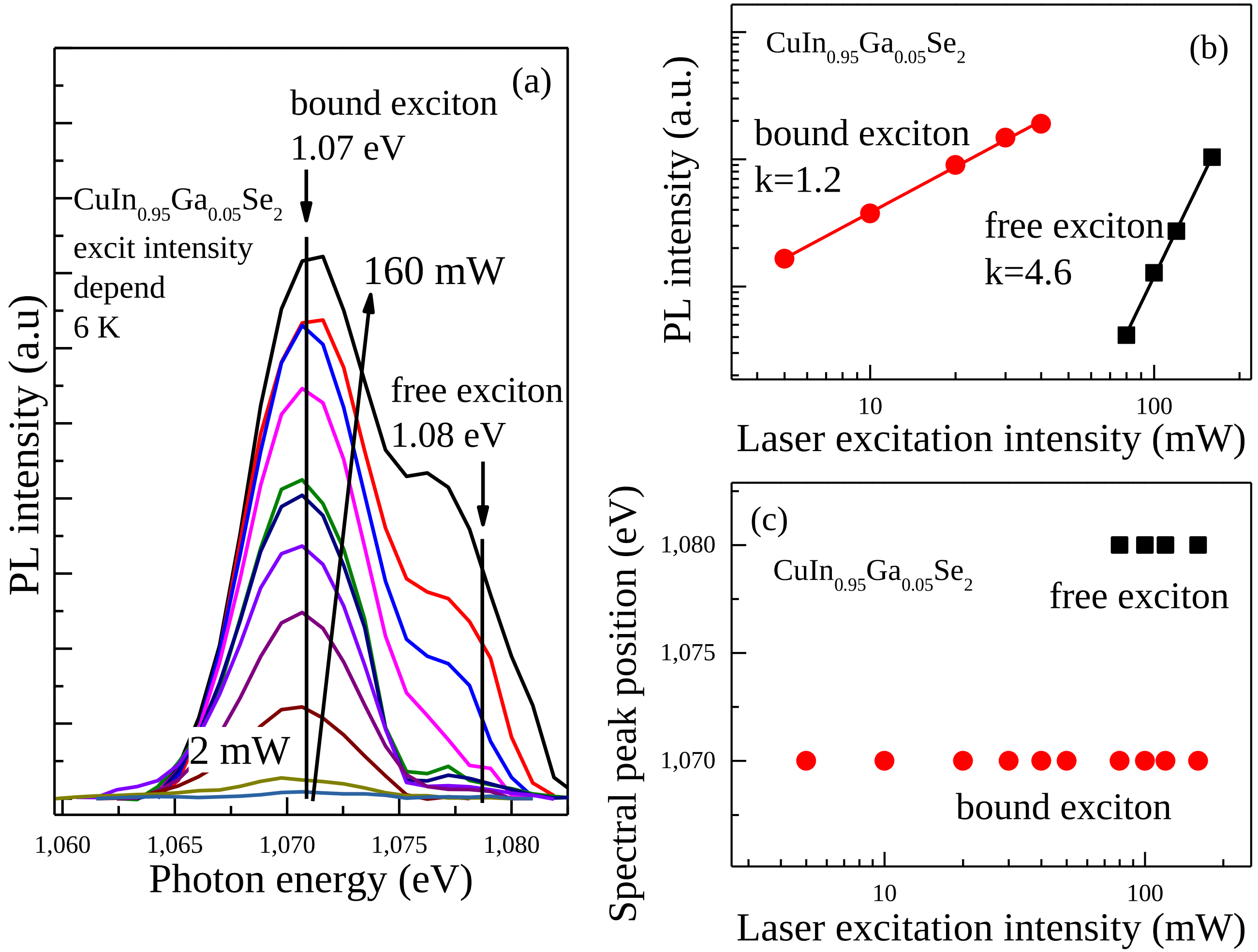

Figure 5.6: (a) Excitation intensity dependence, (b) k-value plot and (c) j-shift plot of excitonic PL spectra from $CuIn_{0.95}Ga_{0.05}Se_2$.

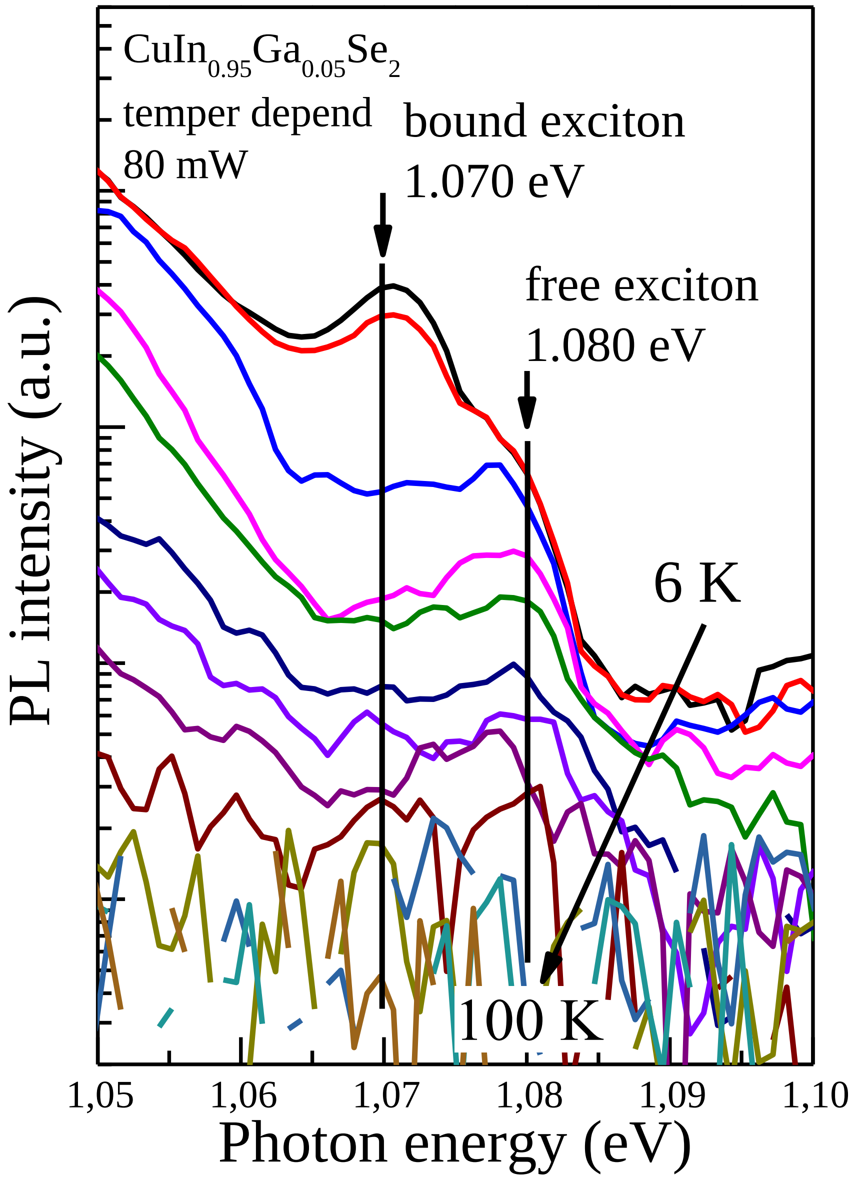

Figure 5.7: Temperature dependence of excitonic PL spectra from $CuIn_{0.95}Ga_{0.05}Se_2$.

5.1.4 $CuIn_{0.90}Ga_{0.10}Se_2$ (x=0.10)

Similar to the $CuIn_{0.95}Ga_{0.05}Se_2$ sample, the PL spectra at 6 K and 20 mW of the sample with 10% Ga content contain several non-resolved and resolved high energy peaks (Figure 5.8a) at 0.995 eV, 1.063 eV and 1.095 eV with PL intensity of 21, 29 and 17 a.u., respectively. The increasing excitation intensity moves the most intense peak to higher energy with a j-shift of around 5.3 meV/d (Fig. 5.8c), whereas its intensity rises with a k-value of 0.93 (Figure 5.8b).

At low temperatures (Figure 5.9a) the spectral position of the dominant peak redshifts until the temperature of 60 K, reaching the minimum of 1.056 eV and then starts blueshifting (Figure 5.9b). From the Arrhenius analysis (Figure 5.9c) an activation energy of 23 meV was obtained. This E_a value is almost equal to γ suggesting that the band is a BT recombination mechanism. The rather small for a BT recombination value of the j-shift can be explained by the fact that in the spectra of $CuIn_{0.90}Ga_{0.10}Se_2$ there was a set of unresolved peaks, causing significant uncertainties.

As with the $CuIn_{0.95}Ga_{0.05}Se_2$ sample, this 10% sample also shows narrow non-intense peaks that look like excitons. These peaks were investigated more closely (Figures 5.10 and 5.11). At 6 K and 20 mW there were clearly seen two merged peaks, the first peak was located at 1.095 eV and the second one was centered at 1.101 eV (Figure 5.10a). With increase in excitation intensity the k-values of 1.45 and 1.6, respectively, were obtained (Figure 5.10b). These values are more than 1, and it is the first proof of the excitonic nature of these peaks. The second proof is that the spectral peak position is not changing over the excitation-dependent measurement (Figure 5.10c).

On the temperature dependence plot two peaks can be also observed at 1.095 eV and 1.101 eV (Figure 5.11a). Increasing temperature quenches the lower energy peak by 30 K whereas the higher energy peak, in its turn, quenched at the higher temperature of 60 K. This suggests that the peak centered at 1.095 eV can be assigned to a BE and the other peak is associated with FE recombination. The spectral peak position of these two peaks remained the same through the temperature-dependent measurement (Figure 5.11b). From the Arrhenius analysis E_a of 19 meV was obtained for free exciton that is in agreement with the value in [34].

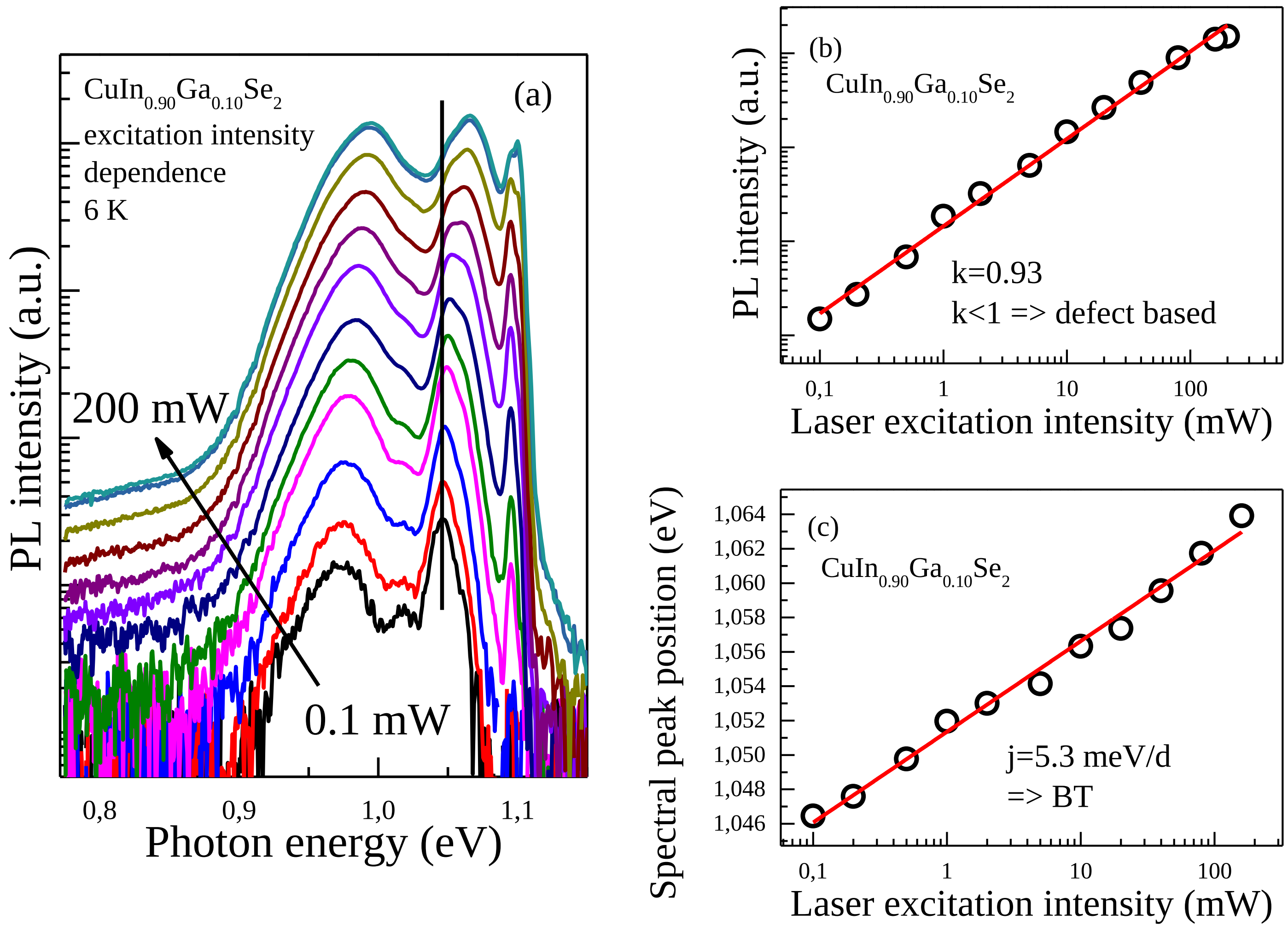

Figure 5.8: (a) Excitation intensity dependence, (b) k-value plot and (c) j-shift plot from CuIn$_{0.90}$Ga$_{0.10}$Se$_2$.

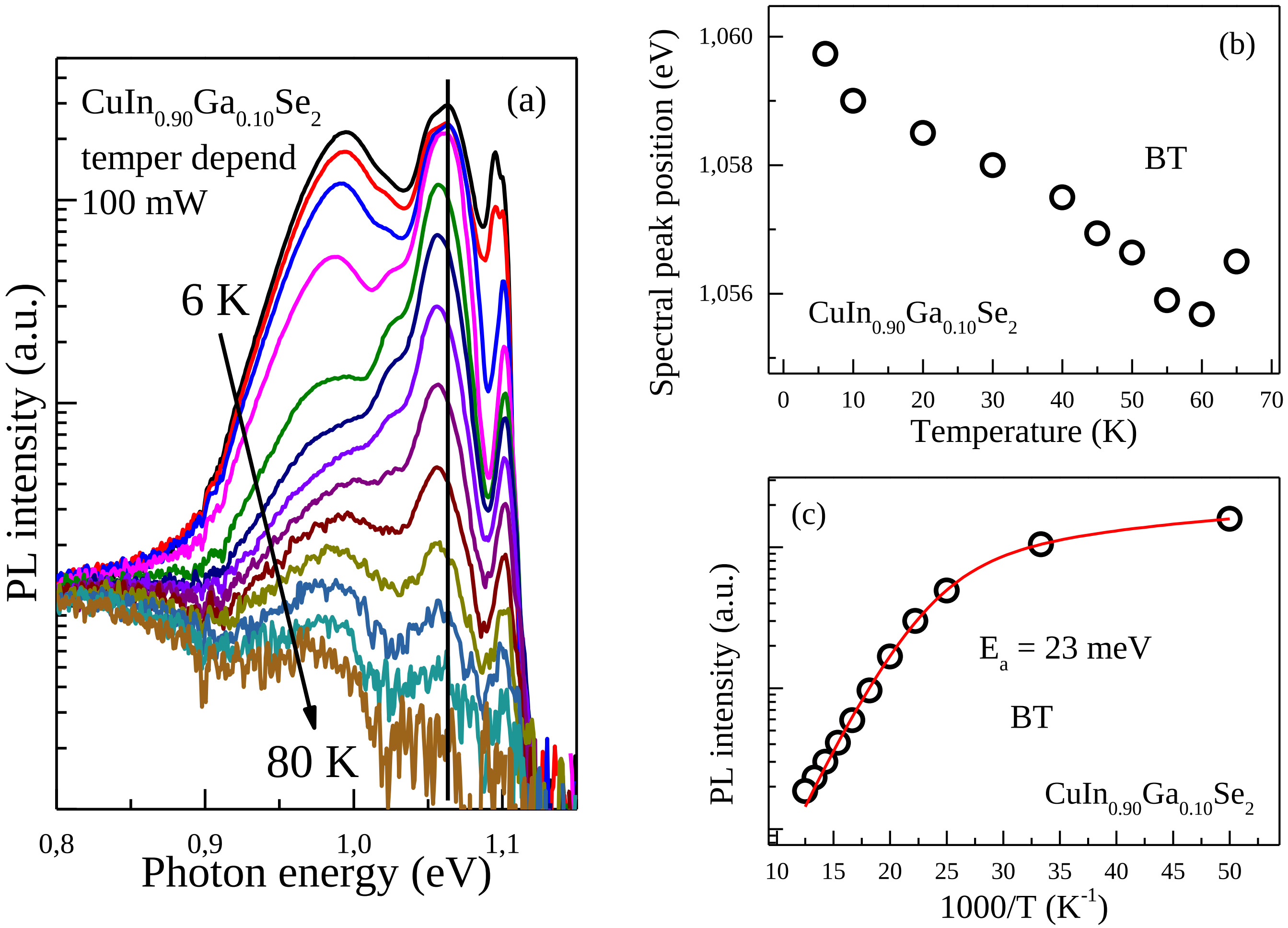

Figure 5.9: (a) Temperature dependence, (b) peak energy vs. temperature plot and (c) log(peak PL intensity) vs. 1000/temperature plot from $CuIn_{0.90}Ga_{0.10}Se_2$.

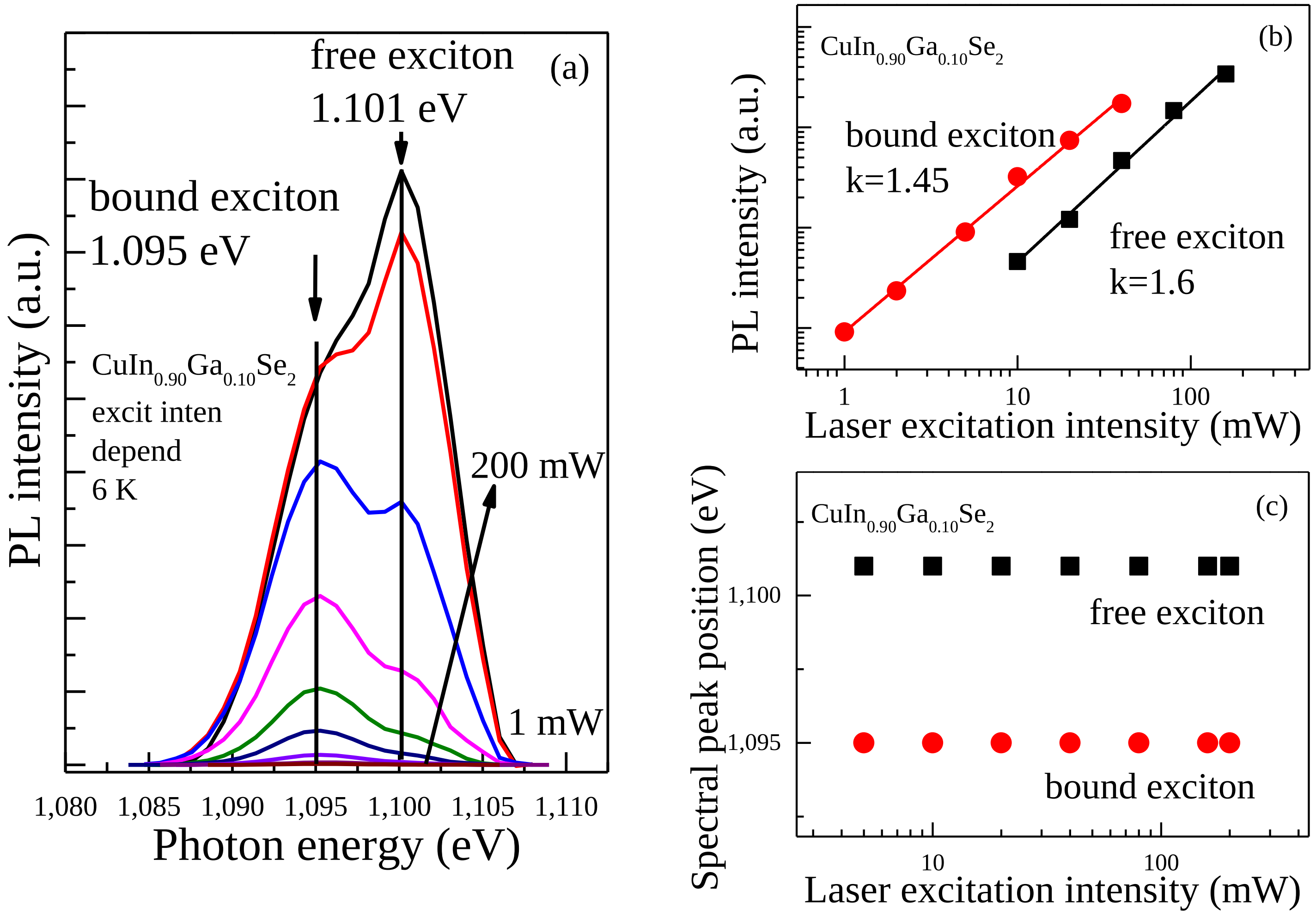

Figure 5.10: (a) Excitation intensity dependence, (b) k-value plot and (c) j-shift plot of excitonic PL spectra from $CuIn_{0.90}Ga_{0.10}Se_2$.

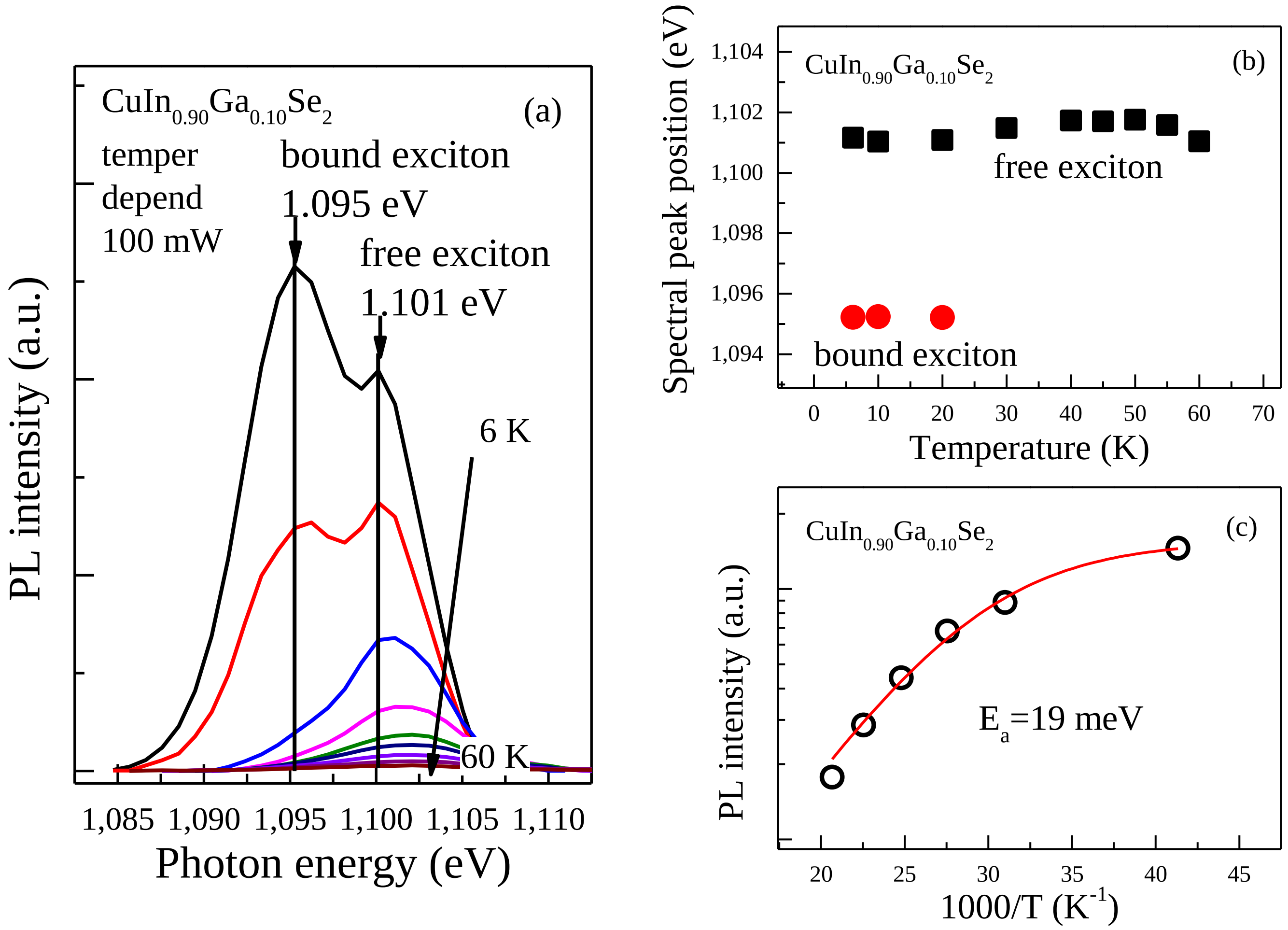

Figure 5.11: (a) Temperature dependence, (b) peak energy vs. temperature plot and (c) log(peak PL intensity) vs. 1000/temperature plot of excitonic PL spectra from $CuIn_{0.90}Ga_{0.10}Se_2$.

5.1.5 $CuIn_{0.75}Ga_{0.25}Se_2$ (x=0.25)

At 6 K and excitation intensity of 20 mW the spectrum of $CuIn_{0.75}Ga_{0.25}Se_2$ shows several peaks in the 0.90-1.15 eV range with one dominant and well-resolved peak at 1.13 eV (Figure 5.12a). This peak has a characteristic asymmetrical shape with a very abrupt high energy side and gentler low energy side. The recombination mechanism of this band is associated with defects, because the k-value of 0.94 is less than 1 (Figure 5.12b). With increase in laser excitation intensity the peak position moves to higher energies with a j-shift of about 3 meV/decade as shown in Figure 5.12c. However, this value does not provide a clear answer on the type of recombination involved.

The peak position in the temperature dependence (Figure 5.13a) initially shifts towards lower energies, reaching a minimum of 1.131 eV at T_{min}=30 K, and then starts to move to higher energies as shown in Figure 5.13b. In this case E_a obtained from the Arrhenius analysis and γ derived from fitting (Figure 5.13c and 5.13d) are similar, 13 meV and 17 meV, respectively. This suggests that this peak is likely to be due to a BT transition.

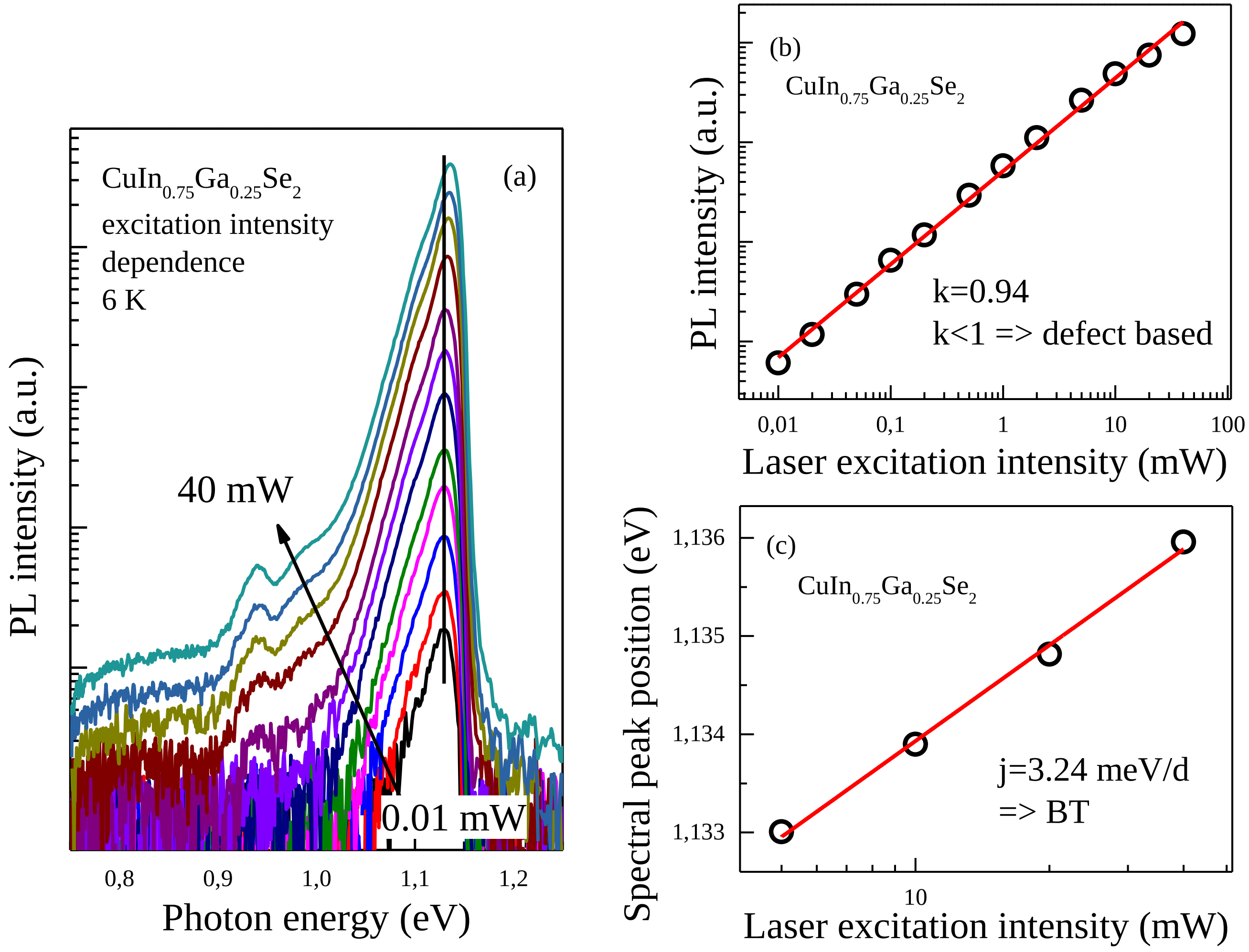

Figure 5.12: (a) Excitation intensity dependence, (b) k-value plot and (c) j-shift plot from CuIn$_{0.75}$Ga$_{0.25}$Se$_2$.

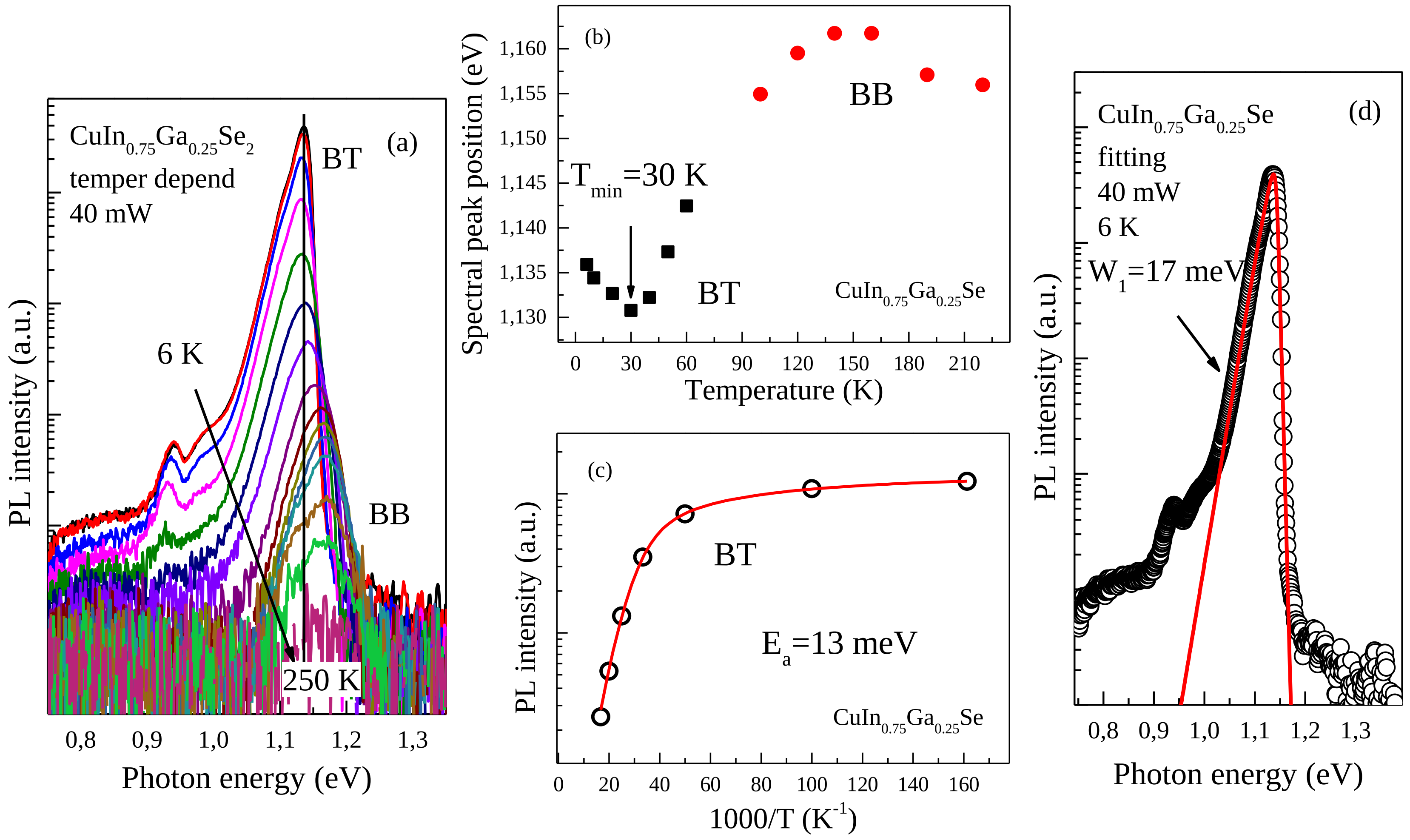

Figure 5.13: (a) Temperature dependence, (b) peak energy vs. temperature plot, (c) log(peak PL intensity) vs.1000/temperature plot and (d) fitting of PL spectrum at 6 K and 40 mW by double sigmoid function from $CuIn_{0.75}Ga_{0.25}Se_2$.

5.1.6 $CuIn_{0.50}Ga_{0.50}Se_2$ (x=0.50)

At a temperature of 6 K and laser excitation power of 20 mW there are 2 resolved peaks in the PL spectrum of $CuIn_{0.50}Ga_{0.50}Se_2$. The first one is centered at 1.234 eV, whereas the second dominates at these conditions and located at 1.280 eV (Figure 5.14a). The k-values for both peaks are similar and less than 1, at 0.88 and 0.87, respectively (Figure 5.14b and 5.14c), indicating that their recombination mechanism is defect based. As the excitation intensity increases the spectral position of both peaks shifts to higher energies with j-shifts of 7.3 meV/d and 10.63 meV/d, respectively (Figure 5.14d and 5.14e).

Although we fit the peaks with the double sigmoid functions, the bands overlap which makes it difficult to analyse their excitation intensity and temperature dependencies. In the temperature dependence (Figure 5.15a) the spectral position of both resolved peaks (1.242 eV and 1.300 eV) firstly shifts towards lower energies, reaching a minimum of 1.188 eV and 1.270 eV, respectively, at 50 K, and then starts to move toward higher energies (Figure 5.15b and 5.15c). This is a characteristic pattern for the BT or BI recombination. To clarify which type of recombination is involved the values of γ and E_a were compared. However we cannot accurately fit the low energy sides of these overlapped peaks therefore γ = 20 meV (Figure 5.16c and 5.16d) is only an estimate value. Here both E_{a1}=16 meV and E_{a2}=13 meV (Figure 5.16a and 5.16b) are close to γ. However, the peak 1 quenches later, whereas the peak 2 quenches earlier, therefore we can assume that the higher energy peak can be due to a BT recombination mechanism, whereas the lower energy band is likely to be a BI transition. At higher temperatures we can see the BB transition.

Additionally, a third peak appears at lower energy (1.131 eV) and looks like a series of phonon satellites from a main peak (Figure 5.16c). For example, the Longitudinal Optical (LO) phonons in $CuInSe_2$ and $CuGaSe_2$ with energies of 29 meV and 33 meV, respectively, were reported in [35, 36]. However, in our case intervals between the peaks (marked in red in Figure 5.15a) are 58 meV and 111 meV and not equal. Also the spectra in Figure 5.14a indicate this is not the case as the second peak is the most intense, therefore we can conclude that it is not the phonon satellites.

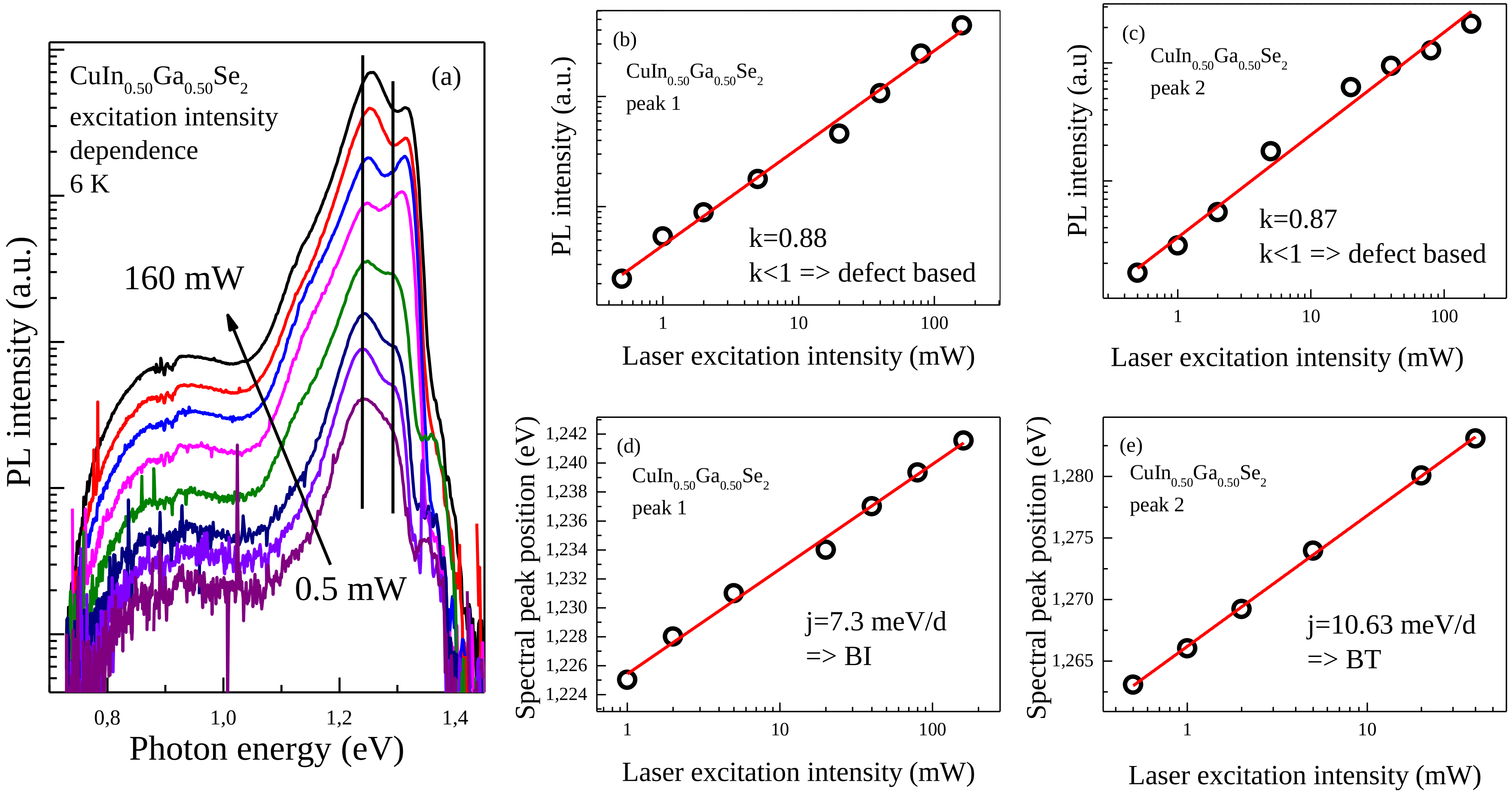

Figure 5.14: (a) Excitation intensity dependence; (b), (c) k-value plots for peak 1 and peak 2; (d), (e) j-shift plots for peak 1 and peak 2 from $CuIn_{0.50}Ga_{0.50}Se_2$.

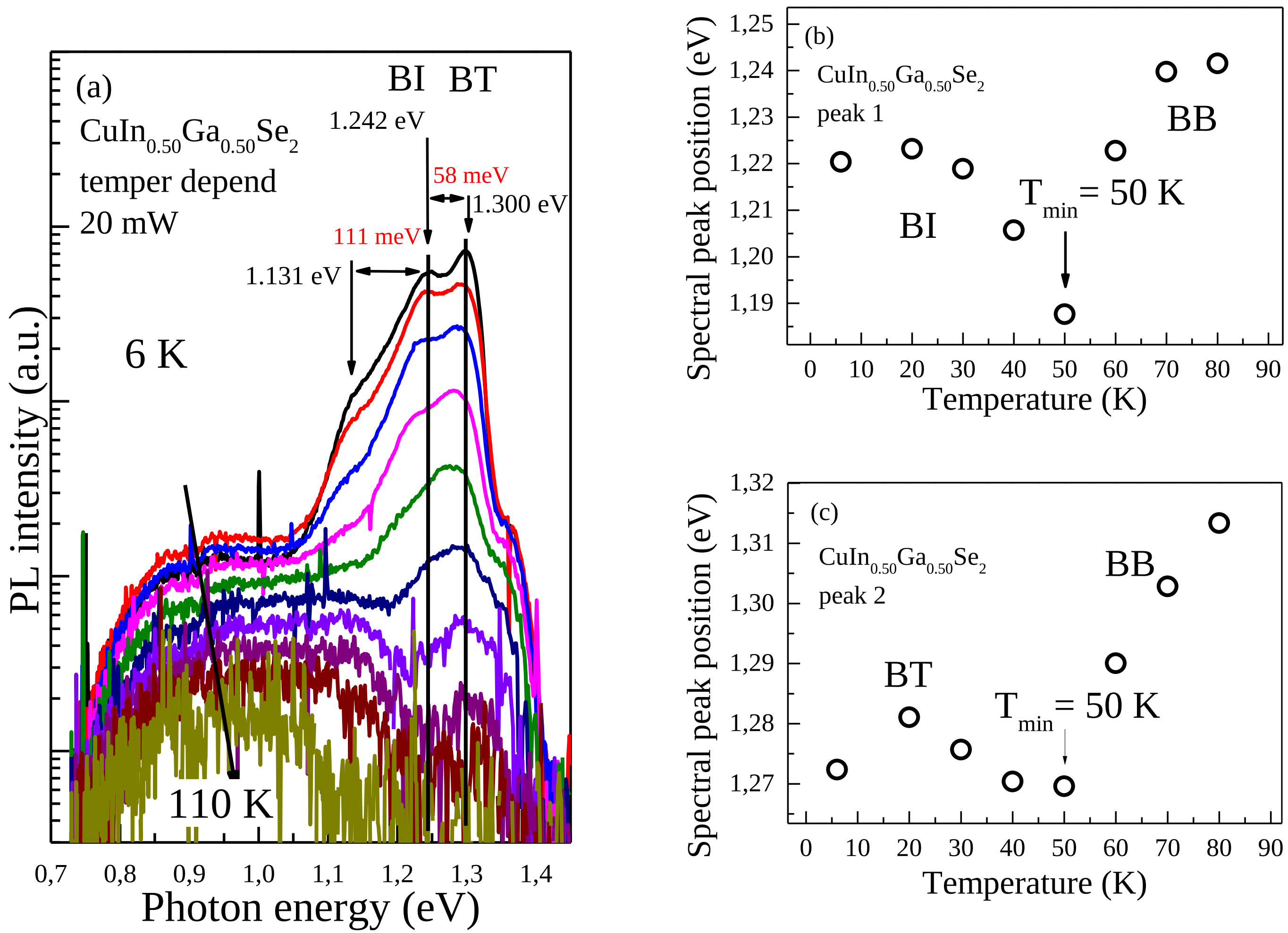

Figure 5.15: (a) Temperature dependence; (b), (c) peak energy vs. temperature plots for peak 1 and peak 2 from $CuIn_{0.50}Ga_{0.50}Se_2$.

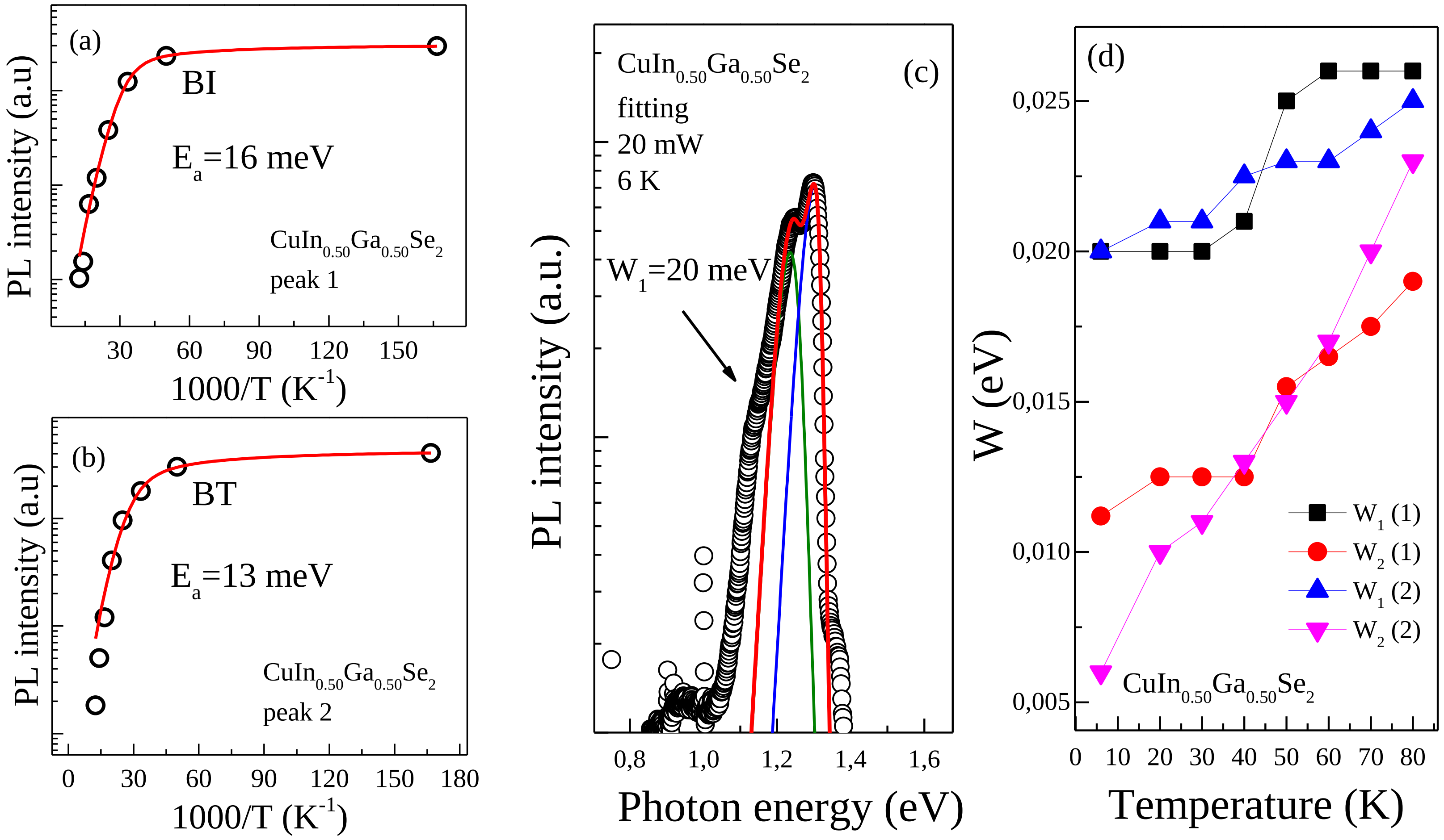

Figure 5.16: (a), (b) log(peak PL intensity) vs.1000/temperature plots for peak 1 and peak 2; (c) fitting of PL spectrum at 6 K and 20 mW by double sigmoid function; (d) temperature dependence of fitting parameters W_1 and W_2 from $CuIn_{0.50}Ga_{0.50}Se_2$.

5.1.7 $CuIn_{0.25}Ga_{0.75}Se_2$ (x=0.75)

At 6 K and excitation intensity of 20 mW just one peak at 1.41 eV can be observed in the PL spectra of $CuIn_{0.25}Ga_{0.75}Se_2$ shown in Figure 5.17a. Unlike the shape of the bands of the other samples in this case the PL band is almost symmetrical (at low excitation intensities) with an intensity independent low energy side and intensity dependent high energy side. A k-value of 0.81 < 1 suggests a defect related recombination (Figure 5.17b). The spectral peak position shows a blue shift with increasing excitation intensity, giving a j-shift of ~5 meV/decade (Figure 5.17c).

With increasing temperature the spectral peak position shifts to higher energies (Figure 5.18a). The characteristic pattern shown in Figure 5.18b implies that here a DAP recombination is involved. For this sample E_a=48 meV (Figure 5.18c).

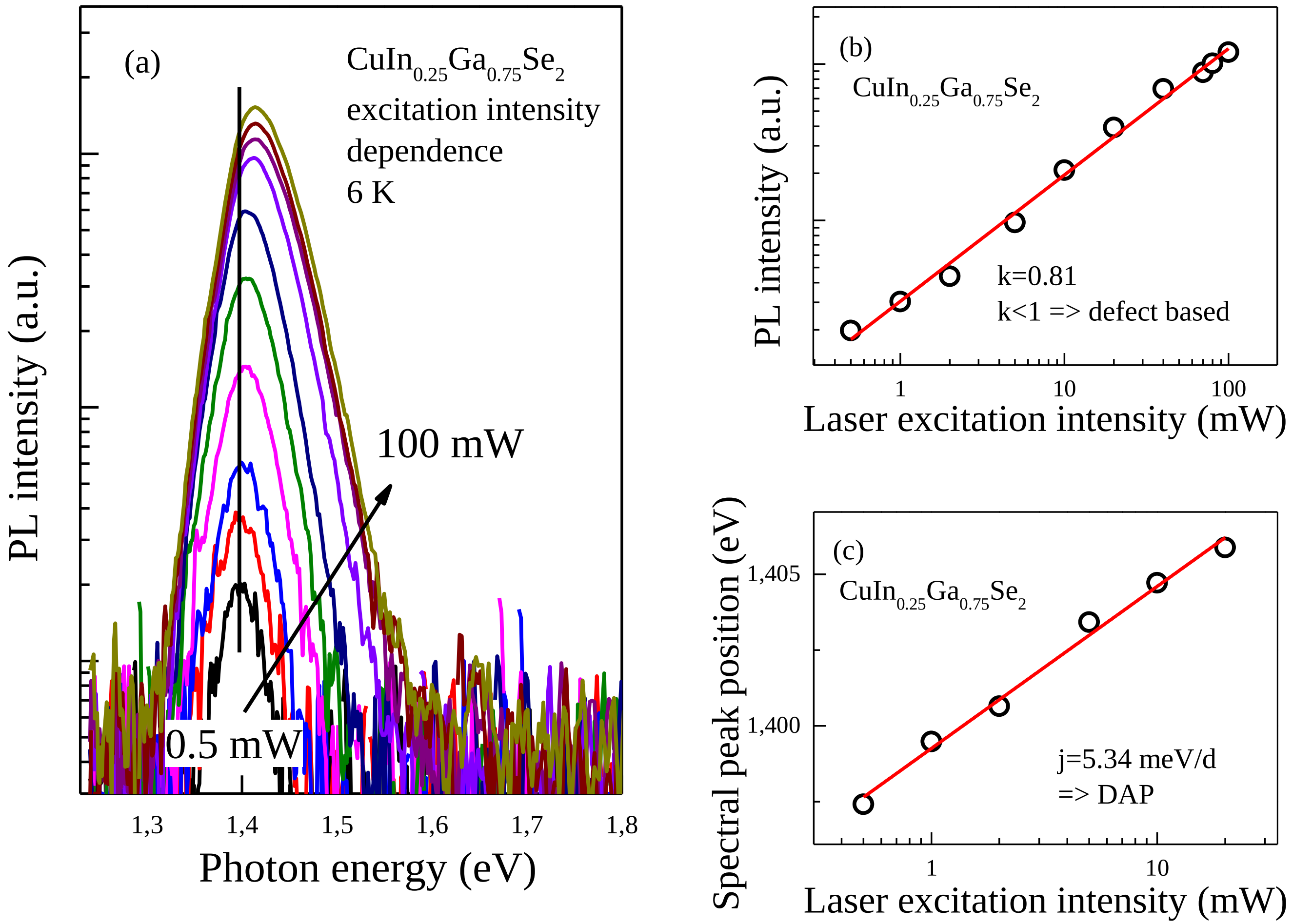

Figure 5.17: (a) Excitation intensity dependence, (b) k-value plot and (c) j-shift plot from $CuIn_{0.25}Ga_{0.75}Se_2$.

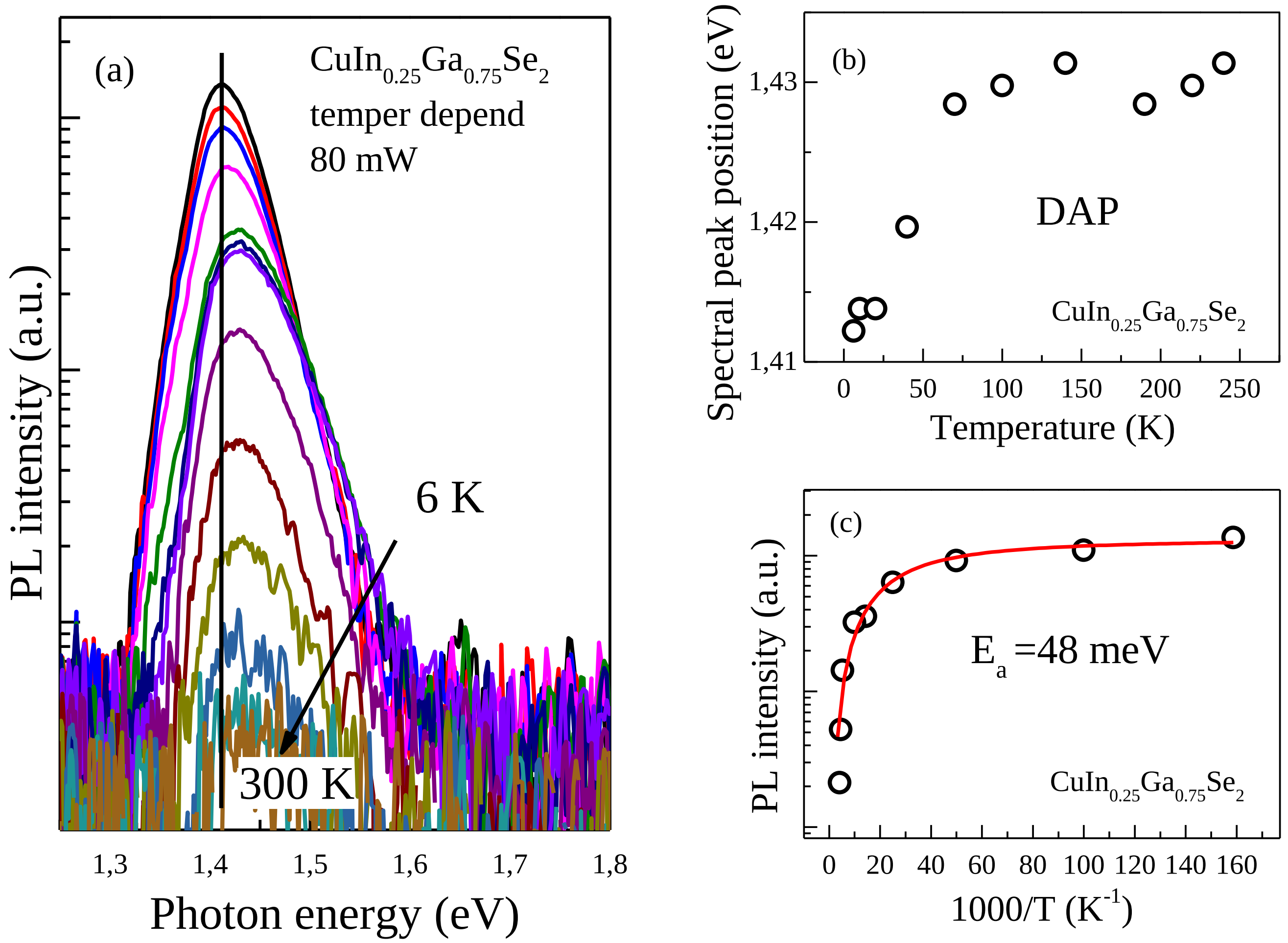

Figure 5.18: (a) Temperature dependence, (b) peak energy vs. temperature plot and (c) log(peak PL intensity) vs.1000/temperature plot from $CuIn_{0.25}Ga_{0.75}Se_2$.

5.1.8 $CuGaSe_2$ (x=1.00)

At 6 K just one peak at 1.59 eV can be observed in the excitation intensity dependence of the PL spectrum of $CuGaSe_2$ (Figure 5.19a). Similar to the $CuIn_{0.25}Ga_{0.75}Se_2$ sample, the shape of the PL peaks of this 100% sample is rather symmetrical, but it still has its high energy side steeper than the low energy one. The k-value of 0.90 is less than 1 as shown in Figure 5.19b, therefore we can conclude that the recombination is defect related. With increasing excitation intensity the peak position shifts to higher energies with a j-shift of 12.7 meV/decade (Figure 5.19c), suggesting a band tail related recombination (according to section 3.3).

In the temperature dependence (Figure 5.20a) it is clearly seen that firstly the peak position shifts to lower energy, reaches a minimum energy of 1.562 eV at 70 K and then moves to higher energies again (Figure 5.20b). According to this pattern it can be either a BT or BI recombination. To clarify which it is the value of γ and E_a should be compared. Here, according to Figures 5.20c and 5.20d, E_a=26 meV and γ=17 meV. Although the value of the activation energy is a little more than the γ-value, the characteristic value of j-shift indicates that it is likely to be a BT transition rather than BI.

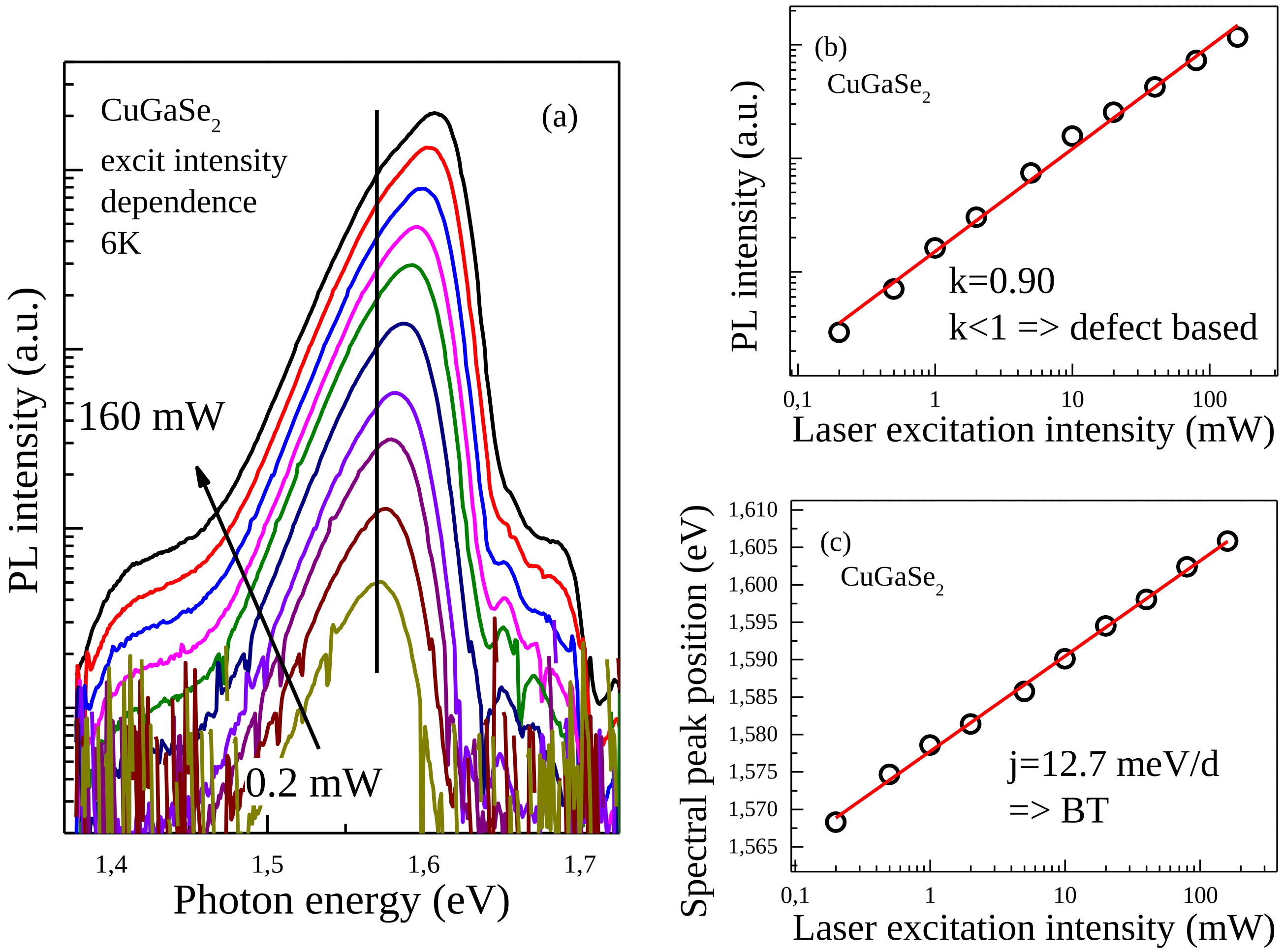

Figure 5.19: (a) Excitation intensity dependence, (b) k-value plot and (c) j-shift plot from CuGaSe$_2$.

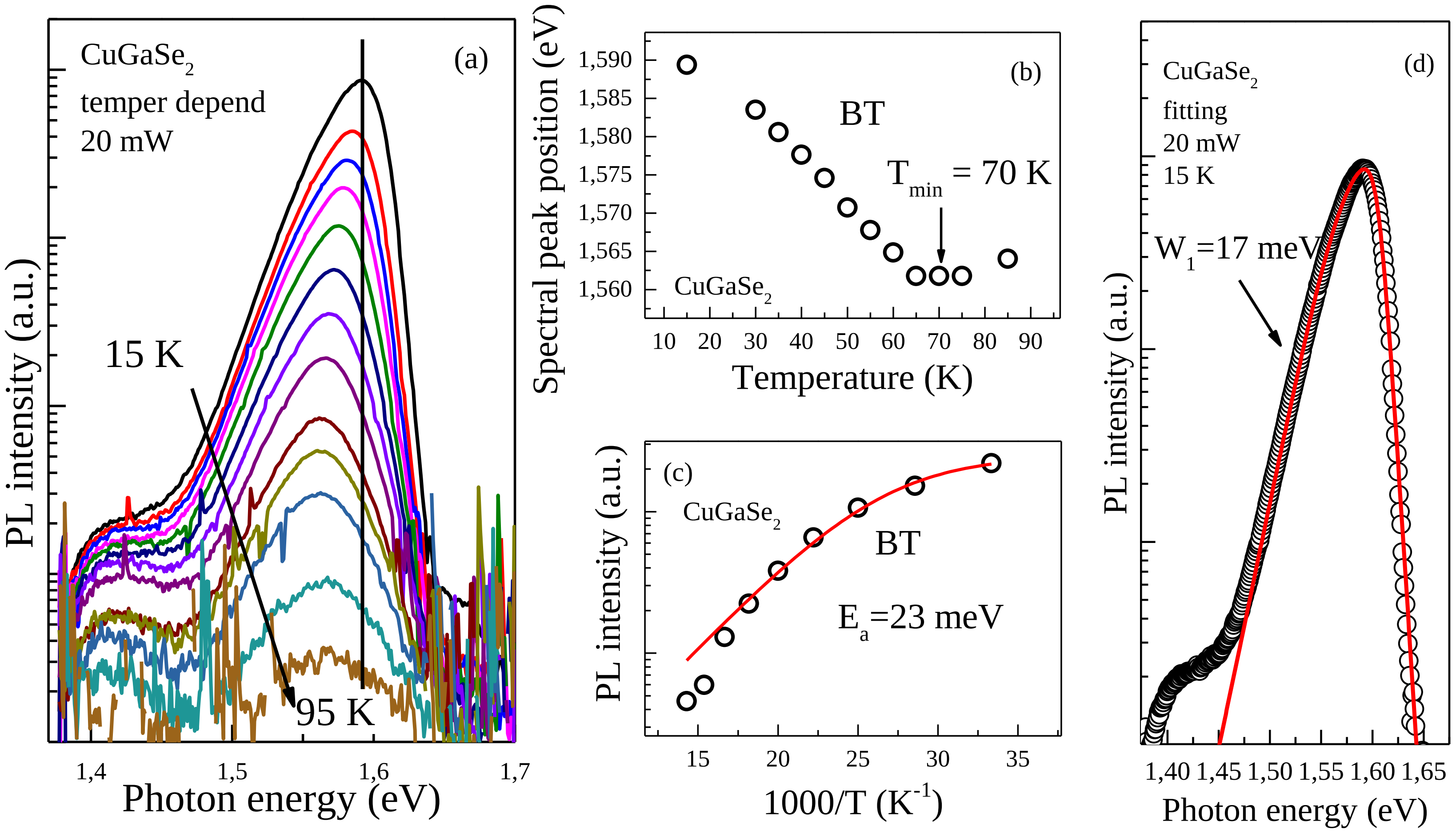

Figure 5.20: (a) Temperature dependence, (b) peak energy vs. temperature plot, (c) log(peak PL intensity) vs. 1000/temperature plot and (d) fitting of PL spectrum at 15 K and 20 mW by double sigmoid function from CuGaSe$_2$.

Tables 5.1 and 5.2 summarise the PL results from the CIGSe samples. The values of E_{max} are given for dominant peaks at 20 mW and at minimum temperature ~6 K. T_q is the temperature, at which the band quenched.

Table 5.1: PL results on $CuIn_{1-x}Ga_xSe_2$ samples.

Parameters	**x**						
	0.00	**0.05**	**0.10**	**0.25**	**0.50**	**0.75**	**1.00**
E_{max} (eV)	0.95	1.00	1.06	1.13	(2): 1.28	1.41	1.59
j-shift (meV/d)	2.6±0.2	11.0±0.5	5.3±0.2	3.24±0.14	(1): 7.3±0.3 (2): 10.63±0.14	5.34±0.25	12.7±0.2
k-value	0.949±0.015	0.94±0.02	0.93±0.02	0.94±0.02	(1): 0.88±0.03 (2): 0.87±0.04	0.81±0.02	0.90±0.03
$\gamma=W_1$ (meV)	14	-	-	17	20	-	17
T_{min} (K)	62.5	55	60	30	(1): 50 (2): 50	-	70
E_{a1} (meV)	44±1	31±2	23±1	13±1	(1): 15.5±0.4 (2): 13±2	48±3	23±2
E_{a2} (meV)	15.5±0.3	-	-	-	-	-	-
Fitting model	Ar-2	Kr-1	Kr-1	Kr-1	Kr-1	Kr-1	Ar-1
Type of recombination	BI+BT+BB	BI	BT	BT+BB	(1): BI+BB (2): BT+BB	DAP	BT

Table 5.2: PL results on excitons in $CuIn_{1-x}Ga_xSe_2$ samples.

Parameters	**x**			
	0.05		**0.10**	
E_{max} (eV)	1.07	1.08	1.095	1.101
j-shift (meV/d)	-	-	-	-
k-value	1.20±0.03	4.6±0.1	1.45±0.04	1.6±0.1
T_q (K)	30	55	30	60
E_a (meV)	-	-	-	19±2
Fitting model	-	-	-	Ar-1
Type of exciton	BE	FE	BE	FE

The free and bound excitons identified in the CIGSe samples with 5% and 10% Ga content indicate a very high purity of the material. Excitonic emission in CIGSe was reported elsewhere [37], but without clear evidence.

The presence of the BI peaks in the $CuInSe_2$ and $CuIn_{0.5}Ga_{0.5}Se_2$ samples can be justified by low Ga content and, therefore, low defect concentration. In our case the BI peaks are caused by a recombination of free electrons with holes localised on the deep acceptor.

It is hard to explain why a DAP was found only in the sample with 75% of Ga. Presumably, it is due to the populations of defects. This might be caused by the non-homogeneity of the copper composition along the ingot, because the top of each ingot is copper rich and bottom of the ingot is copper deficient. Since the ingot is cut across into several slices, this results in different copper content and, therefore, different types of recombination in different samples (slices). Each slice has a number. To achieve the close results it is important to use the slices with the same or next number. Therefore, band tails not found in the 75% sample can be simply explained by wrong slice selection. Definitely, more work is needed to understand this.

With higher content of Ga the concentration of defects raises and the material becomes more doped, thus the formation of band tails are more probable, as in the samples with 10%, 25%, 50% and 100% Ga content.

On the other hand, it is not entirely clear what defects determine the band tails. There is an opinion that it is antisite defects formed after vacancies and interstitials. For $CuInSe_2$ they are, first of all, V_{Cu} (acceptors), Cu_i and In_{Cu} (donors), respectively. In CIGSe the replacement of In by Ga occurs through the disordering of In-Ga in the cation sublattice. It should grow with an increase in the proportion of Ga to ~50% and then fall. Theorists consider that Ga_{Cu} in $CuGaSe_2$ is more detrimental than In_{Cu} in $CuInSe_2$, because its level is much deeper. Thus, Ga_{Cu}^{+} and Ga_{Cu}^{2+} with energies of 490 and 690 meV, respectively, are against In_{Cu}^{+} with energy of 240 meV and In_{Cu}^{2+} with energy of 330 meV, while the energy of V_{Cu}^{-} in $CuInSe_2$ is 30 meV and that for V_{Cu}^{+} in $CuGaSe_2$ is 10 meV [38].

We observed an increase in the average band tail depth γ from 14 meV in $CuInSe_2$ to 20 meV in $CuIn_{0.5}Ga_{0.5}Se_2$ through 17 meV in $CuIn_{0.75}Ga_{0.25}Se_2$ and then a decrease in $CuGaSe_2$, although, not to the level of $CuInSe_2$, but to only 17 meV. This suppose that in $CuGaSe_2$ the band tails are deeper than in $CuInSe_2$ and can explain why with an increase in Ga content above 30%, the efficiency of the solar cells does not improve. However, this is only an assumption and we do not have enough statistics for such a statement.

5.1.9 $Cu_2ZnSnSe_4$ before Ar^+ radiation damage

At 7 K and 20 mW the PL spectrum of $Cu_2ZnSnSe_4$ presents a broad asymmetric peak centered at 0.946 eV with steeper slope on the high energy side compared to the low energy side (Figure 5.21a). Features associated with water vapour absorption are seen in the region near 0.9 eV, as present in many PL spectra of $Cu_2ZnSnSe_4$. The k-value of $Cu_2ZnSnSe_4$ before Ar^+ radiation damage is 0.99 (Figure 5.21b). As seen in Figure 5.21c, increasing the excitation intensity from 0.5 mW to 50 mW causes the spectral peak position to blueshift with a j-value of 11.7 meV/d.

From the temperature-dependent measurement (Figure 5.22a and Figure 5.22b) it is clearly seen that at lowest temperature (15 K) one asymmetric peak located at 0.94 eV is present in the PL spectrum. By ~70 K the shape of the peak becomes more symmetrical. The 0.94 eV peak quenched by around 150 K, while a second peak at 1.02 eV appears at ~110 K. After reaching the temperature of 150 K this new peak was the only peak in the PL spectra.

The value of the activation energy obtained from Arrhenius analysis (Figure 5.22c) for the first peak was 75 meV, whereas the γ-value for $Cu_2ZnSnSe_4$ before Ar^+ radiation damage obtained from temperature dependence of fitting parameters W_1 and W_2 was 25 meV (Figure 5.22d). Here the E_a is 3 times greater than γ, indicating that the first peak was due to BI recombination. In the case of the second peak a BB recombination was involved since the peak dominated at room temperatures.

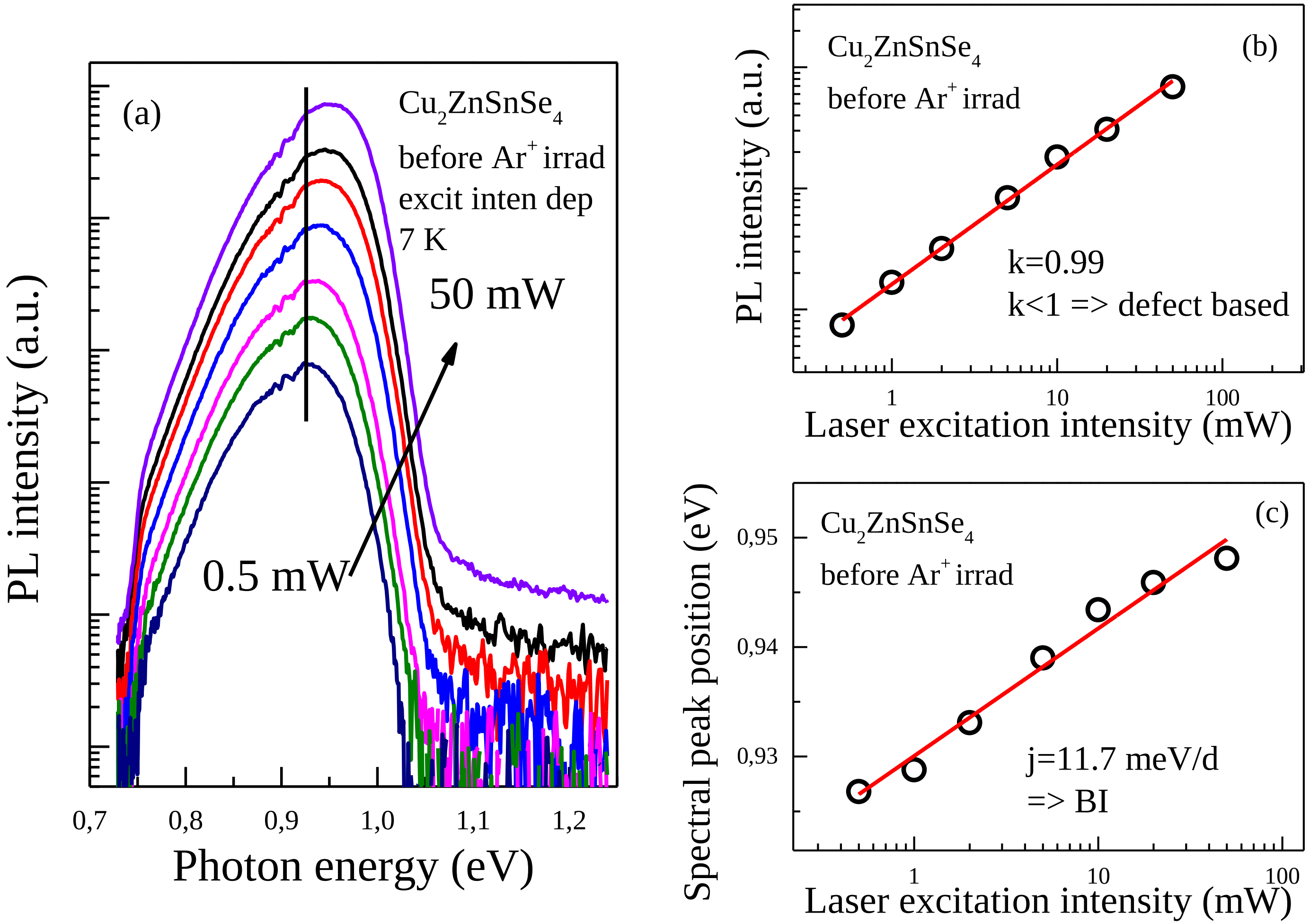

Figure 5.21: (a) Excitation intensity dependence, (b) k-value plot and (c) j-shift plot from Cu$_2$ZnSnSe$_4$ before Ar$^+$ irradiation.

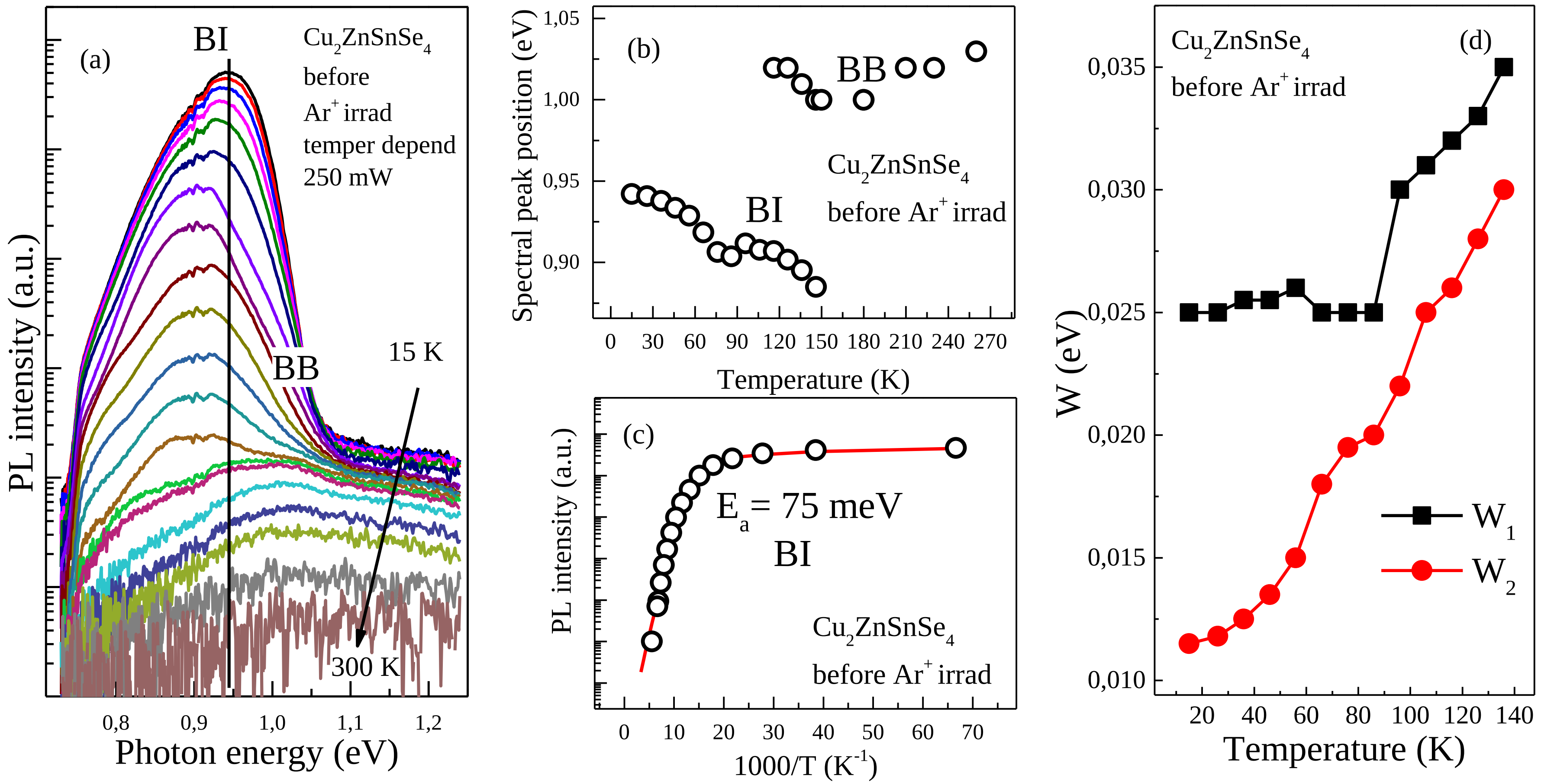

Figure 5.22: (a) Temperature dependence, (b) peak energy vs. temperature plot, (c) log(peak PL intensity) vs. 1000/temperature plot and (d) temperature dependence of fitting parameters W_1 and W_2 from $Cu_2ZnSnSe_4$ before Ar^+ irradiation.

5.1.10 $Cu_2ZnSnSe_4$ after Ar^+ radiation damage

The PL spectra after Ar^+ irradiation measured at 6 K and 20 mW are shown in Figure 5.23a and reveal the same broad asymmetrical band at 0.946 eV as in the PL spectra before irradiation. However, the Ar^+ radiation damage reduced the band intensity by a factor of 4.5, made the low energy slope gentler and induced a tail, which extends beyond the limit of the detector (Figure 5.23b).

With increasing excitation intensity (Figure 5.24a) the spectral peak position of the band in PL spectra of $Cu_2ZnSnSe_4$ after Ar^+ radiation damage moved towards high energies like the PL band in $Cu_2ZnSnSe_4$ before Ar^+ radiation damage, keeping the value of the k-coefficient almost the same (Fig. 5.24b) and the values of the j-shift rather close (Fig. 5.24c): they changed from 0.99 to 0.98 and from 11.7 meV/d to 12.4 meV/d, respectively. As described in section 3.3, not greatly changing j-shift means that the bombardment did not change the ratio of concentrations of donors and acceptors a lot, generating both donors and acceptors.

According to the temperature-dependent measurements (Figure 5.25a) irradiation increased the average depth of potential fluctuations (γ) from 25 meV before irradiation to 30 meV after irradiation (Figure 5.25b). The Arrhenius analysis (Figure 5.25d) showed that the activation energy rose from 75 meV before irradiation to 88 meV after irradiation. Therefore, here again a BI recombination is the main source of PL.

Ar ions displace atoms in the CZTSe lattice, creating primary radiation defects, vacancies and interstitials, which recombine at room temperature during irradiation and shortly after that. In multinary compounds such a recombination tends to form antisite defects that are associated with the band tails [39]. According to the WDX results (see subsection 5.2.2), the most likely defects are acceptors V_{Cu} and donors Zn_{Cu} with energies of 40 and 80 meV, respectively.

The proof of secondary defects formation is the observed increase of γ and the activation energy as well as the appearance of the long low energy tail. The raised concentration of non-radiative traps causes the reduced PL band intensity after the irradiation that is also consistent with an increased concentration of antisite defects.

Ar ions damage a near surface layer of 10 nm whereas PL emission comes from top layer of 100 nm, assuming the absorption coefficient of 3.5×10^4 cm^{-1} at 2.5 eV (496 nm) [40]. This means that the PL spectra are a combination of emission from damaged and undamaged CZTSe, explaining how even after the dose of 2×10^{16} cm^{-2} we still observe an intense emission.

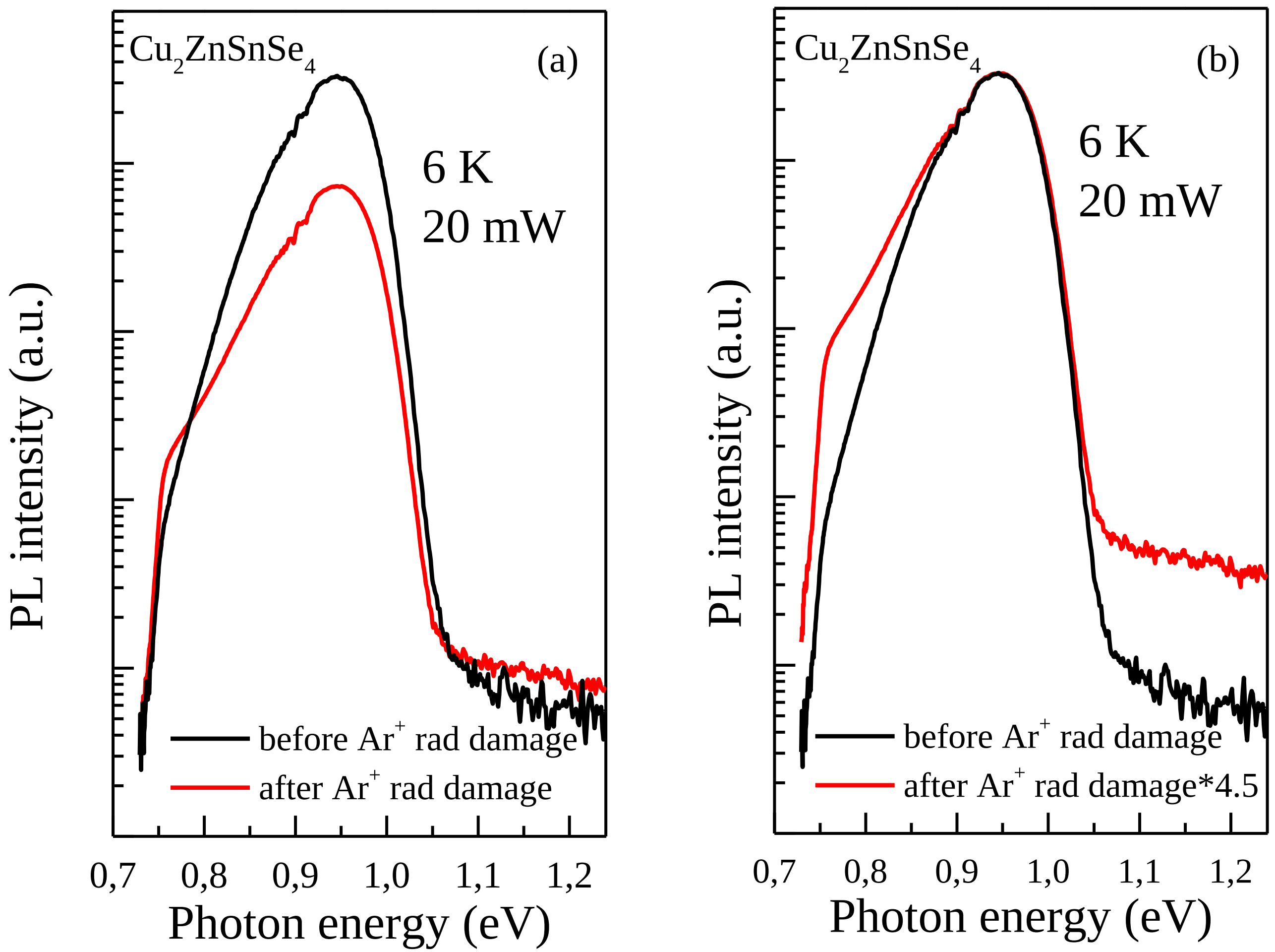

Figure 5.23: The comparison of PL spectra from $Cu_2ZnSnSe_4$ before and after Ar^+ irradiation, where (a) and (b) show PL spectra with real and normalised intensity, respectively.

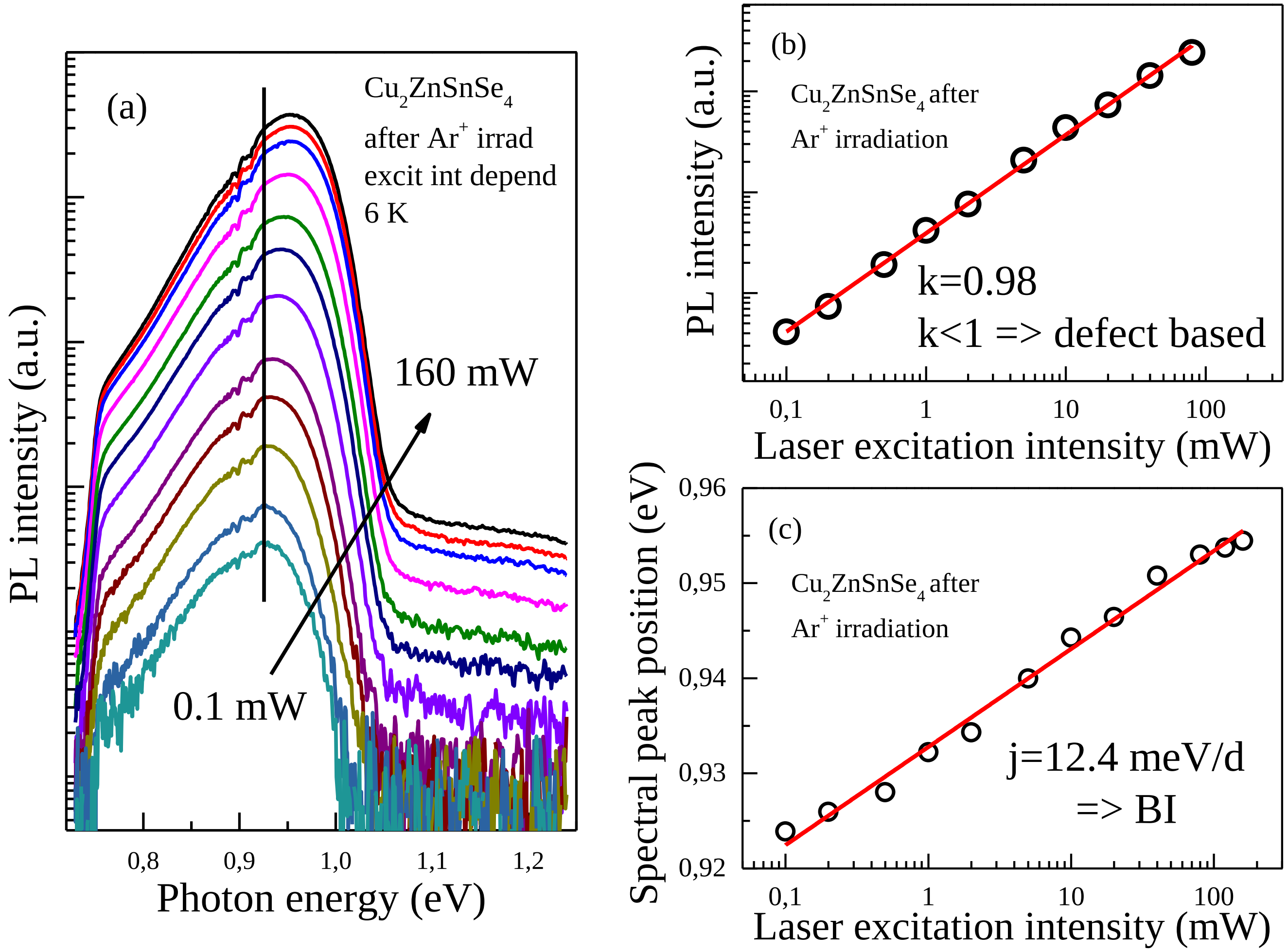

Figure 5.24: (a) Excitation intensity dependence, (b) k-value plot and (c) j-shift plot from Cu$_2$ZnSnSe$_4$ after Ar$^+$ irradiation.

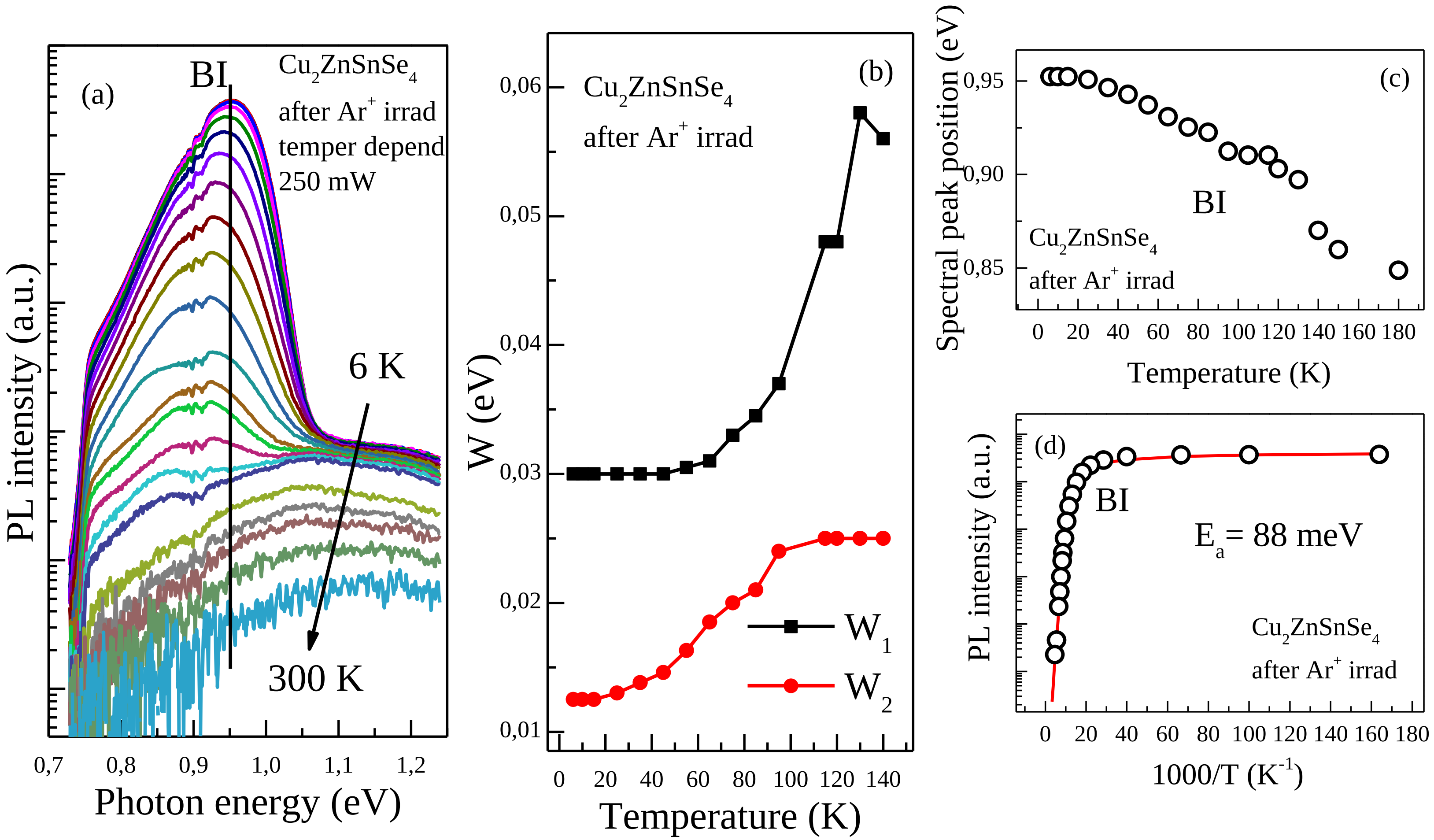

Figure 5.25: (a) Temperature dependence, (b) temperature dependence of fitting parameters W_1 and W_2, (c) peak energy vs. temperature plot and (d) log(peak PL intensity) vs. 1000/temperature plot from $Cu_2ZnSnSe_4$ after Ar^+ irradiation.

All PL results on $Cu_2ZnSnSe_4$ samples are summarised in the Table 5.3.

Table 5.3 – Parameters of the PL spectra of CZTSe before and after Ar^+ irradiation.

Parameters	CZTSe before Ar^+	CZTSe after Ar^+
E_{max} (eV)	0.946	0.946
k-value	0.99±0.02	0.977±0.014
j-shift (meV/d)	11.7±0.8	12.4±0.3
$\gamma=W_1$ (meV)	25	30
E_a (meV)	75	88
Fitting model	Kr-1	Kr-1
Type of recombination	BI+BB	BI

5.2 Microscopy results

5.2.1 EDX results

As justified in section 4.2, the EDX system was used to establish the elemental composition of the $CuIn_{1-x}Ga_xSe_2$ samples with x=0.05, 0.10, 0.25, 0.50 and 0.75. These measurements were calibrated by using the EDX analysis of the samples of pure $CuInSe_2$ and $CuGaSe_2$. The accelerating voltage in each experiment was 30 kV. For Cu, Ga and Se the K-series was selected, for In the L-series was selected [41]. As an example the EDX spectrum of $CuIn_{0.75}Ga_{0.25}Se_2$ is shown on Figure 5.26.

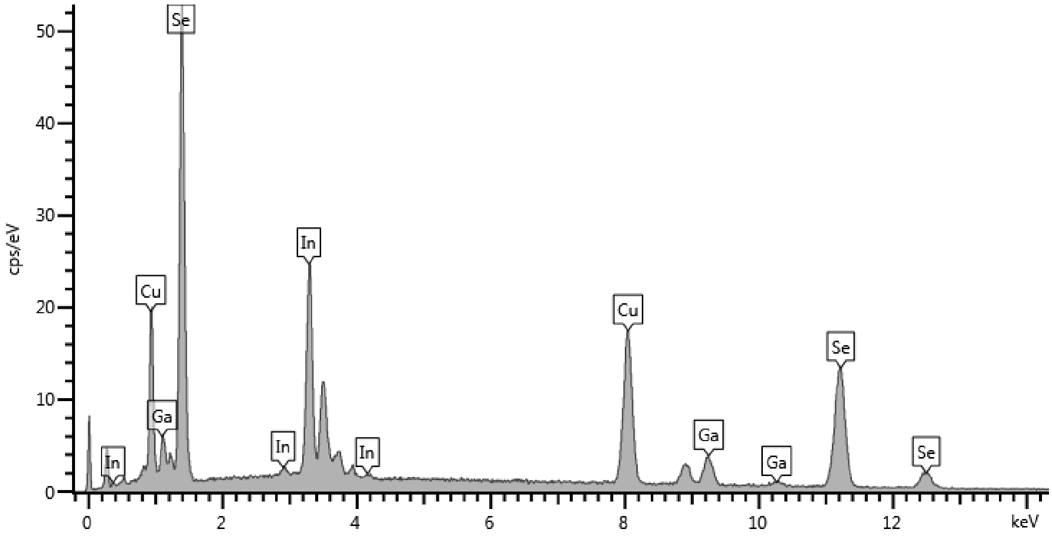

Figure 5.26: EDX spectrum of $CuIn_{0.75}Ga_{0.25}Se_2$. The elements giving rise to each particular peak are indicated.

The quality of the result was assessed by how close the total weight percentage (Wt.%) is to 100. According to that fact the $CuInSe_2$ and $CuGaSe_2$ samples were chosen as a standard of Cu, In, Ga and Se since these user standards should give better results rather than factory standards. For the samples with 5%, 10% and 25% Ga content the standards for Cu, In and Se were taken from $CuInSe_2$ whereas the standard for Ga was taken from $CuGaSe_2$. For the sample with 75% content of Ga, vice versa, Cu, Ga and Se standards were derived from $CuGaSe_2$ and standard for In was derived from $CuInSe_2$. For the sample with 50% Ga content both variants were applied.

For these measurements totals of 71–102% were achieved, indicating that some of the results are reliable and some of the results are not entirely trustworthy. For all the chalcopyrite samples except the samples with 5% and 10% Ga content the value of Wt.% was very close to 100. In the case of the $CuIn_{0.95}Ga_{0.05}Se_2$ and $CuIn_{0.90}Ga_{0.10}Se_2$ samples a few measurements were conducted amongst which the best result achieved was 71 Wt.% and 85 Wt.%, respectively, suggesting that these two obtained elemental compositions are not quite reliable.

Tables 5.4 and 5.5 contain results of composition analysis (atomic percentage for each element and corresponding chemical formula, respectively) for all seven chalcopyrite samples.

Table 5.4 – Atomic percentages of elements in the chalcopyrite samples.

Element	**At.% at different x**							
	0.00	**0.05**	**0.10**	**0.25**	**0.50 (CISe std, Ga from CGSe)**	**0.50 (CGSe std, In from CISe)**	**0.75**	**1.00**
Cu	25.00	23.66	24.92	25.46	25.37	24.64	24.54	24.97
In	25.00	19.05	19.74	20.47	11.95	12.23	5.68	0.20
Ga	-	1.48	2.74	5.98	13.17	13.45	18.89	24.95
Se	50.00	55.8	52.61	48.08	49.51	49.67	50.89	49.88
[Cu]/ [In+Ga]	1.00	1.15	1.11	0.96	1.01	0.96	1.00	0.99
[Se]/ [Cu+In+Ga]	1.00	1.26	1.11	0.93	0.98	0.99	1.04	1.00
[Ga]/ [Ga+In]	0.00	0.07	0.12	0.23	0.52	0.52	0.77	0.99

Table 5.5 – Empirical formulae of chalcopyrite samples derived from EDX analysis.

x	Stoichiometric formula	Empirical formula
0.00	$CuInSe_2$	$Cu_1In_1Se_2$
0.05	$CuIn_{0.95}Ga_{0.05}Se_2$	$Cu_{0.95}In_{0.76}Ga_{0.06}Se_{2.23}$
0.10	$CuIn_{0.90}Ga_{0.10}Se_2$	$Cu_1In_{0.79}Ga_{0.11}Se_{2.10}$
0.25	$CuIn_{0.75}Ga_{0.25}Se_2$	$Cu_{1.02}In_{0.82}Ga_{0.24}Se_{1.92}$
0.50	$CuIn_{0.50}Ga_{0.50}Se_2$	$Cu_{1.01}In_{0.48}Ga_{0.53}Se_{1.98}$ ($CuInSe_2$ std, Ga from $CuGaSe_2$) $Cu_{0.99}In_{0.49}Ga_{0.54}Se_{1.99}$ ($CuGaSe_2$ std, In from $CuInSe_2$)
0.75	$CuIn_{0.25}Ga_{0.75}Se_2$	$Cu_{0.98}In_{0.23}Ga_{0.76}Se_{2.04}$
1.00	$CuGaSe_2$	$Cu_1In_{0.01}Ga_1Se_2$

For the samples of $CuIn_{0.95}Ga_{0.05}Se_2$ and $CuIn_{0.90}Ga_{0.10}Se_2$ considerable excess of Cu and Se (anions) is observed. This is likely to be the explanation of why excitons are detected in these samples [42]. As soon as [Cu]/[In] becomes less than 1, the intensity of excitonic peaks decreases and band tails appear. For the rest of the samples the [Cu]/[In+Ga] ratio did not exceed 1, confirming the tail-related nature of recombination in the corresponding samples [43].

The compositions shown above are reasonably close to the stoichiometric values (except e.g. the sample with 25% Ga, where the S deficiency is observed). The deviations could be explained by the character of the surface of the samples. As was mentioned earlier it was difficult to collect good spectra from samples with 5% and 10% Ga content because of the high roughness of the samples surface. Additionally, the deviations could be connected with the fact that all the samples were embedded into In substrates, that also probably explains the presence of small amount of In in the $CuGaSe_2$ sample.

5.2.2 WDX results

As justified in section 4.2, the WDX analysis was performed before Ar^+ radiation damage of the $Cu_2ZnSnSe_4$ sample to establish its composition. In this case the factory standards of Cu, Zn, Sn and Se were used. The operation voltage of electron beam was 10 kV. The elemental compositions of the film determined by WDX analysis as the average of 10-point linear scans are shown in Table 5.6. For these measurements Wt.% totals of 96–99% were achieved, indicating that the obtained results are rather reliable.

Table 5.6 – Atomic percentages of elements in the sample of $Cu_2ZnSnSe_4$.

Element	**At.%**
Cu	21.8
Zn	15.2
Sn	12.9
Se	50.1
[Cu]/[Zn+Sn]	0.78±0.10
[Zn]/[Sn]	1.18±0.02
[Se]/[Cu+Zn+Sn]	1.00±0.01

This corresponds to a chemical formula $Cu_{1.74}Zn_{1.22}Sn_{1.03}Se_{4.01}$.

The deviation from stoichiometric quantities could be explained by the sample not having a uniform composition across it surface. The [Cu]/[Zn+Sn] ratio is less than 1 (Cu deficiency), that explains why tail-related features were observed in the PL spectra of $Cu_2ZnSnSe_4$ [20]. On the other hand, ones of the most efficient solar cells are made from CZTSe with copper deficiency and zinc excess, because in this case the open circuit voltage is the greatest [39].

Chapter 6

Conclusion

This work describes a study of some leading candidates for the absorber layers of thin film solar cells: $CuIn_{1-x}Ga_xSe_2$ (CIGSe) and $Cu_2ZnSnSe_4$ (CZTSe).

CIGSe-based solar cells lead in terms of conversion efficiencies, radiation hardness and overall stability amongst thin film PV devices. This study, employing PL spectroscopy and examining $CuIn_{1-x}Ga_xSe_2$ single crystals with x=0, 0.05, 0.10, 0.25, 0.50, 0.75 and 1.00, tries to clarify why solar cells with $x > 0.3$ in their CIGSe absorber do not improve the performance although the optimum E_g= 1.4 eV for a single junction PV device should be at about x = 0.5.

CZTSe is further development of CIGSe, where rare and expensive In and Ga are substituted with Zn and Sn, making this new material one of the most promising for absorber in sustainable thin film solar cells. It demonstrates a spectacular similarity of some of its structural and electronic properties with those in CIGSe. In this study we examine the radiation properties of this material by comparing PL spectra of CZTSe thin films before and after Ar^+ irradiation.

The PL spectra of the $CuIn_{1-x}Ga_xSe_2$ samples with x = 0.10, 0.25, 0.5 and 1.00 demonstrate the presence of band tails generated by randomly distributed potential fluctuations due to high concentrations of charged defects. The nature of the observed PL bands was established by analysing the temperature and excitation intensity dependences of the PL spectra, the shape of the obtained emission bands as well as their spectral position and intensity. From the low temperature PL spectra the average band tail depth γ, describing the density of states (DOS) of the valence band, is calculated.

The sample with x = 0.75 appeared to have a near stoichiometric [Cu]/[In+Ga] and did not show any band tail features in its PL spectra. Instead the observed band reveals a donor-acceptor pair (DAP) recombination mechanism.

In $CuInSe_2$ despite a near stoichiometric elemental composition low temperature PL spectra of the samples reveal a dominant band assigned to the band-impurity (BI) recombination mechanism, a recombination of free electrons from the conduction band and holes localised at an acceptor with its level at 44 meV from the valence band. This level is spread by the valence band tail with the average depth of $\gamma = 14$ meV.

A rise of the Ga content to x = 0.25 (0.23 according to the EDX) increases γ to 17 meV. This increase of γ well correlates with the change of [Cu]/[In+Ga] from a near stoichiometric to a copper deficient. Such an increase in γ can also partly be attributed to a Se deficiency. The rise of the Ga content also changes the type of recombination from BI to band-tail (BT) one. The increase of γ might also reflect a reduction in the structural quality of the lattice due to a randomisation of In-Ga on the cation sublattice.

The next rise of Ga content to x = 0.5 (0.52 according to EDX) increases γ further to the maximum value of 20 meV leaving the same BT recombination mechanism. In this sample the Se content returns to a stoichiometric value. Therefore we should assign the increase in γ to the substitution of In in defects, which are likely to be formed at copper deficiency (such as In_{Cu} and their neutral complexes In_{Cu}+ $2V_{Cu}$), by Ga forming the donors Ga_{Cu}, which are much deeper than donors In_{Cu} and their neutral complexes Ga_{Cu}+ $2V_{Cu}$. Also the increase of γ should be affected by the further reduction of the lattice structural quality due the further randomisation of In-Ga.

In $CuGaSe_2$ the mean depth of the valence band tail of 17 meV becomes smaller. This reduction can be associated with an almost stoichiometric [Cu]/[In+Ga] and [Se]/[Cu+In+Ga] and with general improvements of the lattice structure when the material becomes a ternary compound. However the reduced γ is still greater than $\gamma = 14$ meV in $CuInSe_2$ demonstrating that Ga based defects results in deeper band tails.

The increasing content of Ga from x = 0 to x = 1 is followed by j-shift increasing from 2.6 meV per decade of laser excitation power to 12.7 meV per decade. This can be interpreted as a gradual increase in the compensation level of the material.

With increasing excitation power in the PL spectra of CIGSe with x changing from 0 to 1 the gradient k of the PL intensity rise demonstrates values close to 0.9 on a log-log scale, supporting the assignment of the dominant bands to defects related emission.

For the first time free and bound excitons in CIGSe samples with 5% and 10% Ga content were clearly observed, identified and analysed, indicating a high purity of the material. In the case of free exciton in $CuIn_{0.90}Ga_{0.10}Se_2$ the calculated binding energy of 19 meV is consistent with values of 12 and 18 meV reported in literature. This observation of excitonic emission well correlates with the copper excess elemental composition.

Concerning kesterite samples, for the first time ever a study of the impact of 4 keV Ar^+ radiation damage (surface cleaning for XPS) was conducted for $Cu_2ZnSnSe_4$. The BI transition was identified as a main source of PL in CZTSe samples before and after irradiation, while the spectral peak position at 0.946 eV remained the same. However, comparison of the PL spectra of $Cu_2ZnSnSe_4$ samples before and after radiation treatment collected at 6 K and 20 mW revealed significant changes in the material. The band intensity was reduced by 5 times and the peak shape changed to that one with gentler low energy slope contained long induced tail. The tail is associated with complexes of antisite secondary defects formed after the primary defects, interstitial atoms and vacancies, generated by Ar ions, and recombined during and shortly after the irradiation. The formation of additional defects is supported by an increase in γ from 25 to 30 meV as well as increase in the E_a from 75 to 88 meV, suggesting a change of the dominant acceptor in the material.

Acknowledgements

I would like to thank Dr Michael Yakushev for insightful explanation of the theory of photoluminescence, production of samples and help with the PL system, Prof Robert Martin for his relevant comments and useful pieces of advice and Prof Maxim Fedorov for financial support on this project. I would also like to thank Michael Sulimov for help with CZTSe results processing and Dr Paul Edwards and Lucia Spasevski for assistance with the electron microanalysis measurements on the samples.

References

[1] Sharma, S., Jain, K.K., Sharma, A. Solar Cells: In Research and Applications–A Review. *Materials Sciences and Applications* **6**, 1145–1155 (2015).

[2] REN21. Renewables 2016 Global Status Report. *REN21 Secretariat, Paris*, 271 (2016).

[3] Pogharian, S., Ayoub, J., Candanedo, J.A., Athienitis, A.K.. Getting to a net zero energy lifestyle in Canada: the Alstonvale net zero energy house. *3rd European PV Solar Energy Conference* (2008).

[4] Neamen, D.A. Semiconductor Physics and Devices - 3rd ed. *McGraw-Hill, New York*, 746 (2003).

[5] Shockley, W., Queisser, H.J. Detailed Balance Limit of Efficiency of p-n Junction Solar Cells. *Journal of Applied Physics* **32**, 510–519 (1961).

[6] Lee Y.S., Gershon T., Gunawan O., Todorov T.K., Gokmen T., Virgus Y., Guha, S. $Cu_2ZnSnSe_4$ Thin-Film Solar Cells by Thermal Co-evaporation with 11.6% Efficiency and Improved Minority Carrier Diffusion Length. *Advanced Energy Materials* **12**, 1401372–1401374 (2015).

[7] Jackson P., Wuerz R., Hariskos D., Lotter E., Witte W., Powalla M. Effects of heavy alkali elements in $Cu(In,Ga)Se_2$ solar cells with efficiencies up to 22.6%. *Physica Status Solidi - Rapid Research Letters* **10**, 583–586 (2016).

[8] Green, M.A. Solar Cells: Operating Principles, Technology and System Applications. *Prentice-Hall, New Jersey,* 274 (1982).

[9] Repins, I., Vora N., Beall C., Wei S.H., Yan Y., Romero M., Teeter G., Du H., To B., Young M., Noufi R. Kesterites and Chalcopyrites: A Comparison of Close Cousins. *Materials Research Society Proceedings* **1324,** mrss11-1324-d17-01 (2011).

[10] Hurtavy, V.G. Sheleg, A.U. Effect of ionizing radiation on dielectric characteristics of $Cu_2ZnSn(S_xSe_{1-x})_4$ single crystals. *Physics of the Solid State* **59**, 242–245 (2017).

[11] https://www.nrel.gov/pv/

[12] Tomlinson R.D. Fabrication of $CuInSe_2$ single crystals using melt-growth technique. *Solar Cells* **16**, 17–26 (1986).

[13] Márquez-Prieto J., Ren Y., Miles R.W., Pearsall N., Forbes I. The influence of precursor Cu content and two-stage processing conditions on the microstructure of $Cu_2ZnSnSe_4$. *Thin Solid Films* **582**, 220–223 (2015).

[14] Champness, C.H. $CuInSe_2$: Solar cell material, not fool's gold. *Physics in Canada*, 29-36 (2001).

[15] Reshak, A.H., Nouneh K., Kityk I.V., Bila J., Auluck S., Kamarudin H., Sekkat Z. Structural, Electronic and Optical Properties in Earth-Abundant Photovoltaic Absorber of Cu_2ZnSnS_4 and $Cu_2ZnSnSe_4$ from DFT calculations. *International Journal of Electrochemical Science* **9,** 955–974 (2014).

[16] Choi, S. G., Kim, T.J., Hwang, S.Y., Li, J., Persson, C., Kim, Y.D., Wei, S.H., Repins, I.L. Temperature dependent band-gap energy for $Cu_2ZnSnSe_4$: A spectroscopic ellipsometric study. *Solar Energy Materials and Solar Cells* **130,** 375–379 (2014).

[17] Persson, C. Electronic and optical properties of Cu_2ZnSnS_4 and $Cu_2ZnSnSe_4$. *Journal of Applied Physics* **107**, 053710-1–053710-8 (2010).

[18] Yakushev, M. V., Luckert, F., Faugeras, C., Karotki, A. V., Mudryi, A. V., Martin, R. W. Excited states of the free excitons in $CuInSe_2$ single crystals. *Applied Physics Letters* **97,** 152110-1–152110-3 (2010).

[19] Luckert, F., Yakushev, M.V., Faugeras, C., Karotki, A.V., Mudryi, A.V., Martin, R.W. Diamagnetic shift of the A free exciton in $CuGaSe_2$ single crystals. *Applied Physics Letters* **97,** 162101-1–162101-3 (2010).

[20] Márquez-Prieto, J., Yakushev, M.V., Forbes, I., Krustok, J., Edwards, P.R., Zhivulko, V.D., Borodavchenko, O.M., Mudryi, A.V., Dimitrievska, M., Izquierdo-Roca, V., Pearsall, N., Martin, R.W. Impact of the selenisation temperature on the structural and optical properties of CZTSe absorbers. *Solar Energy Materials and Solar Cells* **152,** 42–50 (2016).

[21] Levanyuk A.P., Osipov V.V. Edge luminescence of the direct-gap semiconductors. *Uspekhi Fizicheskikh Nauk* **24**, 187–215 (1981).

[22] Krustok, J., Collan, H., Yakushev, M., Hjelt, K. The Role of Spatial Potential Fluctuations in the Shape of the PL Bands of Multinary Semiconductor Compounds. *Physica Scripta* **79**, 179–182 (1999).

[23] Bebb H.B., Williams E. Semiconductors and Semimetals. *Academic Press, New York,* 181 (1972).

[24] Pankove J.I. Optical processes in semiconductors. *Prentice-Hall, New Jersey,* 422 (1971).

[25] Klingshirn C.F. Semiconductor Optics. *Springer, Berlin,* 797 (1997).

[26] Yu P.W. Radiative recombination in melt-grown and Cd-implanted $CuInSe_2$. *Journal of Applied Physics* **47**, 677–684 (1976).

[27] Levanyuk, A.P., Osipov, V.V. The theory of luminescence of heavily-doped semiconductors *Soviet Physics of Semiconductors* **7**, 1058–1068 (1973).

[28] Yakushev, M.V., Mudryi, A.V., Borodavchenko, O.M., Volkov, V.A., Martin, R.W. A photoluminescence study of excitonic grade $CuInSe_2$ single crystals irradiated with 6 MeV electrons. *Journal of Applied Physics* **118,** 155703-1–155703-7 (2015).

[29] Schmidt T., Lischka K., Zulehner W. Excitation-power dependence of the near-band-edge photoluminescence of semiconductors. *Physical Review B* **45**, 8989-8994 (1992).

[30] Krustok J., Collan H., Hjelt K. Does the low-temperature Arrhenius plot of the photoluminescence intensity in CdTe point towards an erroneous activation energy? *Journal of Applied Physics* **81**, 1442–1445 (1997).

[31] https://www.fei.com

[32] http://www.cameca.com

[33] Shirakata S., Nakada T. Near-band-edge photoluminescence in $Cu(In,Ga)Se_2$ solar cells. *Solar Energy Materials and Solar Cells* **95**, 219–222 (2011).

[34] Luckert, F., Yakushev, M.V., Faugeras, C., Karotki, A.V., Mudryi, A.V., Martin, R.W. Excitation power and temperature dependence of excitons in $CuInSe_2$. *Journal of Applied Physics* **111,** 093507-1–093507-8 (2012).

[35] Tanino H., Maeda T., Fujikake H., Nakanishi H., Endo S., Irie T. Raman spectra of $CuInSe_2$. *Physical Review B* **45**, 13323–13336 (1992).

[36] Schuler S., Siebentritt S., Nishiwaki S., Rega N., Beckmann J., Brehme S., Lux-Steiner M. Ch. Self-compensation of intrinsic defects in the ternary semiconductor $CuGaSe_2$. *Physical Review B* **69**, 045210-1–045210-9 (2004).

[37] Rega, N., Siebentritt, S., Albert, J., Nishiwaki, S., Zajogin, A., Lux-Steiner, M.C., Kniese, R., Romero, M.J. Excitonic luminescence of Cu(In,Ga)Se_2. *Thin Solid Films* **480–481,** 286–290 (2005).

[38] Rincón, C., Márquez, R. Defect physics of the $CuInSe_2$ chalcopyrite semiconductor. *Journal of Physics and Chemistry of Solids* **60**, 1865–1873 (1999).

[39] Chen, S., Walsh, A., Gong, X.G., Wei, S.H. Classification of Lattice Defects in the Kesterite Cu_2ZnSnS_4 and $Cu_2ZnSnSe_4$ Earth-Abundant Solar Cell Absorbers. *Advanced Materials* **25**, 1522–1539 (2013).

[40] Amal, M.I., Kim, K.H. Optical properties of selenized $Cu_2ZnSnSe_4$ films from a Cu-Zn-Sn metallic precursor. *Chalcogenide Letters* **9**, 345–353 (2012).

[41] https://www.unamur.be/services/microscopie/sme-documents/Energy-20table-20for-20EDS-20analysis-1.pdf

[42] Yakushev M.V., Mudryi A.V., Tomlinson R.D. Energy of Free Excitons in $CuInSe_2$ Single Crystals. *Applied Physics Letters* **82** 3233–3235 (2003).

[43] Zhang S.B., Wei S.H., Zunger A., Katayama–Yoshida H. Defect physics of the $CuInSe_2$ chalcopyrite semiconductor. *Physical Review B* **57**, 9642–9656 (1998).